Multi-electron and multi-channel effects on Harmonic Generation

Contact *abrown41@qub.ac.uk*

A.C. Brown and H.W. van der Hart

Centre for Theoretical Atomic, Molecular and Optical Physics,
Queen's University Belfast,
Belfast, BT7 1NN

Introduction

Harmonic generation is one of the phenomena within atomic and molecular physics central to attosecond science [1]. It is the process behind the generation of ultra-short light pulses [2]. The pulses are currently pushing the boundaries of laser science both from an engineering point of view, and in terms of studying fundamental physical entities and processes which unfold on an ultrafast time-scale. Harmonic generation has also been used as a measurement tool: it has been used to image molecular dynamics [3], to obtain detailed information about molecular orbitals [4], and to highlight the importance of multi-electron dynamics in various systems [5,6].

In modeling harmonic generation, many methods make use of the single active electron (SAE) approximation, which is based on a three step, semi classical theory [7]. This theory postulates that a low frequency laser field tunnel ionises and accelerates an electron away from its parent ion. When the electric field changes direction, the electron is accelerated back towards the ionic core, where it can it can be recaptured and emit a photon at an odd harmonic of the driving field. While this theory has helped to harness the power of harmonic generation and explain many of its experimental observations, it neglects the important multi-electron and multi-channel effects which can influence the process, especially at shorter wavelengths.

To investigate the influence of multi-electron dynamics on atomic processes in intense ultra-short light fields, over the last six years we have developed time-dependent R-matrix (TDRM) theory [8]. The theory has been applied to demonstrate how multi-electron dynamics can affect the ionisation dynamics within atoms: in a pump-probe scheme we first excite the $2s2p^2$ configuration of C^+, and then measure how ionisation varies with the probe pulse time delay [9]. With this in mind, we have recently extended TDRM theory to account for harmonic generation. This extension will enable us to assess how harmonic generation is affected by multi-electron and multi-channel dynamics.

In this report, we will first give a short overview of the basic aspects of TDRM theory. We will then explain how harmonic generation is treated within this theory. The method will subsequently be demonstrated for two representative examples: harmonic generation at 390nm for He, which allows us to compare three different schemes for determining the harmonic spectra, and fifth-order harmonic generation in the wavelength range between 200 and 240 nm for Ar, which demonstrates how multi-channel interference can affect the harmonic spectra.

Time-dependent R-matrix theory

The TDRM approach is a non-perturbative, *ab initio* theory for general atomic systems, which allows for the full description of multi-electron dynamics in laser-atom interactions. The approach applies the standard R-matrix technique in which configuration space is partitioned into two regions with a shared boundary. In the inner region, all electrons are within a distance $a \approx 20a_0$ of the nucleus, and all interactions between all electrons are fully described. In the outer region, a single ejected electron has moved beyond a, and has become well separated from the atomic core. In this region, this outer electron moves in the long-range field given by the laser field and a multipole potential of the residual ion.

The time-dependent wavefunction ψ within the inner region is expanded in terms of a standard R-matrix basis [10]. Using a Crank-Nicolson scheme, we can express ψ_{q+1} at time $t=t_{q+1}$ in terms of ψ_q, the solution at the previous time step, thus allowing us to propagate a solution in time. We write ψ at the boundary a in terms of its derivative, ψ', and an R-matrix, **R**, and T-vector, **T**. **T** represents the flow of the known wavefunction, ψ_q, through the boundary a, while **R** describes the flow of the unknown wavefunction ψ_{q+1} through this boundary.

Through the solution of a system of linear equations in the inner region, we can obtain **R** and **T** at a. We then solve a system of coupled differential equations in the outer region to propagate **R** and **T** out to an outer region boundary far away from the residual atom. At this distance, we assume that the unknown wavefunction ψ_{q+1} has vanished, and hence set $\psi_{q+1} = 0$ at this distance. Using **R** and **T**, we can subsequently propagate the wavefunction ψ_{q+1} inwards to obtain it at every point in space. Once we have obtained the full ψ_{q+1}, we can then use this wavefunction as the starting point for the next iteration of the Crank-Nicolson scheme.

Harmonic generation

Harmonic generation arises from the oscillating dipole moment induced during a laser-atom interaction. The harmonic radiation is generated by the acceleration experienced by a charged particle, and hence its spectrum is directly related to the Fourier transform of the expectation value of the dipole acceleration operator during the laser pulse,

$$\ddot{\mathbf{d}} = \frac{d^2}{dt^2}\langle\psi(t)| - e\mathbf{r}|\psi(t)\rangle.$$

Using operator identities, the harmonic spectrum can also be expressed in terms of the Fourier transform of the expectation value of the dipole velocity operator,

$$\dot{\mathbf{d}} = \frac{d}{dt}\langle\psi(t)| - e\mathbf{r}|\psi(t)\rangle,$$

or the Fourier transform of the expectation value of the dipole length operator,

$$\mathbf{d} = \langle\psi(t)| - e\mathbf{r}|\psi(t)\rangle.$$

At present, it is hotly debated in the literature which form provides the best estimate of the harmonic yield [11,12]. Within single-active-electron models, the dipole acceleration form is usually seen as the most reliable, but experience from single-active-electron models was found not to transfer well to the TDRM approach for wavefunction propagation. Within TDRM, the capability exists to use all three expressions for the harmonic spectrum. This capability can be exploited to verify which approach provides the best means for determining reliable harmonic yields.

Application to He

In order to test the reliability of the different expressions for the harmonic spectrum, we have carried out a calculation of the harmonic spectrum for He irradiated by a 14-cycle laser pulse

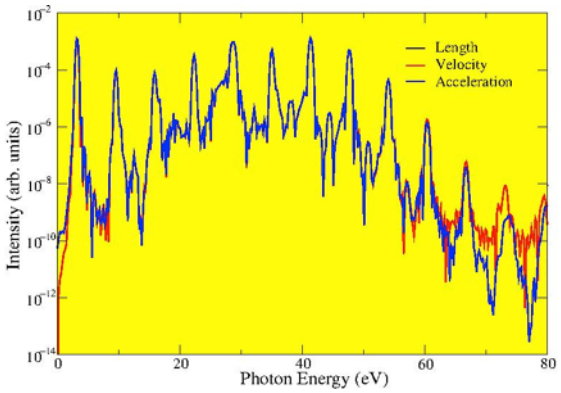

Figure 1 The harmonic spectrum of He in a 14 cycle, 390nm, 4×10^{14} Wcm^{-2} laser field, as calculated from the dipole length (black), velocity (red) and acceleration (blue) operators.

with a wavelength of 390nm, and a peak intensity of 4×10^{14} Wcm^{-2}. The pulse profile contains a 5-cycle turn-on and turn-off and 4 cycles at peak intensity. Figure 1 shows the harmonic spectrum obtained by the different expressions. It can be seen that the differences between the three expressions is rather small: the spectra agree at the harmonic peaks to within 15%, up to an energy of 60 eV. Beyond this energy the spectra diverge.

Application to Ar

As a second example of the application of the extension of the TDRM approach to treat harmonic generation, we investigate the harmonic spectrum generated by an Ar target irradiated by laser light with a wavelength around 200-240 nm with a peak intensity of 2×10^{13} Wcm^{-2}. The reduced intensity compared to the He study means that fewer harmonics will be visible, and we focus our investigation on the fifth harmonic. The yield for this particular harmonic contains contributions from two interfering pathways (Fig. 2): excitation of a 3*s* electron to an excited n*p* state (n≥4), and excitation of a 3*p* electron into the continuum. A multi-electron calculation is essential to describe both of these pathways simultaneously, and hence a multi-electron calculation is essential to obtain accurate harmonic yields.

We find that the interference between these two pathways gives rise to markedly asymmetric resonances in the fifth harmonic response of Ar. This resonance appears as a window resonance in photoionisation yields [13]. For the fifth harmonic, the resonance *q*-parameter is quite different due to the different probabilities of the 3*s* electron and 3*p* electron to absorb five photons rather than a single photon. In addition, the finite pulse duration will broaden the pulse significantly, and, given the intensity of the pulse, photoionisation out of the resonances will also contribute to an increase in the resonance width in the present calculation compared to photoionisation calculations.

The appearance of an asymmetric peak in the harmonic yield is a clear sign that both excitation of a 3s electron and excitation of a 3p electron contribute significantly to the final harmonic

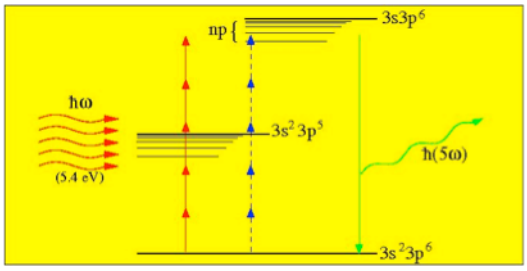

Figure 2 Harmonic generation in Ar is determined by two competing pathways. Absorption of at least 3 photons can excite a 3*p* electron into the continuum (red line), while absorption of 5 photons can excite a 3*s* electron into the n*p* Rydberg series converging onto the $3s3p^6$ threshold (blue line).

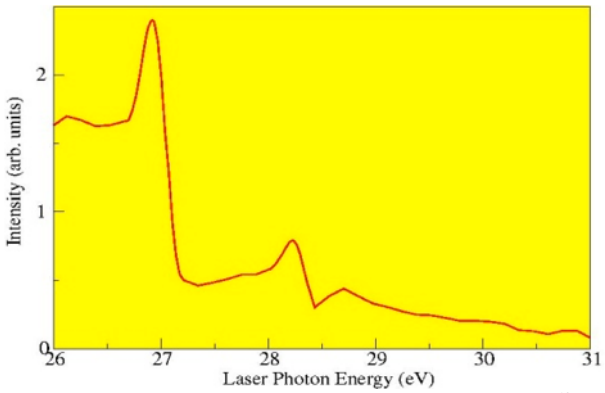

Figure 3 The fifth harmonic yield of Ar in a 25 cycle, 2×10^{13} Wcm^{-2} laser pulse of varying frequency. Asymmetric peaks can be seen at laser photon energies of 26.9 and 28.3 eV.

yield. It is thus a clear demonstration that for an accurate prediction of harmonic yields, it is important to account for the influence of multi-electron dynamics. In this respect the TDRM approach will provide a major benefit over SAE models.

Conclusions

We have developed capability within time-dependent R-matrix theory to describe harmonic generation, including the influence of multi-electron dynamics and multi-channel dynamics on the harmonic yields. Harmonic yields can be obtained from the time-dependent expectation value of the dipole acceleration, dipole velocity or dipole length operator. The three different forms for the harmonic yields are in good agreement with each other for a test case of He irradiated by 390 nm laser light. The importance of multi-channel effects is demonstrated by the investigation of fifth harmonic yields in Ar.

The present results are strongly encouraging for further investigation and development. In particular, it will be of interest to adopt the R-matrix with time-dependence (RMT) codes to describe harmonic generation. The increased parallelism offered by this code may make calculations at the experimentally interesting wavelength of 800 nm feasible.

Acknowledgements

AB acknowledges financial support from DELNI through the programme for government. HvdH is supported by the ESPRC through grant number EP/G055416/1.

References

1. P B Corkum and F. Krausz, *Nat phys* **3** 381 (2007)
2. P M Paul *et al*, *Science* **292** 5522 (2001)
3. S Baker *et al*, *Science* **312** 5772 (2006)
4. P B Corkum, *Phys. Today* **64** 36 (2011)
5. O Smirnova *et al*, *Nature* **460** 972 (2009)
6. A D Shiner *et al*, *Nat. Phys.* **7** 464 (2011)
7. M Lewenstein *et al*, *Phys. Rev. A.* **49** 2117 (1994)
8. M A Lysaght *et al*, *Phys. Rev. A.* **79** 053411 (2009)
9. M A Lysaght *et al*, *Phys. Rev. Lett.***102** 193001 (2009)
10. P.G. Burke and K.A. Berrington, *Atomic and Molecular Processes: an R-matrix approach* (Bristol: Institute of Physics Publishing, 2003)
11. J C Baggesen and L B Madsen, *J. Phys. B: At. Mol. Opt. Phys.***44** 115601 (2012)
12. J A Pérez-Hernández and L Plaja *J. Phys. B: At. Mol. Opt. Phys.* **45** 028001 (2012)
13. P G Burke and K T Taylor, *J. Phys. B: At. Mol. Opt. Phys.* **8** (1975)

A new equation of state for waterbag-distributed plasma

Contact *d.burton@lancaster.ac.uk*

DA Burton
Physics Department, Lancaster University
& The Cockcroft Institute, Daresbury, UK

H Wen
Physics Department, Lancaster University
& The Cockcroft Institute, Daresbury, UK

Analytical investigation of the properties of large-amplitude plasma waves is a task that has fascinated numerous workers over many years [1–13]. Of particular interest is the maximum amplitude that a non-linear electrostatic wave can attain; for sufficiently large fields, non-linearities lead to collapse of the wave structure ("wave-breaking") due to sufficiently large numbers of electrons becoming trapped in the wave. However, quantifying "sufficiently large" is far from straightforward and, instead, effort tends to focus on the domain of quasi-static solutions of a system of equations describing the plasma. The results of such approaches are highly model-dependent and the relationship between the maximum amplitudes given by those approaches and the actual physical amplitude at wave-breaking is a source of considerable debate [6–8].

Due to their relative simplicity, piecewise constant distributions with compact support in velocity space (so-called "waterbag" distributions) have been used extensively in the study of large amplitude electrostatic waves in warm plasmas [2,3,6,10,11]. Waterbag distributions are highly amenable to analytical investigation and naturally offer *exact* dynamical solutions to the Vlasov-Maxwell system. Although it is certainly the case that the inherent simplicity of waterbag distributions restricts their domain of applicability, one cannot dispute that they are a useful *non-perturbative* tool for probing the solution space of the Vlasov-Maxwell system. From the outset, any issues that arise concerning the applicability of waterbag distributions can only be attributed to their structure and not to deviation from the solution space of the Vlasov-Maxwell system. It follows that they are a natural tool for analysing large-amplitude waves in collisionless plasmas.

The Vlasov-Maxwell system was used recently [10] to induce a non-linear 2nd-order ODE for the boundary of a 3D "gourd"-type waterbag distribution whose periodic quasi-static solutions were shown to have the maximum electric field

$$E_{\max}^2 \approx \frac{m^2\omega_p^2 c^2}{q^2}\left(\frac{9mc^2}{20k_B T_{\|\mathrm{eq}}}\right)^{1/2} \qquad (1)$$

in the limit of ultrarelativistic phase velocities, with $\omega_p = \sqrt{n_{\mathrm{ion}} q^2/(m\varepsilon_0)}$ the plasma frequency, m the rest mass of the electron, q the charge of the electron and n_{ion} the proper number density of the ions (modelled as a homogenous background). The above result holds for a sufficiently narrow waterbag distribution whose normalized longitudinal thermal spread $k_B T_{\|\mathrm{eq}}/mc^2$ at equilibrium is sufficiently small.

Equation (1) was obtained from a direct attack on the Vlasov-Maxwell system using geometrical methods [10]. Although highly amenable to analysis, this approach bypasses the fluid dynamics of the plasma and further work is required to reveal the plasma's thermodynamic properties. In the present article we present an equation of state derived from the 3D "gourd" waterbag studied recently [10] and, as a consistency check, show that the equation of state is compatible with a finite maximum electric field for a wave with an ultrarelativistic phase velocity. The plasma's heat flux plays a critical role in the derivation of this result.

In the following, Greek indices range over $0, 1, 2, 3$, the Einstein summation convention is used throughout, indices are raised and lowered using the Minkowski metric $[\eta_{ab}] = \mathrm{diag}(-1, 1, 1, 1)$ and Heaviside-Lorentz units are used in which $c = 1$. The plasma electrons are represented by a 1-particle distribution f and the ions are treated as an immobile homogenous background because their motion is negligible over timescales of present interest. We use Lorentz coordinates (x^μ) adapted to the inertial frame associated with the ion background and the location of a point in proper velocity space is denoted by the 3-dimensional vector $\dot{\boldsymbol{x}} = (\dot{x}^1, \dot{x}^2, \dot{x}^3)$, which should be understood to be independent of spatial position $\boldsymbol{x} = (x^1, x^2, x^3)$. For clarity, in the following we use x^0 and t interchangeably.

The value $f(t, \boldsymbol{x}, \dot{\boldsymbol{x}})$ of the 1-particle waterbag distribution f is a positive constant if $\dot{\boldsymbol{x}} \in \mathcal{W}_x$ and zero if $\dot{\boldsymbol{x}} \notin \mathcal{W}_x$, with the subscript x indicating that the subset $\mathcal{W}_x$ of proper velocity space depends on the point $(x^\mu) \equiv (t, \boldsymbol{x})$ in spacetime. The fluid ("bulk") properties of the plasma electrons are encoded in tensors on spacetime obtained as moments in $\dot{x}^\mu$ of $f(t, \boldsymbol{x}, \dot{\boldsymbol{x}})$:

$$\begin{aligned} S^{\mu\cdots\nu}(t, \dot{\boldsymbol{x}}) &= \int \dot{x}^\mu \ldots \dot{x}^\nu f(t, \boldsymbol{x}, \dot{\boldsymbol{x}}) \frac{d\dot{x}^1 \wedge d\dot{x}^2 \wedge d\dot{x}^3}{\sqrt{1 + |\dot{\boldsymbol{x}}|^2}} \\ &= \alpha \int_{\mathcal{W}_x} \dot{x}^\mu \ldots \dot{x}^\nu \frac{d\dot{x}^1 \wedge d\dot{x}^2 \wedge d\dot{x}^3}{\sqrt{1 + |\dot{\boldsymbol{x}}|^2}} \end{aligned}$$

with $\dot{x}^0 \equiv \sqrt{1 + |\dot{\boldsymbol{x}}|^2}$, where $f(t, \boldsymbol{x}, \dot{\boldsymbol{x}}) = \alpha > 0$ if $\dot{\boldsymbol{x}} \in \mathcal{W}_x$ and $f(t, \boldsymbol{x}, \dot{\boldsymbol{x}}) = 0$ if $\dot{\boldsymbol{x}} \notin \mathcal{W}_x$. The moments of interest in the present article are the electron number 4-current density N^μ and the electron fluid's stress-

energy-momentum tensor $T^{\mu\nu}$,

$$N^\mu(t,\dot{\boldsymbol{x}}) = \alpha \int_{\mathcal{W}_x} \dot{x}^\mu \frac{d\dot{x}^1 \wedge d\dot{x}^2 \wedge d\dot{x}^3}{\sqrt{1+|\dot{\boldsymbol{x}}|^2}}, \tag{2}$$

$$T^{\mu\nu}(t,\dot{\boldsymbol{x}}) = m\alpha \int_{\mathcal{W}_x} \dot{x}^\mu \dot{x}^\nu \frac{d\dot{x}^1 \wedge d\dot{x}^2 \wedge d\dot{x}^3}{\sqrt{1+|\dot{\boldsymbol{x}}|^2}} \tag{3}$$

The particular $\mathcal{W}_x$ of interest here is axisymmetric around the $\dot{x}^3$-axis and its boundary $\partial\mathcal{W}_x$ is parameterized as

$$\dot{x}^0 = \mu(\zeta) + A(\xi^1) + v\psi(\xi^1,\zeta), \tag{4}$$

$$\dot{x}^1 = R\sin(\xi^1)\cos(\xi^2), \tag{5}$$

$$\dot{x}^2 = R\sin(\xi^1)\sin(\xi^2), \tag{6}$$

$$\dot{x}^3 = v[\mu(\zeta) + A(\xi^1)] + \psi(\xi^1,\zeta) \tag{7}$$

where R is constant controlling the distribution's extent in the $\dot{x}^1, \dot{x}^2$ plane and

$$\psi = -\sqrt{[\mu + A(\xi^1)]^2 - \gamma^2[1 + R^2\sin^2(\xi^1)]}, \tag{8}$$

with $0 < \xi^1 < \pi$ and $0 \le \xi^2 < 2\pi$ curvilinear coordinates on proper velocity space, $\zeta \equiv x^3 - vx^0$ the phase of the wave, v the phase velocity of the wave and $\gamma \equiv 1/\sqrt{1-v^2}$. The generator $A(\xi^1)$ of $\mathcal{W}_x$ is chosen to have the form $A(\xi^1) = -a\cos(\xi^1)$, with the constant $a > 0$, and the condition

$$\frac{a}{R}\sqrt{\frac{1+R^2}{a^2+\gamma^2R^2}} > 1$$

ensures that the waterbag is of the "gourd" type discussed in [10]. We comment that the ansätz $(4-7)$ was carefully chosen to reduce the Vlasov-Maxwell system to a second order ODE for $\mu(\zeta)$ which may be tackled directly, without recourse to the stress-energy-momentum tensor [10]. However, here we focus on properties of $T^{\mu\nu}$ in order to gain a new perspective on the electron fluid's behaviour.

Evaluation of (2, 3) proceeds by using Stokes' theorem on differential forms:

$$\int_{\mathcal{M}} d\alpha = \int_{\partial\mathcal{M}} \alpha, \tag{9}$$

where α is a p-form and $\mathcal{M}$ is a $p+1$-dimensional orientable manifold. Using (9) it is straightforward to rewrite the various components of (2, 3) as integrals over $\partial\mathcal{W}_x$:

$$N^0 = \alpha\int_{\partial\mathcal{W}_x} \dot{x}^3\Omega, \qquad N^3 = \alpha\int_{\partial\mathcal{W}_x} \dot{x}^0\Omega,$$

$$T^{00} = \frac{m\alpha}{2}\int_{\partial\mathcal{W}_x} [\dot{x}^3\dot{x}^0 + (\dot{x}^{02} - \dot{x}^{32})\ln(\dot{x}^3 + \dot{x}^0)]\Omega,$$

$$T^{33} = \frac{m\alpha}{2}\int_{\partial\mathcal{W}_x} [\dot{x}^3\dot{x}^0 - (\dot{x}^{02} - \dot{x}^{32})\ln(\dot{x}^3 + \dot{x}^0)]\Omega,$$

$$T^{03} = \frac{m\alpha}{2}\int_{\partial\mathcal{W}_x} \dot{x}^{32}\Omega$$

where $\Omega = d\dot{x}^1 \wedge d\dot{x}^2$. The remaining components of N^μ and $T^{\mu\nu}$ either vanish by virtue of the axisymmetry of $\mathcal{W}_x$ or they are constant and do not contribute to the dynamics. The above are then immediately recast as integrals over $0 < \xi^1 < \pi$, $0 \le \xi^2 < 2\pi$ using

$$d\dot{x}^1 \wedge d\dot{x}^2 = R^2\sin(\xi^1)\cos(\xi^1)\, d\xi^1 \wedge d\xi^2.$$

The focus of this article is on quasi-static longitudinal electric waves. Hence $F_{\mu\nu} = E(\zeta)(\delta^0_\mu\delta^3_\nu - \delta^3_\mu\delta^0_\nu)$ and the bulk 4-velocity $V^\mu \equiv N^\mu/\sqrt{-N^\nu N_\nu}$ of the electrons is of the form $V^\mu = \Gamma(\delta^\mu_0 + u\delta^\mu_3)$, where $\Gamma \equiv 1/\sqrt{1-u^2}$ and $u = u(\zeta)$. The timelike unit 4-vector V^μ and the spacelike unit 4-vectors $Z^\mu \equiv \Gamma(\delta^\mu_3 + u\delta^\mu_0)$, δ^μ_1, δ^μ_2 form an orthonormal basis for 4-vectors on spacetime suitable for exploring longitudinal waves.

The stress-energy-momentum tensor $T^{\mu\nu}$ of the electron fluid may be decomposed as

$$T^{\mu\nu} = eV^\mu V^\nu + \xi(V^\mu Z^\nu + Z^\mu V^\nu) + pZ^\mu Z^\nu + T^{\mu\nu}_\perp$$

where e is the total proper mass-energy density, ξ is the relativistic heat flux, p is the relativistic pressure, and the transverse component $T^{\mu\nu}_\perp$ of $T^{\mu\nu}$ satisfies $T^{\mu\nu}_\perp V_\mu = T^{\mu\nu}_\perp Z_\mu = 0$. The balance law

$$\partial_\mu T^\mu{}_\nu = q\, N^\mu F_{\mu\nu} \tag{10}$$

couples the electron fluid's stress-energy-momentum tensor and number 4-current density to the electromagnetic field $F_{\mu\nu}$. Combining (10) with Maxwell's equations

$$\partial_\mu F_{\nu\omega} + \partial_\omega F_{\mu\nu} + \partial_\omega F_{\mu\nu} = 0, \quad \partial_\mu F^{\mu\nu} = q(N^\nu - N^\nu_{\rm ion})$$

leads to

$$\frac{dE}{d\zeta} = \frac{1}{2}qn_{\rm ion}\left[\left(\frac{n}{n_{\rm ion}}\right)^2 - 1\right], \tag{11}$$

$$\frac{d}{d\zeta}\left[(e+p-2\xi)\left(\frac{n_{\rm ion}}{n}\right)^2\right] = qn_{\rm ion}E \tag{12}$$

in the limit that the phase velocity $v \to 1$, where $N^\mu_{\rm ion} = n_{\rm ion}\delta^\mu_0$ is the ion number 4-current with $n_{\rm ion}$ the proper number density of the ions and $n \equiv \sqrt{-N^\mu N_\mu}$ is the proper number density of the electron fluid. The macroscopic quantities e, p, ξ only enter into (11, 12) in the combination $e + p - 2\xi$ after the limit $v \to 1$ has been taken.

The maximum amplitude electric field $E_{\max}$ is given by

$$E^2_{\max} = \left[-(e+p-2\xi) + n^2_{\rm ion}\frac{e+p-2\xi}{n^2}\right]_{n=n_{\rm ion}}^{n=n_{\max}} + \int_{n_{\rm ion}}^{n_{\max}} \frac{2(e+p-2\xi)}{n}\, dn \tag{13}$$

which is obtained by integrating (11, 12) between $(n = n_{\rm ion}, E = -E_{\max})$ and $(n = n_{\max}, E = 0)$. Although an explicit simple expression for the maximum

value $n_{\max}$ of n is not known, it is fruitful to explore the behaviour of (13) for large $n_{\rm ion}$ in the limit $n_{\max} \to \infty$ since $n \gg n_{\rm ion}$ is expected for a wave with ultrarelativistic phase velocity. By far the most difficult part of the exercise is to obtain $e + p - 2\xi$ as a function of n, which follows by eliminating the waterbag variable μ from expressions for $e + p - 2\xi$ and n obtained using $T^{\mu\nu}$ and N^{μ}. A lengthy calculation yields the central result of this article:

$$e + p - 2\xi \approx \frac{mc^2 n^2 b}{n_{\rm ion}} \left[1 + 8 \exp\left(- \frac{2n^2 b^2}{3n_{\rm ion}^2} - \frac{5}{2} \right) \right] + \frac{13 mc^2 n_{\rm ion}}{b} \exp\left(- \frac{2n^2 b^2}{3n_{\rm ion}^2} - \frac{5}{2} \right) \tag{14}$$

for $R \ll 1$ (the waterbag is narrow), where the speed of light c has been restored on the right-hand side of (14), the dimensionless constant $b \approx \sqrt{5 k_B T_{\|\rm eq}/mc^2}$, and the ratio $n/n_{\rm ion}$ is sufficiently large. The details of $e + p - 2\xi$ for $n \approx n_{\rm ion}$ are not required in this article because we are presently only interested in whether or not (13) converges in the limit $n_{\max} \to \infty$ with fixed $n_{\rm ion}$ and b.

As expected, insertion of (14) into (13) leads to a finite value for $E_{\max}^2$ in the limit $n_{\max} \to \infty$ with fixed $n_{\rm ion}$ and b. It turns out that the role of ξ is critical to ensure that (13) yields a finite maximum electric field; in the case of the 1D waterbag due to Katsouleas and Mori [3], the heat flux vanishes and $E_{\max}^2$ diverges logarithmically in $n_{\max}$.

Acknowledgements

We thank the Cockcroft Institute and the ALPHA-X project for support, and RMGM Trines for useful discussions.

References

[1] JM Dawson, Phys. Rev. 113 (1959) 383

[2] TP Coffey, Phys. Fluids 14 (1971) 1402

[3] T Katsouleas and WB Mori, Phys. Rev. Lett. 61 (1988) 90

[4] JB Rosenzweig, Phys. Rev. A 38 (1988) 3634

[5] CB Schroeder, E Esarey and BA Shadwick, Phys. Rev. E 72 (2005) 055401

[6] RMGM Trines and PA Norreys, Phys. Plasmas 13 (2006) 123102

[7] CB Schroeder, E Esarey and BA Shadwick, Phys. Plasmas 14 (2007) 084701

[8] RMGM Trines and PA Norreys, Phys. Plasmas 14 (2007) 084702

[9] RMGM Trines, Phys. Rev. E 79 (2009) 056406

[10] DA Burton and A Noble, J. Phys. A: Math. Theor. 43 (2010) 075502

[11] T Coffey, Phys. Plasmas 17 (2010) 052303

[12] DA Burton, RMGM Trines, TJ Walton and H Wen, J. Phys. A: Math. Theor. 44 (2011) 095501

[13] PS Verma, S Sengupta and P Kaw, Phys. Rev. Lett. 108 (2012) 125005

Development and Validation of a 1D2V Vlasov-Fokker-Planck Model

T. E. Fox,[1, 2, *] A. P. L. Robinson,[2] and J. Pasley[1, 2]

[1] *York Plasma Institute, University of York, York, YO10 5DD, United Kingdom*
[2] *Central Laser Facility, STFC Rutherford Appleton Laboratory, Harwell Oxford, Didcot, OX11 0QX, United Kingdom*

Inertial fusion energy (IFE) has the potential to provide a clean, safe, abundant, secure and complementary method of generating useful electrical energy. However, developing an efficient IFE scheme is reliant on effectively coupling a radiation source e.g. a laser to an IFE fuel capsule. Coupling occurs via electrons and thus a detailed understanding of their transport behaviour under the extreme conditions generated by inertial confinement fusion is required. A 1d2v Vlasov-Fokker-Planck model capable of simulating this behaviour has been developed and is nearing the end of an extensive validation phase that has yielded promising results. The construction of the model and the results of the suite of validation tests form the focus of this paper.

I. INTRODUCTION

The aim of inertial confinement fusion (ICF) [1] is to provide a viable route to electrical power generation via thermonuclear fusion. ICF involves compressing a spherical deuterium-tritium (DT) fuel capsule to reach the conditions necessary for ignition e.g. temperatures of $T_i > 10$keV and areal densities $\rho R > 0.3\text{gcm}^{-2}$. A number of different schemes are considered and these are broadly grouped under direct drive (DD) and indirect drive (ID) schemes. ID schemes place the capsule inside a high Z hohlraum. Lasers enter through holes in either end of the holhraum, impinge on its inner surface and are remitted as x-rays. The x-rays uniformly irradiate the capsule causing it to ablate and drive the fuel inwards. DD schemes use the lasers to directly and uniformly irradiate the capsule sans-hohlraum, causing it to ablate and drive the compression. Whichever sub-scheme is chosen e.g. DD fast ignition [2, 3] or shock ignition [4], the goal is to create a hotspot in the compressed fuel that will ignite and drive an outwardly propagating burn wave as the remaining dense fuel ignites. However, an electromagnetic-wave cannot propagate in the high density plasma undergoing compression and instead couples to the lower density plasma of the ablated corona. The energy deposited there is transported to the ablation front by electrons. An efficient ICF scheme is reliant on an understanding of the efficacy of this electron transport.

Under ICF conditions the laser intensities are sufficient to produce steep temperature gradients with lengthscales shorter than the mean-free path. The resulting non-local thermal transport is poorly modelled by the classical transport description and a kinetic approach is more appropriate. A fully kinetic 1d2v Vlasov-Fokker-Planck model (hereafter referred to as 'the Model') has been developed with a view to study electron transport problems of particular relevance to shock ignition. The validation phase of the development process is currently coming to an end and has yielded promising results that are the focus of this paper.

This paper will proceed with a description of the Model and the construction of the computational domain in Sections II and III respectively. Presented in Section IV are the results from an extensive but not exhaustive suite of validation tests while Section V describes the tests that will complete the validation phase and provide confidence in the Model. Section VI contains some concluding remarks.

II. VLASOV-FOKKER-PLANCK MODEL

The Vlasov-Fokker-Planck equation for a plasma consisting of an electron population and a single ion species is given in its general form by eqn. (1). The Model is completed by coupling this to Maxwell's equations via appropriate moments of the distribution function.

$$\frac{\partial f_\alpha}{\partial t} + \mathbf{v}\cdot\frac{\partial f_\alpha}{\partial \mathbf{r}} + \frac{q_\alpha}{m_\alpha}(\mathbf{E}+\mathbf{v}\times\mathbf{B})\cdot\frac{\partial f_\alpha}{\partial \mathbf{v}} = C_{ee}(f_\alpha)+C_{ei}(f_\alpha) \tag{1}$$

In eqn. (1) α denotes the species, f is the distribution function, q_α is the charge of species α and C_{ee} and C_{ei} represent the Fokker-Planck operators for electron-electron and electron-ion collisions respectively. At present, the Model supports a single electron population and a single, stationary ion population. Thus the subscript α will be dropped, f will be assumed to be the electron distribution function, m_e will replace m_α and $-e$ will replace q_α.

Following the approach originally implemented in [5], the distribution function is represented in velocity space (v, θ, ϕ) by a series expansion in spherical harmonics:

$$f(\mathbf{r},\mathbf{v},t) = \sum_{l=0}^{l_{max}}\sum_{m=-l}^{l} f_l^m(\mathbf{r},v,t)P_l^{|m|}(cos\theta)\mathrm{e}^{\mathrm{i}m\phi}$$
$$\text{where } f_l^{-m} = (f_l^m)^*. \tag{2}$$

* tef503@york.ac.uk

The Model supports an arbitrary number of harmonics, one spatial dimension and phase space can be considered axisymmetric and characterised by $|\mathbf{v}|$, θ. Following the spherical harmonic expansion the set of equations that the Model solves in this 1d2v space can be written in the form

$$\frac{\partial f_l^m}{\partial t} - \mathcal{C}_{l,ei}^m - \mathcal{C}_{l,ee}^m - \mathcal{B}_{l,z}^m = \mathcal{A}_{l,x}^m + \mathcal{E}_{l,x}^m + \mathcal{E}_{l,y}^m. \quad (3)$$

The terms on the left represent collision and magnetic field operators and are treated implicitly while the terms on the right represent advection and electric field operators and are treated explicitly.

The magnetic field operator rotates the distribution function for $m > 0$ according to

$$\mathcal{B}_l^m = -\frac{1}{2}\frac{eB_z}{m_e}\left[(l-m)(l+m+1)f_l^{m+1} - f_l^{m-1}\right] \quad (4)$$

while for $m = 0$ the operator is

$$\mathcal{B}_l^0 = -\frac{eB_z}{m_e} l(l+1) f_l^1. \quad (5)$$

Each term only couples harmonics f_l^{m-1}, f_l^m and f_l^{m+1} and this set of equations forms an algebraic tri-diagonal matrix equation which can be solved by standard methods using a Crank-Nicholson type scheme to integrate implicitly in time. The magnetic field itself is updated from Maxwell's equation $\partial B_z/\partial t = -\partial E_y/\partial x$.

The spatial advection operator in the x-direction takes the form

$$\mathcal{A}_{l,x}^m = -\left(\frac{l-m}{2l-1}\right) v\frac{\partial f_{l-1}^m}{\partial x} - \left(\frac{l+m+1}{2l+3}\right) v\frac{\partial f_{l+1}^m}{\partial x}. \quad (6)$$

This set of equations can be easily cast in matrix form as $\frac{\partial \mathbf{Q}}{\partial t} + \mathbf{A}\frac{\partial \mathbf{Q}}{\partial x} = 0$ where $\mathbf{Q} = \{f_l\}$ and $\mathbf{A}$ is the $(l_{max}+1)\times(l_{max}+1)$ matrix of constant coefficients defined by eqn. (6). Assuming $\mathbf{A}$ has only real and distinct eigenvalues it can be shown that

$$\frac{\partial \mathbf{W}}{\partial t} + \mathbf{\Lambda}\frac{\partial \mathbf{W}}{\partial x} = 0 \quad (7)$$

where $\mathbf{\Lambda}$ is the matrix of eigenvalues of $\mathbf{A}$ and $\mathbf{W} = \mathbf{K}^{-1}\mathbf{Q}$, where $\mathbf{K}$ is the matrix of eigenvectors of $\mathbf{A}$. Eqn. 6 has now been reduced to a set of uncoupled constant coefficient advection equations which can be solved using standard, well developed methods. The Model currently employs a Van Leer-Limited Flux Balance Method as described in [6], with a view to improve this to the more advanced Piecewise Parabolic Method in the future.

The Model includes electric fields in the x- and y-directions. Implementing the electric field operator is complex as it couples harmonics across different l and m indices. In the x-direction the operator is given by eqn. (8) for all $m \geq 0$. In the y-direction the operator is given by eqn. (9) for $m > 0$ and eqn. (10) for $m = 0$.

$$\mathcal{E}_{l,x}^m = \frac{eE_x}{m_e}\left[\frac{l-m}{2l-1}G_{l-1}^m + \frac{l+m+1}{2l+3}H_{l+1}^m\right] \quad (8)$$

$$\mathcal{E}_{l,y}^m = \frac{1}{2}\frac{eE_y}{m_e}\left[\frac{1}{2l-1}\left[G_{l-1}^{m-1} - (l-m)(l-m-1)G_{l-1}^{m+1}\right] - \frac{1}{2l+3}\left[H_{l+1}^{m-1} - (l+m+1)(l+m+2)H_{l+1}^{m+1}\right]\right] \quad (9)$$

$$\mathcal{E}_{l,y}^0 = \frac{eE_y}{m_e}\left[-\frac{l(l-1)}{2l-1}G_{l-1}^1 + \frac{(l+1)(l+2)}{2l+3}H_{l+1}^1\right] \quad (10)$$

In the above two differential functions were defined as

$$G_l^m(v) = v^l\frac{\partial(v^{-l}f_l^m)}{\partial v}; \qquad H_l^m(v) = \frac{1}{v^{l+1}}\frac{\partial(v^{l+1}f_l^m)}{\partial v}. \quad (11)$$

The electric field operators are center differenced in velocity and time with a second order Runge Kutta solution being used for time integration.

Angular scattering by stationary ions is the dominant collisional process and is described by eqn. (12). This represents an exponential decay of each harmonic f_l^m at a rate proportional to $l(l+1)$. Thus higher harmonics decay at a faster rate providing a natural truncation to the spherical harmonic expansion. Eqn. (12) is solved implicitly.

$$\mathcal{C}_{l,ei}^m = -\frac{l(l+1)}{2}\frac{Z^2 n_i e^4 \ln\Lambda_{ei}}{4\pi\epsilon_0^2 m_e^2}\frac{1}{v^3}f_l^m \quad (12)$$

Collisions between electrons are a more involved affair and typically involve scattering each harmonic off every other harmonic which rapidly becomes a considerable effort. Since collisions are more significant for colder electrons and that the electron-ion term is larger than the electron-electron term by a factor Z^2 a semi-isotropic approximation is appropriate. In this approximation the contribution from the isotropic part of the distribution function is taken to represent the total effect of electron-electron collisions. This approach does not conserve momentum but in this model neither do electron-ion collisions. Eqns. (13)–(16), in which $\Gamma_{ee} = \frac{e^4\ln\Lambda_{ee}}{4\pi\epsilon_0^2 m_e^2}$, together describe the semi-isotropic approximation for electron-electron collisions.

$$\mathcal{C}_{l,ee}^m = \frac{\Gamma_{ee}}{v^2}\frac{\partial}{\partial v}\left[D_{\parallel -0}(v)\frac{\partial f_l^m}{\partial v} + C_0(v)f_l^m\right] - \frac{l(l+1)}{2v^2}\Gamma_{ee}D_{\perp -0}(v)f_l^m \quad (13)$$

$$C_0(v) = 4\pi \int_0^v f_0(u) u^2 \mathrm{d}u \tag{14}$$

$$D_{\parallel -0}(v) = \frac{4\pi}{v} \int_0^v u^2 \left\{ \int_0^\infty f_0(v') v' \mathrm{d}v' \right\} \mathrm{d}u \tag{15}$$

$$D_{\perp -0}(v) = \frac{4\pi}{3} \left[\frac{3}{v} \int_0^v u^2 f_0(u) \mathrm{d}u - \frac{1}{v^3} \int_0^v u^4 f_0(u) \mathrm{d}u + 2 \int_v^\infty u f_0(u) \mathrm{d}u \right] \tag{16}$$

The first term in eqn. (13) is a 'drag' term describing energy transfer between electrons and is included in the Model implicitly using Chang-Cooper differencing [7] but using the approach introduced in [8] for solving eqn. (15) to improve energy conservation. The second term in eqn. (13) describes angular scattering and is solved implicitly.

III. COMPUTATIONAL DOMAIN

The computational domain is divided up into $nx \times nv$ cells with nx spatial cells and nv velocity cells, each of a fixed width Δx and Δv respectively. The x-coordinate of the cell centers are denoted x_i for $i = 1, \ldots, nx$ and lie half-way between the adjacent cell boundaries defined at $x_{i+1/2}$. The boundaries of the domain lie at $x_{1/2}$ and $x_{nx+1/2}$. This indexing scheme is cell centered and requires ghost cells external to the domain to be included at x_0 and x_{nx+1} to implement boundary conditions. The velocity grid is similarly defined. Reflective spatial boundary conditions are the default although periodic boundaries are available. The upper velocity boundary is open and assumes $f \to 0$ as $v \to \infty$. The lower velocity boundary condition requires that the isotropic part of the distribution has an extremum at $v = 0$ and that $f^m_{l\geq 1}(v \to 0) \sim v^l$. Assuming that $f^0_0(v_1)$ and $f^0_0(v_2)$ lie on the parabola $f^0_0(0) + \alpha_{00} v^2$ gives

$$f^0_0(v) = f^0_0(0) + [f^0_0(v_2) - f^0_0(0)] \left(\frac{v}{v_2} \right)^2,$$
$$f^0_0(0) = \frac{f^0_0(v_1) - f^0_0(v_2) v_1^2 / v_2^2}{1 - v_1^2 / v_2^2} \tag{17}$$

$$f^m_{l\geq 1}(v) = f^m_l(v_2) \left(\frac{v}{v_2} \right)^l. \tag{18}$$

IV. CODE VALIDATION

An extensive period of validation work has been conducted to test components of the Model working individually and in unison. The following subsections detail the results of the most significant tests undertaken thus far.

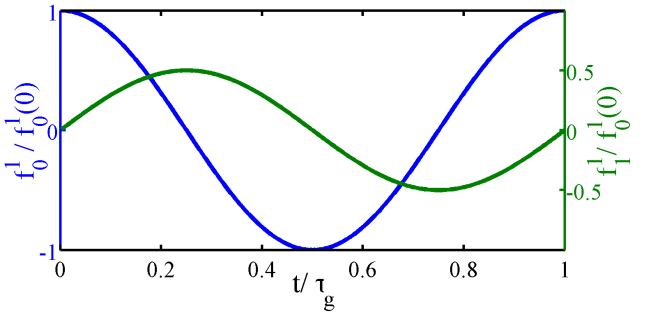

FIG. 1. A single period of the evolution of f^0_1 and f^1_1 as the electron distribution function is rotated by an external magnetic field, $B = 2\pi m_e/e$. The full simulation period was $10\tau_g$ but a single gyro-period is shown for clarity. A time step $\Delta t = \tau_g/400$ gave an error of ~0.001% in the Fourier components with respect to eqn. (19) and a total phase shift error on the order of $\Delta t/100$.

A. Magnetic Field

Free electrons under the influence of an external magnetic field will perform gyro-rotations at the gyro-frequency $\omega_g = eB/m_e$. In the Model this behaviour manifests as a rotation of the distribution function through different harmonics. In the case when $l_{max} = 1$ eqns. (4) and (5) are satisfied by the simple harmonic oscillator solutions,

$$f^0_1(t) = f^0_1(0) \cos(\omega_g t) \qquad f^1_1 = \frac{f^0_1(0)}{2} \sin(\omega_g t). \tag{19}$$

The absence of derivatives in $\mathcal{B}$ mean that a single cell of the f^0_1 and f^1_1 computational domains can be initialised and their evolution compared to eqn. (19). Figure 1 shows the evolution of these cells as a magnetic field $B = 2\pi m_e/e$ rotates the distribution through the f^0_1 and f^1_1 harmonics for one gyro-period, $\tau_g = 2\pi/\omega_g$.

The full test period was $10\tau_g$ using $\Delta t = \tau_g/400$. Over this period the results match their respective theoretical Fourier components with an error of ~0.001%. The relative phase shift between the results and theory after 4000 time steps is on the order of $\Delta t/100$.

B. Application of a Constant Electric Field

A collisionless, quasi-neutral, uniform plasma with an electron number density $n_e = 10^{27}\mathrm{m}^{-3}$ and electron temperature, $T_e = 50\mathrm{eV}$ was subjected to a constant electric field, $E = 10^3 \mathrm{Vm}^{-1}$ for a period $\tau = 10\tau_{pc}$ where $\tau_{pc} = 2\pi/\omega_{pc} = 2\pi/\sqrt{n_e e^2/\epsilon_0 m_e}$ is the cold plasma period and ω_{pc} is the cold plasma frequency. This produces a predictable current density given by

$$J = \frac{n_e e^2 E}{m_e} \tau \tag{20}$$

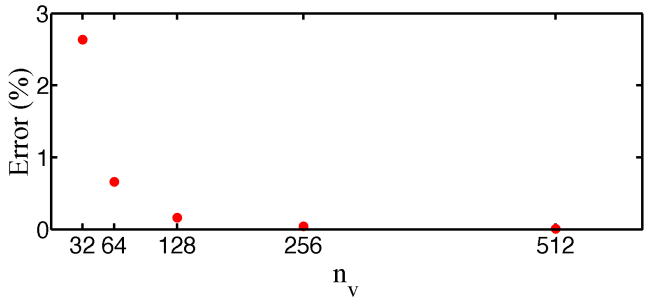

FIG. 2. Percentage errors in the final current density achieved after applying a constant electric field for $10\tau_{pc}$. Errors are improved by increasing the velocity grid resolution with sub-percent errors easily achievable.

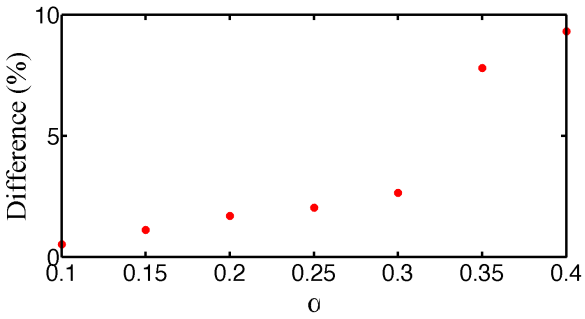

FIG. 3. The warm plasma frequencies produced by the Model show good agreement with eqn. (21) in the regime where it is expected to be valid. As expected, when $v_\phi \gg v_{th}$ is no longer satisfied the difference between the two becomes more apparent.

The distribution function was represented up to $v_{max} = 9v_{th}$ using $l_{max} = 10$. The time-step was automatically chosen to satisfy the most stringent Courant-Friedrichs-Lewy (CFL) stability condition at each step. Figure 2 shows the effect that increasing the resolution in $|\mathbf{v}|$ has on the error as it drops from 2.6% for $n_v = 32$ to 0.01% for $n_v = 512$. Thus, sub-percent errors are easily achievable.

C. Warm Plasma Oscillations

It can be shown from kinetic theory that a warm plasma subjected to a plasma wave of phase velocity $v_\phi = \omega_{ph}/k$ in the regime where $v_\phi \gg v_{th}$ will oscillate (for sufficiently small k) with frequency

$$\omega_{ph} = \sqrt{\omega_{pc}^2 + 3k^2 v_{th}^2} \tag{21}$$

Writing the dispersion relation in this form shows the correction that a finite electron temperature makes to the cold plasma frequency.

To reproduce warm plasma oscillations as a precursor to simulating Landau Damping in Section IV D the simulation parameters were $n_p = 32$, $\Delta x = \frac{2\pi}{kn_p}$, $n_v = 128$ and $v_{max} = 9v_{th}$ and periodic spatial boundary conditions. The time-step was automatically chosen to satisfy the CFL conditions. A large number of harmonics are required to correctly capture Landau damping (see Section IV D) so $l_{max} = 50$ was used. The electron temperature was uniform with $T_e = 50$eV and the background uniform ion density was $n_i = 10^{27}\mathrm{m}^{-3}$. The initial electron number density distribution was defined as

$$n_e = n_i\left(1 + \beta\sin(kx)\right) \tag{22}$$

where β is a scaler chosen to be 0.01. The corresponding initial electric field is

$$E = \frac{en_i\beta}{\epsilon_0 k}\cos(kx) \tag{23}$$

The wavevector was defined in terms of the Debye length, λ_D as $k = \frac{\alpha}{\lambda_D}$ and $\omega_{ph}$was obtained for $\alpha = 0.10, 0.15, 0.20, 0.25, 0.30, 0.35$ and 0.40. This samples the velocity distribution in the range $3v_{th} \rightarrow 10v_{th}$. The frequency was calculated by averaging over the first ten oscillations. Figure 3 shows the percentage difference between these frequencies and those predicted by eqn. (21) for each value of k. Where v_ϕ is closer to satisfying $v_\phi \gg v_{th}$ the difference is on the sub-percent level and increases as v_ϕ moves closer to v_{th}. Eqn. (21) relies on the correction to ω_{pc} being small but for $\alpha = 0.35$ it is more than 10% and more than 20% for $\alpha = 0.40$. This accounts for the large differences observed at these values of α.

D. Landau Damping

Eqn. (21) is invalid when $v_\phi \gg v_{th}$ no longer holds because of the phenomenon of Landau damping [9]. This is the process by which plasma waves in a collisionless, equilibrium plasma can become damped due to the exchange of energy from the wave to electrons with velocities slightly less than the resonance condition $v = v_\phi$. Electrons with velocities slightly larger than v_ϕ would transfer energy to the wave. Thus for the wave to be damped it is necessary that $\mathrm{d}f_0(v = \omega/k)/\mathrm{d}v < 0$.

The simulation was initialised as described in Section IV C with $\alpha = 0.5$. A parameter scan was performed to find the optimum set to model Landau damping accurately. This involved varying the resolution in $|\mathbf{v}|$ using $nv = 128, 256, 512$ and varying the number of harmonics using $l_{max} = 10, 30, 50$.

Taking as figure of merit, $\mathcal{R} = (v_{th}/\Delta v)/l_{max}$, i.e. the ratio of the resolution in $|\mathbf{v}|$ to the resolution in θ, it was found that modelling of Landau damping requires $\mathcal{R} \gtrsim 1$. Below this threshold damping may occur in an approximate fashion at early times and/or at a reduced rate or indeed not at all. Figure 4 gives a representative example of a Landau damping simulation that satisfies $\mathcal{R}$ in which the amplitude of the electric field in the centre

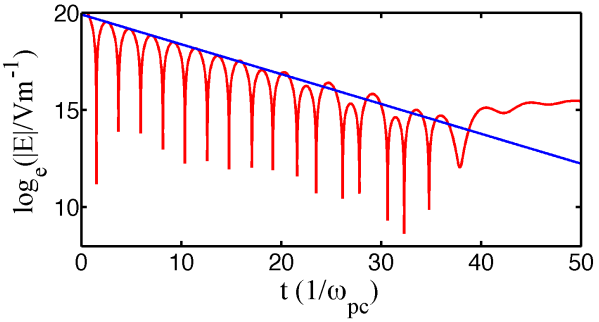

FIG. 4. Time evolution of the amplitude of the electric field in the centre of the domain for a simulation satisfying $\mathcal{R}$. The solid line represents the theoretical decay rate.

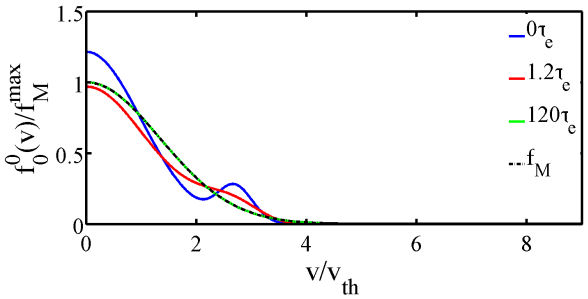

FIG. 5. The time evolution of a bump-on-tail distribution of electrons under the influence of electron-electron collisions. The distributions are normalised to the maximum of the final Maxwellian distribution characterised by a thermal velocity of $\sim 1.34 v_{th}$.

of the domain is shown. Here $n_v = 512$ and $l_{max} = 30$ were used.

The oscillation frequency, ω_r and damping rate, ω_i for the described configuration are given by [6] as $\omega_r = 1.41566\omega_{pc}$ and $\omega_i = 0.153359\omega_{pc}$. Taking Figure 4, ignoring the first period and averaging over the next six gives an error in ω_r of 0.03%. Performing linear regression on the peaks of these periods gives an error in ω_i of 1.6%. These results compare favourably with those presented in [6].

E. Electron-Electron Drag Term

Correct implementation of the electron-electron drag term in eqn. (13) is tested by following the evolution of a bump-on-tail distribution of electrons as it relaxes to Maxwellian distribution, f_M. The fundamental harmonic, f_0^0 was initialised as a Maxwellian characterised by thermal velocity v_{th}. A Gaussian bump was then added with its mean at $v = 2.7 v_{th}$ to give the distribution shown in blue in Figure 5. This was represented using $n_v = 512$ and $v_{max} = 9 v_{th}$ and was evolved for a period $\tau = 120\tau_e$ where $\tau_e = \left(3\sqrt{2\pi} v_{th}^3 \epsilon_0^2 m_e^2 / n_e e^4 \log\Lambda\right)$ is the characteristic relaxation time for a Maxwellian distribution undergoing electron-electron collisions as defined in [10]. A fixed time-step of $\Delta t = \tau_e/20$ was used.

Figure 5 shows similar behaviour to a qualitatively comparable test described in [10]. By $120\tau_e$ the distribution has relaxed to a Maxwellian distribution characterised by a thermal velocity of $\sim 1.34 v_{th}$. Over the simulation period energy was conserved to within 0.06%.

Quantitative confirmation that the electron-electron drag term has been correctly implemented will be obtained when the heat flow tests discussed in Section V are performed.

F. Electric Field Generation at a Density Gradient

Electrons will move to smooth out a density gradient in a uniform temperature plasma with a uniform background ion distribution. An electric field will be generated to oppose the ensuing charge imbalance and impose quasi-neutrality. Assuming the scale length of the density gradient is long compared to the Debye length, the generated electric field is given, to first order, by

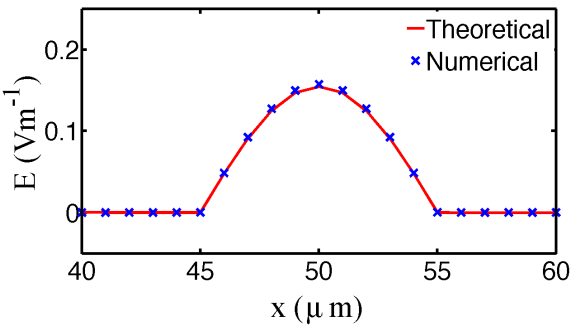

FIG. 6. The time-average electric field generated across a density gradient in a collisionless plasma after $20\tau_{pc}$ is in good agreement with the first order theory of eqn. (24).

$$E = -\frac{k_B T}{n_e e}\frac{\partial n_e}{\partial x} \tag{24}$$

where the ideal gas law has been used for the electron thermal pressure. In a collisionless system eqn. (24) gives a time-average electric field while in a collisional system it gives the final, steady state electric field required to maintain quasi-neutrality.

The plasma was initialised with a temperature, $T_e = 50$eV and ionic charge, $Z = 16$. The number density smoothly interpolates between a lower density of $n_e^L = 10^{27}\mathrm{m}^{-3}$ on the right of the domain up to a higher density of $n_e^H = n_e^L + 2\delta n_e \mathrm{m}^{-3}$ with $\delta n_e = 10^{-8} n_e^L \mathrm{m}^{-3}$. Such a plasma has a Debeye length, $\lambda_D = 1.66 \times 10^{-9}$m. Using $n_p = 100$, $\Delta x = 10^{-6}$m, the density gradient was spread over the middle ten cells giving a scale length of $\sim 10^{-5}$m. The domain was completed using $n_v = 512$ and $v_{max} = 9 v_{th}$ and reflective spatial boundary conditions. Simulations were performed over a period of $20\tau_{pc}$ using $l_{max} = 5$.

Figure 6 compares the electric field profile given by eqn. (24) and the simulated, spatially resolved time-averaged electric field for a collisionless plasma. The wings of the profile have been removed to highlight the gradient region. The average percentage difference between the profiles across the gradient region is ∼1.9%. After the same simulation period the final electric field generated in a collisional system has a difference of ∼2.4%.

V. FORTHCOMING VALIDATION

Infinite velocity distributions are represented on a finite grid in the Model under the assumption that the grid is large enough to contain the majority of the distribution and that $f \to 0$ as $v \to \infty$. This inevitably leads to a discontinuity at the upper boundary for any truly infinite distribution. This may be having an impact on the energy conservation of the Model since a significant improvement in the energy conservation in Section IV E was observed when the boundary was moved from $5v_{th}$ to $9v_{th}$ while increasing n_v from 256 to 512. The energy conservation improved from 2.6% to 0.06%. This is understandable since the internal energy is a strong function of $|\mathbf{v}|$.

The proposal is to change the upper boundary condition from $f \to 0$ as $v \to \infty$ to $\partial f/\partial v \to 0$ as $v \to \infty$. This by definition will remove the discontinuity and may lead to improved energy conservation on smaller grids and in turn reduce runtimes.

A test case that is intended to test the Model working in its entirety will focus on reproducing classical Spitzer heat flow. This will involve initialising uniform density electron and ion distributions while imposing a temperature gradient in the electron distribution with a scale length much longer than the mean free path of the electrons. The evolving system will generate a heat flux which will be measured and compared to Spitzer theory. It is likely that these simulations will be initialised to closely match those in [10] so that a comparison can be made.

VI. CONCLUSIONS

The structure of a 1d2v Vlasov-Fokker-Planck model suitable for tackling problems of electron transport relevant to inertial confinement fusion has been described. It represents velocity space as an expansion in spherical harmonics and can include an arbitrary number of harmonics to sufficiently resolve details in velocity space. It is capable of simulating electric fields in the x- and y-directions and a magnetic field in the z-direction.

An extensive suite of tests has been conducted to validate the Model and it has performed well in all cases. Improvements can most likely be achieved by tweaking simulation parameters to increase resolution in x, $|\mathbf{v}|$ or in time but at the expense of runtime. The results from the Landau damping test (Sections IV D) are particularly noteworthy as reproducing Landau damping is widely regarded as a challenging test for any Vlasov solver.

It is expected that the Model will perform suitably well in the final validation tasks, at which time the Model will be finalised and ready for use.

[1] J. Nuckolls, L. Wood, A. Thiessen, and G. Zimmerman, Nature **239** (1972).

[2] R. Kodama, P. A. Norreys, K. Mima, A. E. Dangor, R. G. Evans, H. Fujita, Y. Kitagawa, K. Krushelnick, T. Miyakoshi, N. Miyanaga, T. Norimatsu, S. J. Rose, T. Shozaki, K. Shigemori, A. Sunahara, M. Tamp, K. A. Tanaka, K. A. Toyama, T. Yamanaka, and M. Zepf, Nature **412** (2001).

[3] M. Tabak, J. Hammer, M. E. Glinsky, W. L. Kruer, S. C. Wilks, J. Woodworth, E. M. Campbell, and M. D. Perry, Phys. Plasmas **1** (1994).

[4] R. Betti, C. D. Zhou, K. S. Anderson, L. J. Perkins, W. Theobald, and A. A. Solodov, Phys. Rev. Lett. **98** (2007).

[5] A. R. Bell, A. P. L. Robinson, M. Sherlock, R. J. Kingham, and W. Rozmus, Plasma Phys. Control. Fusion **48** (2006).

[6] T. D. Arber and R. G. L. Vann, J. Comput. Phys. **180** (2002).

[7] J. S. Chang and G. Cooper, J. Comput. Phys. **6**, 1 (1970).

[8] A. B. Landon, "CECAM report of workshop on the flux limiter and heat flow instabilities in laser-fusion plasmas," (Universite Paris Sud, France, 1981) p. 69.

[9] L. D. Landau, J. Phys. USSR **10**, 574 (1946).

[10] M. Tzoufras, A. R. Bell, P. A. Norreys, and F. S. Tsung, J. Comput. Phys. **230**, 6475 (2011).

[11] C. K. Li, F. H. Séguin, J. R. Rygg, J. A. Frenje, M. Manuel, R. D. Petrasso, R. Betti, J. Delettrez, J. P. Knauer, F. Marshall, D. D. Meyerhofer, D. Shvarts, V. A. Smalyuk, C. Stoeckl, O. L. Landen, R. P. J. Town, C. A. Back, and J. D. Kilkenny, Phys. Rev. Lett. **100**, 225001 (2008).

[12] P. A. Amendt, J. L. Milovich, S. C. Wilks, C. K. Li, R. D. Petrasso, and F. H. Séguin, Plasma Phys. Control. Fusion **51**, 12 (2009).

Approximating the dynamic structure factor in warm dense matter

N. J. Hartley and G. Gregori
Department of Physics,
Clarendon Laboratory,
University of Oxford,
Oxford,
OX1 3PU
nicholas.hartley@physics.ox.ac.uk

Introduction

Warm dense matter (WDM) is a statewhich naturally occurs in planetary interiors, mainly in Jovian plants, but it also formed in the interaction of high-power lasers with matter. It is distinguished by its temperature, generally a few eV, and the fact that it is at approximately solid density, so it is crucial in the inital heating of an ICF capsule. In probing the conditions within this laser-produced matter, the dynamic structure factor (DSF) is a quantity of paramount importance. In the same way that simple Bragg diffraction probes the reciprocal space lattice, Thomson scattering observed from dense plasmas probes the form of the DSF (for a complete description of this, see [1]).

The classical one-component plasma (OCP) is a model well-suited to describing matter under the extreme conditions considered here. It considers a system of identical point charges with Coulomb interactions, surrounded by a uniform background of opposite charge. Its properties are well described by the strong plasma coupling parameter, $\Gamma = (Ze)^2/ak_BT$, where $a = (\frac{4\pi n}{3})^{-1/3}$ the average interparticle separation [2].

While for small Γ such as those in an ideal plasma, a simple collisionless mode described by the Vlasov equation can be used, in WDM where $\Gamma \sim 1$, modifications known as local field corrections must be included, complicating the model. Therefore, in this paper a model developed by Hansen [3] and others, known as the memory function approach, will be utilised instead, to give results which can span a range of different k, Γ points.

1 The Memory Function

The memory function approach is most often used in hydrodynamic descriptions, and describes how the behaviour of a fluid at one point in space and time depends on those that have come before it through a convolution of the memory function with the relevant correlation function. For this reason, the Laplace transform of the memory function, $\phi(k,\omega) = \phi'(k,\omega) + i\phi''(k,\omega)$, is normally used [4], as will be seen later.

We start with the definition of the density response function (DRF), which defines how the density at one point in the plasma depends on that at another point in space and time (see e.g. [2]).

$$\chi(k,\omega) = \frac{k^2 n/m}{\omega^2 - \omega_k^2 + i\omega k^2 \phi(k,\omega)} \qquad (1)$$

where $\omega_k^2 = \Omega_2/\Omega_0$ in terms of frequency mo-

ments.

This quantity is closely related to the dynamic structure factor by the fluctuation-dissipation theorem [5]:

$$S(k,\omega) = -\frac{k_B T}{\pi n \omega}\Im\{\chi(k,\omega)\} \tag{2}$$

Hansen [3] was the first to suggest a Gaussian ansatz for the memory function, which we will use here

$$\begin{aligned} k^2\phi(k,t) &= k^2\phi(k,0)\exp(-\pi t^2/4\tau_k) \\ &= \Omega_p^2 \exp(-\phi t^2/4\tau_k) \end{aligned} \tag{3}$$

In this expression, τ_k is the relaxation time, which is defined seperately from the memory function model, and $\Omega_p^2 = (\Omega_4/\Omega_2) - (\Omega_2/\Omega_0)$, with the frequency moments Ω_n given by

$$\Omega_n = \int_{-\infty}^{\infty} \omega^n S(k,\omega) d\omega \tag{4}$$

The simplest frequency moment $\Omega_0 = \int_{-\infty}^{\infty} S(k,\omega)d\omega = S(k)$ is known as the static structure factor (SSF). Analytic desriptions of higher frequency moments are taken from [6], with quantum corrections ignored.

We take the Laplace transform of Equation 3 to obtain the following expressions for the real and imaginary parts of the memory function

$$k^2\phi'(k,\omega) = \Omega_p^2 \tau_k e^{-\tau_k^2\omega^2/\pi} \tag{5a}$$

$$k^2\phi''(k,\omega) = \Omega_p^2 D(\tau_k\omega/\sqrt{\pi}) \tag{5b}$$

Substituting these expressions for the memory function into Equation 1 gives us a new expression for the DRF in this memory function approach.

$$\chi(k,\omega) = \frac{k^2 n/m}{\omega^2 - \omega_k^2 - \Omega_p^2\left(2xD(x) - i\sqrt{\pi}xe^{-x^2}\right)} \tag{6}$$

where $x = \tau_k\omega/\sqrt{\pi}$ and we recall that $\omega_k^2 = k^2 v_t^2 \frac{1}{S(k)}$.

Returning to the fluctuation-dissipation theorem, Equation 2, we find an expression for the DSF.

$$S(k,\omega) = \frac{\frac{1}{\pi}k^2 v_t^2 \Omega_p^2 \tau_k e^{-x^2}}{[\omega^2 - \omega_k^2 - \Omega_p^2 2xD(x)]^2 + [\Omega_p^2\sqrt{\pi}xe^{-x^2}]^2} \tag{7}$$

A simple expression for the relaxation time can be derived from the random phase approximation, but this was found to give incorrect limiting behaviour for the DSF. Instead, the quantity described in [6], given in terms of frequency moments, was used.

$$\begin{aligned} \tau_k^2 &= \frac{\Omega_p^2}{2\left(\Omega_6/\Omega_2 - \omega_L^4\right)} \\ &= \frac{k^2 v_t^2}{\omega_p^2\left(1+3k^2v_t^2\right)^2\left[\frac{3k^2v_t^2+1}{3k^2v_t^2+3} - \frac{1}{3}\right]} \end{aligned} \tag{8}$$

2 Static Structure Factor

The form of $S(k,\omega)$ still depends on how we calculate the SSF, $S(k)$. Previously, it was found from molecular dynamics (MD) simulations [7]. What we would like to do instead, though, is find an analytic expressions for $S(k)$ which can recreate the MD results without such a computationally intensive method.

The difficulty with this is that as there are many restrictions on the properties of the SSF. While its limits are well understood - it approaches unity as $k \to \infty$ and goes to k^2/k_D^2 as $k \to 0$ [8] - how it approaches these limits is more challenging. Its behaviour in these limits is so crucial because it appears in an integral to calculate the correction to the fourth moment Ω_4, as described in [9]. This integral takes the form

$$I(k) = -A\int_0^{\infty} dq\, q^2(S(q)-1)J(q,k) \tag{9}$$

The simplest model for the SSF is the Debye form

$$S(k) = \frac{k^2}{k^2 + k_D^2}$$

with k_d the inverse Debye length. The problem with this form is that it approaches unity too slowly as $k \to \infty$, giving an integral which does not converge. This leads us to introduce an exponential term, with the choice of exponent motivated by the characteristic length scale of the problem.

$$S_0(k) = \frac{k^2}{k^2 + k_D^2 e^{-k^2/k_D^2}} \tag{10}$$

While this does allow the integral to converge, $S(k)$ remains unphysical as the peaked sturcture factor, characteristic of coupled plasmas, is absent. However, a further approximation is suggested by Chaturvedi et. al. [10], giving

$$S_1(k) = \frac{S_0(k)}{1 - f(k)S_0(k)} \tag{11}$$

A first approximation gives $f(k) = (k_D/k)^4$, as described in [11], but this does not approximate to k^2/k_D^2 as $k \to 0$, so a further exponential is introduced to correct this.

$$f(k) = \left(\frac{k_D}{k}\right)^4 \left(1 - e^{k^2/k_D^2}\right)^2$$

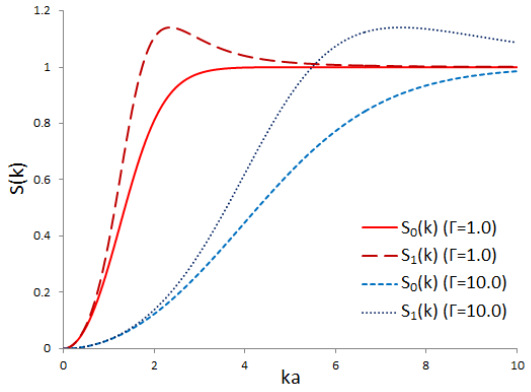

Figure 1: *$S(k)$ as calculated from* (10) *and* (11)

As can be see from Figure 1, this form of the SSF has a peak at which $S(k) > 1$, instead of monotonically increasing for all k. While this could be more physically accurate, we find that the DSF derived from it does not agree with MD data.

3 Further Work

Using (7), the DSF can be modelled for different values of k, Γ and using different approximations for $S(k)$. These can then be integrated, in this case using a Gaussian quadrature method, to give an improved result for the SSF. Throughout this modelling, the SSF derived by integrating the DSF always agreed with the original approximation used for the SSF, indicating that the method is numerically robust.

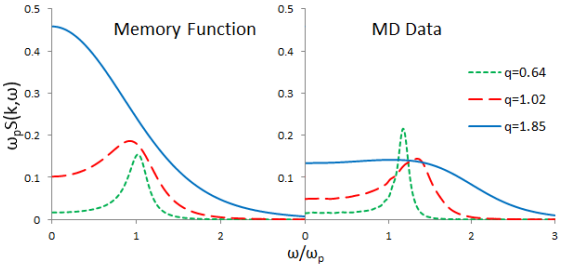

Figure 2: *Values for the DSF, calculated with* $\Gamma = 1$ *in* (7)*, and MD data taken from Mithen [7]*

Figure 2 shows a comparison of results from using the memory function model described here and those obtained from MD simulations. In both cases we can see the peak broaden and decrease in height as we increase $q = ka$, as expected. The significant difference, though, is the difference in the absolute height, which is due to the difference in the size of $S(k)$ used in the memory function. It seems that the model for $S(k)$ used here, (11), overestimates the size of the peak at low Γ; work by Hamaguchi [12] suggests that the peak in the static structure factor may not appear until $\Gamma \sim 50$, which is a much greater coupling strength than is examined here. Therefore, finding more appropriate model for $S(k)$ will be a priority in continuing with this work.

Acknowledgements

The author would like to thank James Mithen for the MD data used in this paper.

References

[1] S. H. Glenzer and R. Redmer. X-ray Thomson scattering in high energy density plasmas. *Reviews of Modern Physics*, 81(4):1625–1663, December 2009.

[2] J. P. Hansen and I. R. McDonald. *Theory of Simple Liquids*, volume 2nd. Academic Press, 2006.

[3] J. P. Hansen, I. R. McDonald, and E. L. Pollock. Statistical mechanics of dense ionized matter III. *Physical Review A*, 11(3):1025–1039, 1975.

[4] S Ranganathan and S Yip. Memory functions for kinetic theory models of density fluctuations in fluids. *Physica A: Statistical and Theoretical Physics*, pages 127–139, 1980.

[5] S. Ichimaru, S. Mitake, S. Tanaka, and X.-Z. Yan. Theory of interparticle correlations in dense, high-temperature plasmas. *Physical Review A*, 32(3), 1985.

[6] G. Gregori and D. O. Gericke. Low frequency structural dynamics of warm dense matter. *Physics of Plasmas*, 16(5), 2009.

[7] J. P. Mithen, J. Daligault, and G. Gregori. Comparative merits of the memory function and dynamic local-field correction of the classical one-component plasma. *Physical Review E*, 85(5):1–9, May 2012.

[8] M. Baus and J. P. Hansen. Statistical mechanics of simple coulomb systems. *Physics Reports*, 59(1):1–94, 1980.

[9] A. A. Kugler. Theory of the Local Field Correction in an Electron Gas. *Journal of Statistical Physics*, 12(1), 1975.

[10] D. K. Chaturvedi, M. Rovere, G. Senatore, and M. P. Tosi. Liquid alkali metals and alloys as electron-ion plasmas. *Physica 111B*, pages 11–23, 1981.

[11] E. García Saiz, G. Gregori, D. O. Gericke, J. Vorberger, B. Barbrel, R. J. Clarke, R. R. Freeman, S. H. Glenzer, F. Y. Khattak, M. Koenig, O. L. Landen, D. Neely, P. Neumayer, M. M. Notley, A. Pelka, D. Price, M. Roth, M. Schollmeier, C. Spindloe, R. L. Weber, L. van Woerkom, K. Wünsch, and D. Riley. Probing warm dense lithium by inelastic X-ray scattering. *Nature Physics*, 4(12):940–944, October 2008.

[12] S. Hamaguchi, R. T. Farouki, and D. H. E. Dubin. Phase diagram of Yukawa systems near the one-component-plasma limit revisited. *The Journal of Chemical Physics*, 105(17):7641, 1996.

The Effect of Temporal Pulse Shape in Simulating the Interaction of an Intense Laser Pulse and an Ultra-thin Foil

Contact *ceri.brenner@stfc.ac.uk*

R. Heywood[*], C. M. Brenner, A. P. L. Robinson and D. Neely

Central Laser Facility, STFC, Rutherford Appleton Laboratory, Didcot, OX11 0QX, UK

[*]*Lord Wandsworth College, Long Sutton, Hook, Hampshire, RG29 1TB*

J. Pasley

Department of Physics, University of York, Heslington, York, YO10 5DD, UK

Introduction

Laser driven particle acceleration is a burgeoning area of high power laser research that is being investigated by many groups worldwide. The huge interest in this field is driven by the extensive potential applications that a controllable, high-energy ion beam would have. For example, these beams could be employed in a novel variant of hadron therapy: a cancer treatment in which high energy ions are used to destroy cancerous tumours. The advantage of ions over the more conventional x-rays is that they have a fixed stopping distance and also a high proportion of their energy is deposited at the end of their range in the Bragg peak. Consequently, the surrounding cells are irradiated less. Currently, hadron therapy can be carried out with a conventional particle accelerator but, due to the size and cost of these accelerators, there are only a limited number of facilities in operation. Conversely, laser driven particle accelerators would be far more compact and could be cheaper, making this procedure far more convenient [1]. Controllable, high-energy ion beams also have potential applications in the fast ignition method of inertial confinement fusion as well as in isotope production [2, 3]. However, if these applications are to be realized using laser-based sources, then the technique for producing these ion beams needs to be perfected, particularly in terms of the maximum ion energy and the distribution of energy in the proton energy spectrum [4].

Following the development of chirped pulse amplification (CPA) technology in the late twentieth century, a great deal of research has taken place into the acceleration of ions to multi-MeV energies using lasers with intensities of 10^{18}-10^{20} W/cm^2 [5]. It is accepted that Target Normal Sheath Acceleration (TNSA) is the dominant mechanism for ion acceleration in this intensity regime [6]. In this mechanism, hot electrons are accelerated by the laser and propagate through the target before escaping from the rear. However, a strong electrostatic field (~10^{12}V/m) is caused by this charge separation [7]. This draws the majority of the electrons back to the rear end of the target while also accelerating the ions to multi-MeV energies in a very short time period (~ps). The acceleration of ions with a high charge to mass ratio is favored and therefore protons are often the accelerated ions. While the ions accelerated through TNSA display many desirable qualities, such as high brightness, very low emittance and short pulse duration [8], several factors affect the prospects of ion beams driven by TNSA: they tend to have a low production efficiency and a wide distribution of energies.

In this report, 1D Particle-In-Cell (PIC) simulations will be used to model the interaction between a variety of laser pulses and a polypropelene target. Each laser pulse will have a different wave envelope and the effect of these different wave envelopes on the proton energy spectrum will be investigated. In addition to this, the effect of the pulses on the coupling efficiency will also be explored. This investigation will allow simulations to be run in the future with a greater knowledge of how the wave envelope affects the interaction. Furthermore, if it is found that the pulse shape makes a significant difference to the interaction, it may be suggested that this should be investigated in 2D and then using a real laser to see whether the effects are real and whether such modification might result in an approach that is better suited to the applications of laser-driven ion beams.

Simulation Setup

The simulations were conducted using the 1D PIC code described in [9]. They were setup to simulate the interaction between an 800 nm, intense laser pulse from the Astra laser at the Central Laser Facility and a polypropelene (C_3H_6) target. Polypropelene is the polymer that is most frequently used as a target material in such experiments. The target used was 25 nm thick, making it ultra-thin, and had a sharp density profile. The electron number density of the polypropelene is $1.2\text{x}10^{29}\text{m}^{-3}$ and the critical density was $1.75\text{x}10^{27}\text{m}^{-3}$, and therefore the electron number density was 70 times the critical density initially. In each simulation, the wave envelope of the laser pulse was changed. In total, six different wave envelopes were used: a Gaussian, Super Gaussian (with an index of four), Sine, Sine^3, Sech^2 and a Top Hat. These pulses were chosen because they covered a broad range of possible pulse shapes. The shape of the electric field created by each pulse is shown below in figure 1.

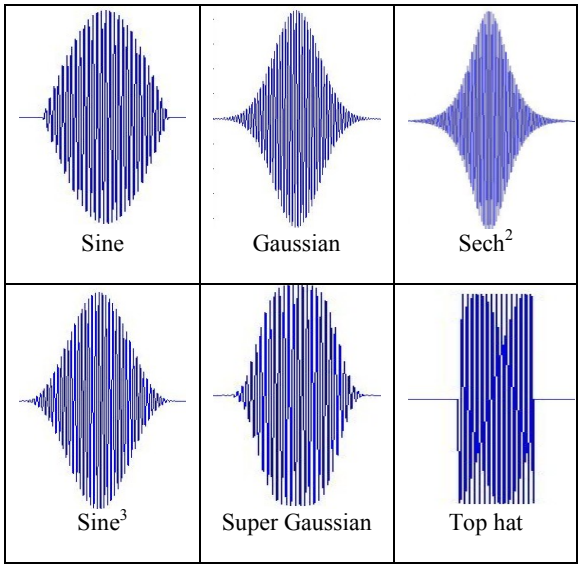

Fig.1 The six different pulse shapes employed in the simulations described in this paper.

While the wave envelope of the laser pulse changed each time, all of the laser pulses were linearly polarized and had a wavelength of 800nm. The duration of all of the laser pulses was ~ 40fs.

Results

Initially, the effect of changing the intensity of the pulse was investigated. This was done using both a $Sech^2$ pulse and a Gaussian pulse and the parameters described previously. The intensity was varied between $5x10^{17}W/cm^2$ and $5x10^{19}W/cm^2$. The results, illustrated below in figure 2, conclusively show that the coupling efficiency is highly dependent on intensity in a 1D particle-in-cell simulation with the parameters described in this report.

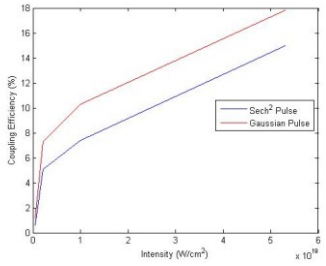

Fig.2 The coupling efficiency as a function of intensity in a 1D particle-in-cell simulation.

However, experimentally, it has been seen that the intensity has only a very limited effect on the coupling efficiency in the ultrahigh contrast interaction conditions. This is shown by figure 3, which clearly demonstrates that the effect described above is far greater than has been found to occur experimentally.

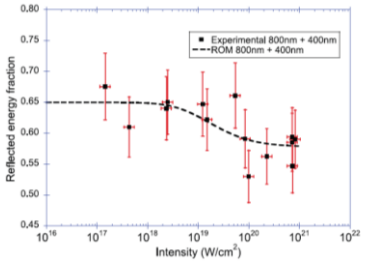

Fig.3 From [10], the percentage of reflected energy as a function of intensity.

These figures reveal that there is an imperfection in the code that leads to the coupling efficiency having a much higher dependency on the intensity than has been observed experimentally. This is likely to be due to the fact that many of the absorption mechanisms apparent in experiments cannot be modeled in one dimension, such as resonant and vacuum absorption.

This result is reinforced when simulations are run with different pulse shapes that all have the same input energy density ($1.6J/m^2$). Figure 4 shows the results of these simulations, and it reveals that the absorption of all the pulses is quite different. For instance, the coupling efficiency of the pulses varied from 8.8% for the $Sech^2$ pulse up to 10.7% for the Top Hat Pulse. Furthermore, it is clear that the shorter pulses, which contained a greater proportion of their energy in regions of high intensity, had higher coupling efficiencies than the longer pulses, which contained more of their energy in regions of low intensity. Consequently, these results also imply that the absorption is higher at higher intensities.

Wave Envelope	Top Hat	Super Gaussian (index 4)	Sine	$Sine^3$	Gaussian	$Sech^2$
Absorbed Energy Density (J/m^2)	0.17	0.17	0.16	0.15	0.15	0.14
Coupling Efficiency (%)	10.7	10.4	9.8	9.4	9.2	8.8
Maximum Proton Energy (MeV)	8.36	7.75	7.45	7.24	7.05	6.90

Fig.4 The first set of simulation results for each of the six pulse shapes.

Consequently, in order to see the affect the pulse shape actually has, this effect must be compensated for. This was done by adjusting the input energy so that the absorbed energy was constant for all of the pulse shapes. When these simulations are carried out, the simulation results are almost identical for each of the pulse shapes. These results are shown in figure 5. Figure 6 also demonstrates this, as the proton energy spectrums for all of the pulse shapes are incredibly similar.

Wave Envelope	Top Hat	Super Gaussian (index 4)	Sine	$Sine^3$	Gaussian	$Sech^2$
Input Energy Density (J/m^2)	1.52	1.56	1.60	1.68	1.76	1.74
Absorbed Energy Density (J/m^2)	0.164	0.162	0.157	0.157	0.161	0.159
Coupling Efficiency (%)	10.82	10.38	9.76	9.34	9.12	9.13
Maximum Proton Energy (MeV)	8.2	7.7	7.5	7.4	7.5	7.3

Fig.5 The second set of simulation results for each of the six pulse shapes.

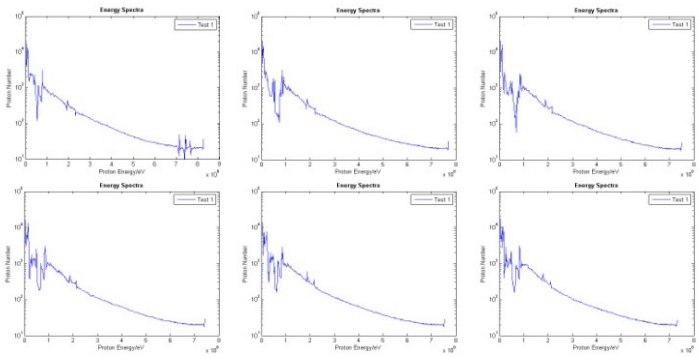

Fig.6 The proton energy spectrums from each of the six pulse shapes. Form top left clockwise: Top Hat, Super Gaussian, Sine, $Sech^2$, Gaussian and $Sine^3$.

Conclusions

On initial inspection it appears that for pulses with duration of ~ 40fs, the pulse shape may have an effect on the simulation results in a 1D particle-in-cell simulation. However, this is a purely artificial result caused by the inability of the 1D simulation code to correctly reproduce the scaling of the absorption fraction as a function of laser intensity. With further investigation, it is clear that once this effect has been compensated for, the temporal pulse shape has a negligible effect on the simulation results. This suggests that, for a given amount of absorbed energy, the simulation code is predominantly impulsive for time scales of the order investigated in this report (~ 40 fs). Since the pulse duration is short in comparison with the plasma expansion time, it seems that the absorption of energy by the plasma is almost instantaneous, implying that the pulse shape will have little effect on the resultant proton spectra. However, this may not be the case if pulses with a longer duration were investigated in the same way. If these pulses were long enough for hydrodynamic effects to take place (~1ps), the shape of the pulse may have a greater effect on the proton energy spectrum. While it was not possible to explore these pulse lengths in this report due to computational constraints, an investigation into this in the future may give further insight into how the pulse shape affects the pulses interaction with the target foil.

Acknowledgements

The authors would like to acknowledge the support of the Nuffield Foundation Science Bursary with special thanks to J. Lewis for coordinating the placement as part of the Education and Outreach activities of STFC. The authors would also like to extend their thanks to everyone involved in the project at the Central Laser Facility. Your help and support was much appreciated.

References

1. D C Carrol, "*Laser-Drive Ion Acceleration: Source Optimisation and Optical Control"* PhD Thesis 2008
2. C A J Palmer *et al., "Petawatt laser ion acceleration with nanometer scale diamond-like carbon targets",* CLF Annual Report 2008-2009.
3. D C Carroll *et al., New Journal of Physics* **12** 045020 (2010).
4. R Prasad *et al.,"Proton/ion energy scaling and laser conversion efficiency using 50fs, 10^{20}-10^{21} W/cm^2 Astra-Gemini pulses",* CLF Annual Report 2009-2010.
5. A P L Robinson *et al., Phys. Rev. Lett.* **96** 035005 (2006).
6. S C Wilks *et al., Physics of Plasmas* **8**, 542 (2001)
7. M Borghesi *et al.,"Radiation Pressure effect on ion Acceleration on the GEMINI laser",* CLF Annual Report 2009-2010
8. O Tresca *et al., "Ion acceleration from foil targets in the ultraintense ultrahigh contrast regime"* CLF Annual Report 2009-2010
9. A P L Robinson *et al., New Journal of Physics* **10** 013021 (2008).
10. M J V Streeter *et al., New Journal of Physics* **13** 023041 (2011).

Corrections to Laser Electron Thomson scattering

Contact: *theinzl@plymouth.ac.uk*

Thomas Heinzl
School of Computing and Mathematics
Plymouth University
Drake Circus, Plymouth PL4 8AA, UK

Anton Ilderton
Department of Physics
Umeå University
SE-901 87 Umeå, Sweden

1 Introduction

Thomson scattering is the classical process of light being deflected by a charged obstacle of typical size smaller than the wavelength of the incident radiation. For definiteness we will henceforth assume the charge to be an electron and the incoming wave stemming from a laser beam. The scattered radiation may be viewed as resulting from a two-step process: (i) the acceleration of the charge due to the electromagnetic field it encounters and (ii) the bremsstrahlung emitted in consequence. The radiated power is then given by Larmor's formula which, in its nonrelativistic incarnation and using Heaviside-Lorentz units, reads

$$P_{\rm rad} = \frac{2}{3}\frac{e^2}{4\pi c^3}\dot{\mathbf{v}}^2 \,. \tag{1}$$

Expressing the acceleration by means of the nonrelativistic Lorentz force (neglecting the $\mathbf{v}\times\mathbf{B}$ term), $m\dot{\mathbf{v}} = e\mathbf{E}$, $\mathbf{E}$ being the electric field of the incoming wave, the radiated power becomes

$$P_{\rm rad} = \frac{2}{3}\frac{e^4}{4\pi m^2 c^3}E^2 \,. \tag{2}$$

This may be turned into a cross section (units of area) upon dividing by the energy flux, i.e. the modulus of the Poynting vector, which for a *plane wave* (PW) is

$$S = c\,|\mathbf{E}\times\mathbf{B}| \overset{\rm PW}{=} cE^2 \,. \tag{3}$$

Hence, we obtain the Thomson cross section,

$$\sigma_{\rm Th} := \frac{P_{\rm rad}}{S} = \frac{8\pi}{3}\left(\frac{e^2}{4\pi mc^2}\right)^2 =: \frac{8\pi}{3}r_e^2 \,, \tag{4}$$

with the classical electron radius, $r_e \simeq 3$ fm. At this distance, the Coulomb energy between electrons equals mc^2, and (with the benefit of hindsight) one ends up with a distance scale that is actually typical for strong interactions (1 fm being roughly the nucleon size). As a result, the Thomson cross section takes on the numerical value $\sigma_{\rm Th} \simeq 6.6\times 10^{-24}$ cm$^2 \simeq 0.66$ barn which is not small by particle physics standards.

It is instructive to rederive (4) in a fully covariant way. The radiated power may be inferred from the proper time derivative of the wave 4-momentum which can be expressed in terms of the electron 4-velocity u^μ [1],

$$\dot{P}^\mu = -\frac{2}{3}\frac{e^2}{4\pi c^5}\dot{u}^2 u^\mu \,. \tag{5}$$

Dotting in u, using $u^2 = c^2$ and the covariant equation of motion, $m\dot{u}^\mu = (e/c)F^{\mu\nu}u_\nu$, one finds the radiated power,

$$P_{\rm rad} = u\cdot\dot{P} = \sigma_{\rm Th}u_\mu F^{\mu\alpha}F_\alpha{}^\nu u_\nu/c =: \sigma_{\rm Th}w_0 \,. \tag{6}$$

For a plane wave (or, more general, null field), the square of the field strength tensor coincides with the energy-momentum tensor,

$$F^{\mu\alpha}F_\alpha{}^\nu \overset{\rm PW}{=} cT^{\mu\nu} \,, \tag{7}$$

so that w_0 in (6) may be interpreted as the energy flux density of the electromagnetic wave as 'seen' by the electron in its instantaneous rest frame.

A plane wave moving in z direction with wave 4-vector $k^\mu = (1,0,0,1)$ will only depend on the invariant phase variable $\phi := k\cdot x$. Introducing the gauge potential A^μ via $F^{\mu\nu} = k^\mu A'^\nu - k^\nu A'^\mu$ (the prime denoting a ϕ derivative) we can write the energy momentum tensor (7) as

$$T^{\mu\nu} \overset{\rm PW}{=} -A'^2\,k^\mu k^\nu \,, \tag{8}$$

where we have chosen Lorentz gauge, $\partial_\mu A^\mu = k\cdot A' = 0$.

The result (6) yields a nice expression for the Thomson cross sections in terms of Lorentz invariants,

$$\sigma_{\rm Th} = \frac{u\cdot\dot{P}}{u_\mu T^{\mu\nu}u_\nu} \,, \tag{9}$$

the numerator and denominator being the field energy rate of change and flux density in the co-moving frame of the electron, respectively.

The differential cross section may be derived in a similar vein. For this one needs the angular distribution of the radiated power (1) in direction $\mathbf{l}$ which is [2]

$$\frac{dP_{\rm rad}}{d\Omega} = \frac{e^2}{(4\pi)^2c^3}(\mathbf{l}\cdot\dot{\mathbf{v}})^2 \,, \tag{10}$$

or, upon employing the equation of motion, with $\mathbf{E} = E\boldsymbol{\epsilon}$,

$$\frac{dP_{\rm rad}}{d\Omega} = \frac{e^4}{(4\pi)^2m^2c^3}E^2\left(1-(\mathbf{l}\cdot\boldsymbol{\epsilon})^2\right) \,. \tag{11}$$

Averaging over polarisations and introducing the scattering angle θ one has

$$\langle 1-(\mathbf{l}\cdot\boldsymbol{\epsilon})^2\rangle_{\rm pol}=\frac{1+\cos^2\theta}{2}\ . \tag{12}$$

This angular dependence was originally found by Thomson when calculating the mean "rate at which energy is streaming through unit area" [3]. Dividing by the incoming flux, $S=cE^2$, finally yields the differential cross section,

$$\frac{d\sigma_{\rm Th}}{d\Omega}=\tfrac{1}{2}r_e^2\,(1+\cos^2\theta)\ . \tag{13}$$

Integrating over angles we reobtain (4). Clearly, the differential cross section is more useful in general as it conveys more, namely spectral, information.

2 Radiation reaction

The two-step procedure mentioned in the introduction breaks down when the energy loss due to radiation becomes substantial such that the produced radiation field back-reacts on the 'external' incoming field and hence on the particle motion. In this case, one has to solve a modified equation of motion taking back-reaction into account and named after Lorentz, Abraham and Dirac (LAD) [5, 6, 7] . Introducing the time parameter

$$\tau_0:=\frac{2}{3}r_e/c\simeq 10^{-23}{\rm s}\ , \tag{14}$$

it is most compactly written as [1]

$$m\dot u^\mu=F^\mu+\tau_0\,m\ddot u^\mu=\frac{e}{c}F^{\mu\nu}u_\nu+\tau_0\,m\ddot u^\mu\ . \tag{15}$$

This equation, being third order in time derivatives ($\ddot u=\dddot x$), has pathological features such as runaway solutions and preacceleration which can be traded for each other but not entirely removed while insisting on (15) – see the lucent discussion in [8]. The loophole is to modify the equation via iteration, i.e. by expressing $m\ddot u$ on the right-hand side in terms of the Einstein-Lorentz force, $m\ddot u=\dot F^\mu+O(\tau_0)$ which yields the Landau-Lifshitz equation [9]

$$m\dot u^\mu=F^\mu+\tau_0\,m\dot F^\mu+O(\tau_0^2)\ . \tag{16}$$

This equation has been rigorously rederived using adiabatic perturbation theory [10] or a sophisticated classical regularisation procedure [11].

Clearly, either equation must lead to a modification of the Thomson cross section. This has already been worked out in Dirac's seminal paper [7] who found the following simple result,

$$\sigma_{\rm RR}=\frac{\sigma_{\rm Th}}{1+\frac{4}{9}(\omega_0\tau_0)^2}\ . \tag{17}$$

Here we have introduced the laser frequency $\omega_0:=\dot\phi=k\cdot u$ in the instantaneous rest frame. Assuming that our equations of motion both receive corrections of order τ_0^2 we should rewrite the cross section as

$$\sigma_{\rm RR}=\sigma_{\rm Th}\,\left(1-\tfrac{4}{9}\omega_0^2\tau_0^2\right)\ . \tag{18}$$

The cross section (17) may alternatively be obtained by considering an electron harmonically bound with a damping constant δ, i.e. subject to an additional damping force, $\mathbf{F}_{\rm RR}=-\delta m\mathbf{v}$. Writing (1) as $P_{\rm rad}=-\mathbf{F}_{\rm RR}\cdot\mathbf{v}$ we can identify

$$\delta=\frac{2}{3}\omega_0^2\tau_0\ . \tag{19}$$

This turns (17) into

$$\sigma_{\rm RR}=\frac{\sigma_{\rm Th}}{1+\delta^2/\omega_0^2}\ , \tag{20}$$

which is precisely the cross section for scattering off bound charges when $\omega_{\rm res}\ll\delta\ll\omega_0$, i.e. for large frequencies off resonance (see [2], Ch. 45).

For a later comparison with the quantum effects it is useful to rewrite the small parameter $\omega_0\tau_0$ in terms of the fine structure constant, $\alpha=e^2/4\pi\hbar c$, and the dimensionless parameter

$$\nu_0=\frac{\hbar k\cdot p}{m^2c^2}=\frac{\hbar\omega_0}{mc^2}=\frac{\hbar e^\zeta\omega}{mc^2}\ , \tag{21}$$

which measures the energy of the laser photons (as seen by the electron) in units of the electron rest mass. In the last expression we have introduced rapidity ζ via the electron gamma factor, $\exp\zeta=\gamma(1+\beta)$, to write ν_0 in terms of the lab frequency, ω. Obviously, one has

$$\omega_0\tau_0=\alpha\nu_0\ , \tag{22}$$

where the factors of $\hbar$ cancel on the right-hand side as they must for a purely classical parameter. Let us estimate the magnitude of this quantity for a relativistic electron ($\beta\simeq 1$) colliding with an optical laser [12, 13]. In this case one has $\nu:=\hbar\omega/mc^2\simeq 10^{-6}$ and $e^\zeta\simeq 2\gamma$. Thus, $\omega_0\tau_0\simeq 2\alpha\gamma\nu\simeq 10^{-8}\gamma$, which implies that classical radiation reaction will be substantial for electron energies of 10^2 TeV which is in the far quantum regime. So, unless we find a way of *classically* boosting the radiation reaction its observation will not become feasible. A possible means towards this end is nonlinearity.

3 Nonlinear Effects

Laser intensity is measured in terms of the r.m.s. energy gained by an electron traversing a laser wave length, in units of the electron rest energy. This leads to the dimensionless laser amplitude

$$a_0=\frac{eE_{\rm rms}\lambda\!\!\!^{-}}{mc^2}=\frac{eE_{\rm rms}}{mc\omega}\ , \tag{23}$$

which may be expressed covariantly using the energy density of (6) such that [14]

$$a_0^2=\frac{e^2\langle u_\mu T^{\mu\nu}u_\nu\rangle_{\rm rms}}{m^2c^2(k\cdot u)^2}\ . \tag{24}$$

When the laser beam is focussed down to the diffraction limit this may be turned into a rule-of-thumb estimate

of a_0 in terms of laser power P_L measured in petawatts (PW), namely

$$a_0^2 \simeq 5 \times 10^3 \, P_L/\mathrm{PW} \, . \tag{25}$$

For powers of 10 PW to be expected in the near future this implies a_0 values of a few hundred. For the sake of simplicity, however, we will restrict our interest to the nonlinear corrections of leading order in a_0.

It is known that an electron in a circularly polarised plane wave moves along a circle (in the average rest frame where there is no longitudinal drift, see [9], Ch. 48, Problem 3). The radiation spectrum for such a charge motion has been first calculated by Schott [15] [formula (128), Sect. VII.84; see also [2], Ch. 38] and consists of an infinite sum of higher harmonic contributions labelled by an integer n. Turning the nth harmonic intensity scattered per solid angle into a differential cross section yields [16]

$$\frac{d\sigma_n}{d\cos\theta} = \frac{4\pi n r_e^2}{a_0^2} \left(\cot^2\theta \, J_n^2(na_0 \sin\theta) + a_0^2 J_n'^2(na_0 \sin\theta) \right) \tag{26}$$

where n is the harmonic number and θ the scattering angle. To find the leading correction to linear Thomson scattering ($n = 1$, $a_0 = 0$) we expand the Bessel functions for $a_0 \ll 1$ using the first terms in their power series,

$$J_n(z) = (z/2)^n \left\{ \frac{1}{n!} - \frac{z^2/4}{(n+1)!} + O(z^4) \right\} \, . \tag{27}$$

Plugging this into (26) for $n = 1$ results in the differential cross section

$$\frac{d\sigma_1}{d\cos\theta} = r_e^2 \pi \left(1 + \cos^2\theta - \tfrac{1}{4} a_0^2 \sin^2\theta \, (3 + \cos^2\theta) \right) \, , \tag{28}$$

which nicely exhibits the correction to the Thomson cross section (13) of order a_0^2. Integrating over the angle θ we find the total cross section (for the fundamental harmonic, $n = 1$),

$$\sigma_1 = \sigma_{\mathrm{Th}} \left(1 - \tfrac{2}{5} a_0^2 \right) \, . \tag{29}$$

As $J_n^2(na_0 \sin\theta) \sim a_0^{2n}$ there is another a_0^2 correction coming from the second harmonic. Expanding for $n = 2$ one obtains

$$\frac{d\sigma_2}{d\cos\theta} = 2 \, r_e^2 \pi \, a_0^2 \sin^2\theta \left(1 + \cos^2\theta \right) \, . \tag{30}$$

Interestingly, this has the same overall $\sin^2\theta$ angular dependence as the a_0^2 correction in the fundamental cross section (28), and hence the two will be difficult to distinguish experimentally. This statement holds for circular polarisation, but for *linear* polarisation the situation is different and higher harmonics have been unambiguously identified from their angular radiation patterns [17].

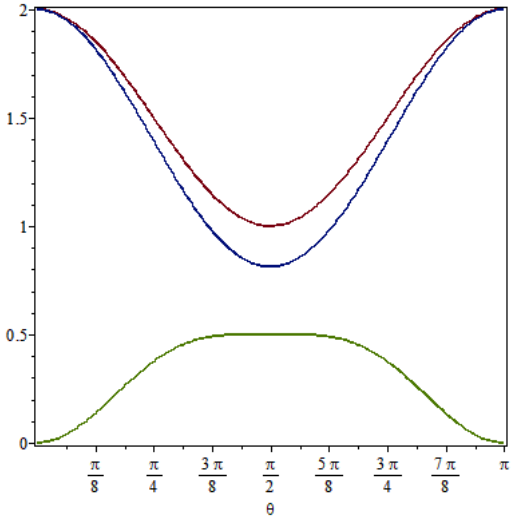

Fig. 1: Angular dependence of $d\sigma_{\mathrm{Th}}$ (upper curve), $d\sigma_1$ (middle curve) and $d\sigma_2$ (lower curve), for $a_0 = 0.5$, in units of $r_e^2\pi$, cf. (13), (28) and (30).

The angular dependence on θ of both cross sections, (28) and (30) are compared with the Thomson one (13) in Fig. 1. Note that only the Thomson term ($a_0 = 0$) contributes in forward and backward direction ($\theta = 0$ and $\theta = \pi$, respectively) as the a_0^2 corrections are suppressed there by the $\sin^2\theta$ factor.

Integrating (30) over θ results in a contribution of different sign

$$\sigma_2 = \tfrac{6}{5} \, a_0^2 \, \sigma_{\mathrm{Th}} \, . \tag{31}$$

As a consequence, upon adding (29) and (31), the complete order a_0^2 correction in the total cross section, i.e. in the sum

$$\sigma = \sigma_1 + \sigma_2 = \sigma_{\mathrm{Th}} \left(1 + \tfrac{4}{5} a_0^2 \right) \, , \tag{32}$$

becomes positive.

4 Quantum Effects

The quantum version of Thomson scattering is of course Compton scattering. Quantum corrections become important when the energy of the radiation becomes comparable to the electron rest mass. In this case, there will be substantial transfer of four-momentum and the whole scattering process is most naturally described using the photon picture, that is, by considering the process $e(p) + \gamma(k) \to e'(p') + \gamma'(k')$. Energy momentum conservation then reads $k + p = k' + p'$ and, in the technically simplest case with the electron initially at rest, implies the Compton formula for the scattered frequency,

$$\frac{\omega}{\omega'} = 1 + \nu_0 (1 - \cos\theta) \, , \tag{33}$$

with the invariant ν_0 defined in (21). In the classical limit, $\nu_0 \to 0$, the energy transfer (recoil) vanishes and $\omega = \omega'$. The differential cross section has first been

obtained by Klein and Nishina and reads [18]

$$\frac{d\sigma_{\rm KN}}{d\Omega} = \tfrac{1}{2} r_e^2 \left(\frac{\omega'}{\omega}\right)^2 \left(\frac{\omega}{\omega'} + \frac{\omega'}{\omega} - \sin^2\theta\right) . \qquad (34)$$

The classical Thomson limit (13) is readily obtained by setting $\omega = \omega'$. Integrating (34) over angles and expanding for $\nu_0 \ll 1$ we obtain the leading quantum correction to the Thomson cross section (4),

$$\sigma_{\rm KN} \simeq \sigma_{\rm Th}(1 - 2\nu_0) . \qquad (35)$$

5 Synthesis

Ideally, one would like to have a general theory that incorporates all corrections. In principle, such a theory exists (at least to some extent), namely quantum electrodynamics (QED) coupled to a strong external plane wave field, a particular incarnation of strong-field QED. It was originally developed in a series of papers, the most relevant ones being [19, 20, 21]. The main challenge for the present discussion is to go beyond the plane wave model and describe the external laser field, say by a Gaussian beam. In this case one loses the exact solution of the Dirac equation due to Volkov [22], and basically no progress has been made along this route. So one will have to make do with plane wave backgrounds for the time being.

Nevertheless, important achievements have been reported. For the case of circular polarisation, the most comprehensive collection of results can be found in [23] (see also Ch. 101 of [18]), in particular the strong field QED generalisation of the classical result 29 which usually is referred to as 'nonlinear Compton scattering' (NLC). We will not repeat the lengthy formulae here, but only present our result for the expansion of the fundamental cross section σ_1 which reads,

$$\sigma_{\rm NLC,1} = \sigma_{\rm Th}\left(1 - 2\nu_0 - \tfrac{2}{5}a_0^2 + \tfrac{14}{5}\nu_0 a_0^2 + \ldots\right) . \qquad (36)$$

Comparing with (29) we find the same nonlinear correction of order a_0^2 *plus* the quantum correction $2\nu_0$ from (35). This provides a useful consistency check. We also note that higher order corrections mix nonlinear and quantum contributions such as the last term of order $\nu_0 a_0^2$ in (36). In this rather literal sense, the NLC result (36) may be viewed as a unification of quantum and nonlinear corrections to Thomson scattering. What seems to be missing in this unification are the radiation reaction contributions. How these can be incorporated or, in other words, how they can be derived from strong field QED is largely unknown. The discussion above suggests, however, that the full theory may contain mixed terms of the form $(\alpha\nu_0 a_0)^{2n}$ implying the possibility of a regime ($a_0 \gg 1$) where quantum effects are still moderate but radiation reaction gets boosted due to large nonlinearities.

References

[1] F. Rohrlich, *Classical Charged Particles*, 3rd ed., World Scientific, Singapore, 2007.

[2] J. Schwinger, L.L. DeRaad, Jr., K.A. Milton and W.-y. Tsai, *Classical Electrodynamics*, Westview Press, Boulder (CO), 1998.

[3] J.J. Thomson, Phil. Mag., Ser. 6, **6**, 673 (1903).

[4] L.W. Davis, Phys. Rev. A **19**, 1177 (1979).

[5] H.A. Lorentz, *The Theory of Electrons*, B.G. Teubner, Leipzig, 1906; reprinted by Dover Publications, New York, 1952 and Cosimo, New York, 2007.

[6] M. Abraham, *Theorie der Elektrizität*, Teubner, Leipzig, 1905.

[7] P.A.M. Dirac, Proc. Roy. Soc. A **167**, 148-169 (1938).

[8] S. Coleman, in: *Electromagnetism: Paths to Research*, Vol. I, Ch. 6, ed. D. Teplitz, Plenum, New York, 1982.

[9] L. D. Landau and E. M. Lifshitz, *The Classical Theory of Fields (Course of Theoretical Physics, Vol. 2)*, Butterworth-Heinemann, Oxford, 1987.

[10] H. Spohn, Europhys. Lett. **49**, 287 (2000)

[11] S. E. Gralla, A. I. Harte and R. M. Wald, Phys. Rev. D **80**, 024031 (2009)

[12] C. Harvey, T. Heinzl, N. Iji and K. Langfeld, Phys. Rev. D **83**, 076013 (2011)

[13] C. Harvey, T. Heinzl and M. Marklund, Phys. Rev. D **84**, 116005 (2011)

[14] T. Heinzl and A. Ilderton, Opt. Commun. **282**, 1879 (2009)

[15] G.A. Schott, *Electromagnetic Radiation*, Cambridge University Press, 1912.

[16] K.T. McDonald, *Proposal for experimental studies of nonlinear quantum electrodynamics*, Princeton preprint DOE-ER-3072-38 (unpublished).

[17] S.-y. Chen, A. Maksimchuk and D. Umstadter, Nature **396**, 653 (1998).

[18] V. Berestetskii, E. Lifshitz and L Pitaevskii, *Quantum Electrodynamics*, Butterworth-Heinemann, Oxford, 1982.

[19] J.S. Toll, *The Dispersion Relation for Light and its Application to Problems Involving Electron Pairs*, PhD thesis, Princeton, 1952 (unpublished).

[20] H. Reiss, J. Math. Phys. **3** (1962) 59.

[21] A. I. Nikishov and V. I. Ritus, Zh. Eksp. Teor. Fiz. **46** , 776 (1963); Zh. Eksp. Teor. Fiz. **46**, 1768 (1964).

[22] D.M. Volkov, Z. Phys. **94**, 250 (1935).

[23] N. B. Narozhnyi and A.I. Nikishov and V.I. Ritus, Zh. Eksp. Teor. Fiz. **47**, 930 (1964).

The study of beam-plasma instabilities relevant to Laser-Plasma interactions in Fast Ignition

Contact *K.Humphrey@strath.ac.uk*

Kathryn Humphrey
SUPA, Department of Physics, University of Strathclyde, Glasgow, G4 0NG, UK
David Speirs
SUPA, Department of Physics, University of Strathclyde, Glasgow, G4 0NG, UK
Raoul Trines
STFC Rutherford Appleton Laboratory, Chilton, Didcot, Oxfordshire, OX11 0QX, UK
Nathan Sircombe
AWE plc. Aldermaston, Reading, Berkshire, RG7 4PR, UK
Peter Norreys
STFC Rutherford Appleton Laboratory, Chilton, Didcot, Oxfordshire, OX11 0QX, UK
Luís Silva
GoLP/Centro de Física dos Plasmas, Instituto Superior Técnico, 1049-001 Lisboa, Portugal
Robert Bingham
STFC Rutherford Appleton Laboratory, Chilton, Didcot, Oxfordshire, OX11 0QX, UK
SUPA, Department of Physics, University of Strathclyde, Glasgow, G4 0NG, UK

QED-PIC Codes for 10PW Laser-Plasma Simulation

Contact *c.ridgers1@physics.ox.ac.uk*

C.P. Ridgers

University of Oxford
Clarendon Laboratory, Oxford, OX1 3PU

C.S. Brady

University of Warwick
Centre for Fusion, Space and Astrophysics,
University of Warwick, Coventry CV4 7AL

T.D. Arber

University of Warwick
Centre for Fusion, Space and Astrophysics
University of Warwick, Coventry CV4 7AL

A.R. Bell

University of Oxford
Clarendon Laboratory, Oxford, OX1 3PU

Introduction

With construction beginning soon on several next-generation 10PW lasers as part of the European Union's Extreme Light Infrastructure (ELI) project, an exciting new frontier will soon be reached in high-power laser-plasma physics. 10PW lasers will create strong enough electromagnetic fields to access non-linear quantum electrodynamics (QED) processes [1]. In contrast to other scenarios where such effects are typically seen, the fields in a 10PW laser's focus will directly access non-linear QED processes and create a completely novel state of matter, a QED-plasma. Here the microscopic QED processes are inherently entwined with the full complexity of a macroscopic laser-plasma interaction and neither may be considered in isolation [2]. As a result the QED strongly modifies the basic plasma kinetics, with radiation reaction completely altering the equation of motion of the electrons and photon & pair production and annihilation giving rise to new sources and sinks of particles. Therefore the standard particle-in-cell (PIC) simulation approach, which has been the dominant kinetic simulation tool in plasma physics for 50 years, is inadequate for describing QED-plasmas a new approach (QED-PIC) must be adopted [2-4].

The inclusion of QED emission processes in a PIC code is considerably simplified by two approximations which may be made about the laser fields. 1. *Quasi-Static* – the ratio of the interaction time to the laser period is equal to the strength parameter $a = eE_L/m_e c\omega_L$ (E_L is the laser's electric field, ω_L its frequency). For $a > 100$ the laser field varies by 1% as the photon or pair is formed and the field may be treated as constant during the emission process. 2. *Weak* – the laser field is much less than the Schwinger limit for vacuum breakdown $E_s = 2\pi m_e c^2/e\lambda_c$ (λ_c is the Compton wavelength). We assume that $E_L < 0.01 E_s$ is sufficient for this condition to be satisfied. If the fields are quasi-static then the emission is correctly described by solving the appropriate rate equations in constant fields. If the fields are weak then one only need include the following first-order emission processes in the usual perturbative-QED treatment [1]: *Synchrotron radiation* – electrons and positrons in the plasma emit gamma-ray photons when accelerated by the laser's electromagnetic fields; *Pair production* – these photons go on to produce electron-positron pairs in the laser's fields. One can see that these are indeed first order QED processes from their Feynman diagrams, shown in figure 1.

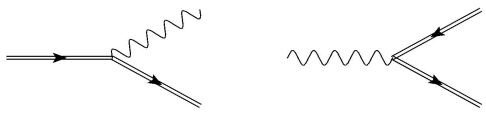

Figure 1: Feynman diagrams for synchrotron photon emission (left) and Breit-Wheeler pair production (right). Double lines refer to electrons in the strong-field, quasi-static limit.

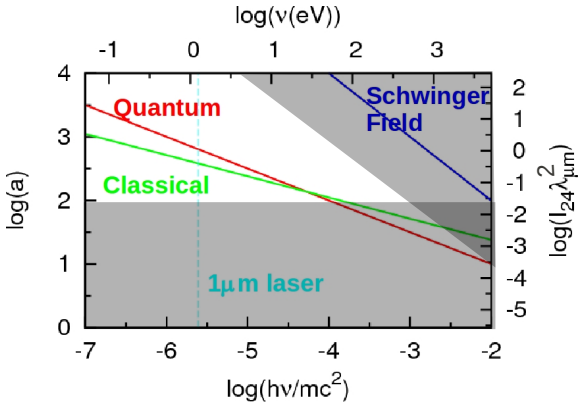

Figure 2: domain of validity for the QED-PIC code.

Figure 2 demonstrates the domain of parameter space where these two approximations (weak-field & quasi-static) hold; the quasi-static approximation breaks down in the lower shaded region, the weak-field in the upper shaded region. The region of validity is parameterised in terms of the photon energy of the laser $h\nu$ and the strength parameter of the laser-wave a (also written in terms of $I_{24}\lambda_{\mu m}^2$ where I_{24} is the laser intensity normalised to 10^{24}Wcm^{-2} and $\lambda_{\mu m}$ is the wavelength in microns). The green line marked 'classical' shows the region above which classical radiation reaction becomes important and that marked 'quantum' where the quantum nature of the emission processes becomes apparent. The cyan dashed line marked '1μm laser' is the photon energy for a one micron optical laser, increasing laser intensity corresponds to moving up this line in the vertical direction. The key point to note from figure 2 is that the QED-PIC model we propose is valid in the most interesting region of parameter space for optical lasers. This region lies above the green line, where the standard PIC approach breaks down. Above this line radiation of gamma-ray photons (the left-hand diagram in figure 1) is a significant energy sink for the electrons in the plasma, and the resulting radiation reaction must be included in the model. It is also clear that the region where this may be treated classically is a relatively narrow sliver and a quantum treatment is preferable. This is reinforced by the fact that as the quantum region is entered pair production (the right-hand diagram in figure 1 for which there is no classical analogue) becomes important

Clearly a PIC code is amenable to the inclusion of point-like particle emission events like those described above. The method by which this is done is described in detail elsewhere [2]. Broadly the algorithm consists of three steps:

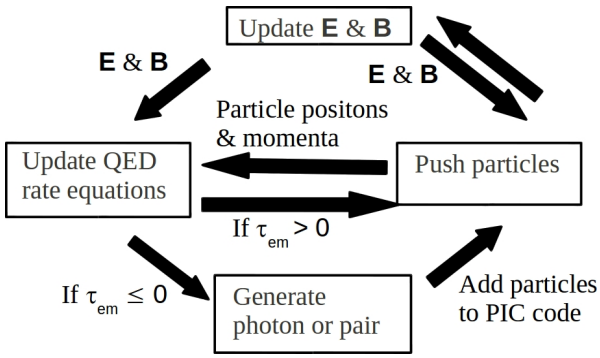

Figure 3: A schematic of the QED-PIC algorithm.

1. Assign optical depth for emission. The cumulative distribution of the optical depth at which the particle emits (τ_{em}) is $P=1-e^{-\tau_{em}}$. The emission is simulated by a Monte-Carlo algorithm whereby P is chosen at random.

2. Reduce the optical depth by solving the rate equation. τ_{em} is reduced by $(dN/dt)\Delta t$ where dN/dt is the rate equation for photon or pair production as given in [5]. Under the quasi-static approximation the rates depend only on the local electromagnetic fields and the particles momentum. These are passed from the PIC code.

3. When $\tau_{em}=0$ the emission event occurs. The energy of the emitted particles then needs to be assigned. The cumulative probability P of a particle having a given energy is tabulated. P is then assigned at random by the Monte-Carlo algorithm and the equation for P (as given in [3]) inverted to yield the energy. The emitting particle suffers the appropriate recoil – this is the radiation reaction force.

4. Add the emitted particles to the PIC code. Pairs then contribute self-consistently to the charge and current densities in the plasma.

A schematic of the QED-PIC algorithm is given in figure 3.

Testing the Algorithm

A good test problem for a QED-PIC code is the generation of gamma-ray photons and pairs in a constant magnetic field. The utility of this test problem lies in our ability to analytically treat the full range of parameters from classical emission to strongly quantum emission. The following semi-classical equation of motion may be derived for an electron moving in a strong magnetic field [5].

$$\frac{d\gamma}{dt}=\frac{-P(\gamma)}{m_e c^2} \qquad (1)$$

$P(\gamma)$ is the power radiated to synchrotron radiation by an electron of Lorentz factor γ . Note that this power is reduced by a factor $g(\gamma)$ relative to the classical synchrotron power, where $g(\gamma)$ is the Gaunt factor [5]. In the fully quantum mechanical treatment the emission is stochastic. However, if we simulate many particles, their average γ at a given time should agree with the semi-classical result in equation (1).

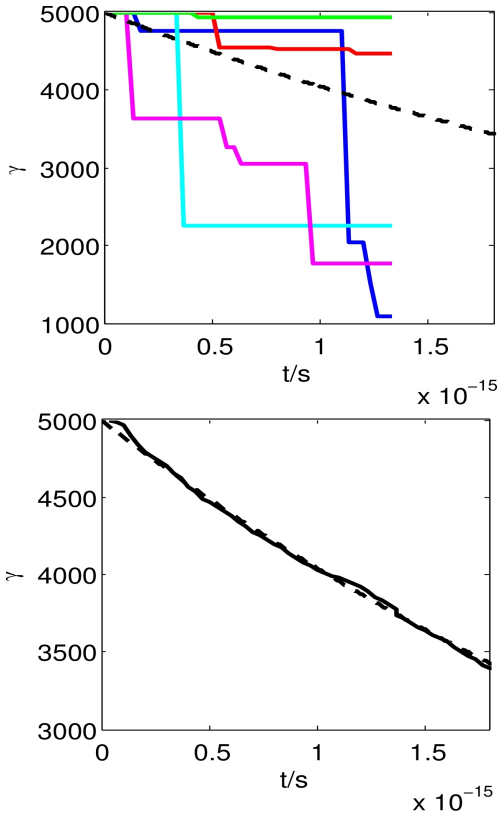

Figure 4: Change in energy with time of electrons in a constant magnetic field. Top: individual trajectories (coloured lines) compared to the semi-classical result from equation (1) (dashed line). Bottom: average over 1000 electron trajectories (solid line) & the semi-classical solution (dashed line).

Figure 4 shows the comparison between EPOCH simulations of electrons in a constant magnetic field and the solution of the semi-classical equation of motion given in equation (1). The top plot shows that the individual electron trajectories from EPOCH (coloured lines) are very different from the semi-classical solution (dashed line), with the stochastic nature of the emission process being very apparent. However, the bottom plot shows that when the average is taken over a large number of electrons (1000 in this case) the average rate of change of energy agrees with the semi-classical result.

Conclusions

Including QED reactions in plasma simulations will be essential as laser powers surpass 10PW in the near future. To do this a new simulation technique is required. We have outlined such a technique – the QED-PIC code – and outlined a test problem. We predict that the development of QED-PIC codes will be essential for the future of high-intensity laser plasma research.

Acknowledgements

This work was funded by EPSRC, grant number EP/G055165/1.

References

1. V.I. Ritus, J. Russ. Laser Res. **6**, 497 (1985)
2. C.P. Ridgers *et al*, Phys. Rev. Lett. **108**, 165006 (2012)
3. R. Duclous, J.G.Kirk & A.R. Bell, Plasma Phys. Controlled Fusion **53**, 015009 (2011)
4. E.N. Nerush *et al*, Phys. Rev. Lett. **106**, 035001 (2011)
5. J.G. Kirk, A.R. Bell & I. Arka, Plasma Phys. Controlled Fusion **51**, 085008 (2009)

ZEPHYROS v.0.7 series

Contact *alex.robinson@stfc.ac.uk*

A.P.L.Robinson

2.64 R1, Central Laser Facility,
STFC Rutherford-Appleton Lab, Didcot, Oxon. OX11 0QX

Introduction

The ZEPHYROS code is a 3D particle hybrid code developed in the CLF by APLR for studying fast electron transport. The code was first developed back in 2008/2009 to support a QUB lead experiment to look at resistive guiding of fast electron beams [1], and was also used to support the follow-up experiment [2]. Since then, ZEPHYROS has been used to support other experiments and new theoretical work.

Recently we have carried out an "over-haul" of the code which includes : (i) a set of upgrades to meet User Support requirements, (ii) cleaning up the code, (iii) putting the code in a version control system and code repository, (iv) documentation of the code and production of a user manual. In this report we will give a brief overview of the code and its capabilities, how the code has evolved to meet user requirements (especially in the 2011-2012 period), and describe the additional support that is being provided for this code.

Basic Framework

ZEPHYROS is a 3D particle-based hybrid code for studying fast electron transport in dense plasmas. This type of hybrid code treats a small 'hot' or 'fast' population via a kinetic description and a much cooler background via a fluid description. The electric field is determined through use of Ohm's law, and the magnetic field is evolved by the induction equation, thus a reduced description of the EM field evolution is used. The hybrid approximation also assumes local current balance ($j_{fast} + j_{cold} = 0$). The fast electrons are essentially described by a kinetic equation with the using the EM fields as determined by the hybrid approximation. The `Vlasov' part of this kinetic equation is solved by the standard methods that are used in Particle-in-Cell codes. The collisional part of this kinetic equation, which considers the drag that a fast electron experiences due to collisions with the background electrons, and the angular scattering due to background ions, is treated using Monte-Carlo methods. The background can be treated as a full fluid, however in the 0.7 series of ZEPHYROS it is still static, and only experiences heating, ionization and change in resistivity. Heating of the background occurs both due to Ohmic heating and heating due to the aforementioned collisional drag. The laser-target interaction is not simulated as such, and fast electrons are injected (via `promotion from the background') via a chosen prescription

ZEPHYROS thus closely follows this hybrid method as developed by Davies (see [3] for example) and others.

ZEPHYROS for CLF Users

Fast electron transport continues to be a major interest of the CLF user community, and the CLF Plasma Physics Group is making ZEPHYROS available to user groups on request. In order to facilitate the use of ZEPHYROS outside of the PPG we have gone through a process of tidying up the code, putting it in the official CLF repository and version control system, and producing a user manual. We have also engaged with user groups at QUB and U.Strathclyde to provide upgrades and modifications to meet the needs of these user groups. The CLF PPG will continue to make considerable effort to provide code modifications to meet user needs.

Meeting User Requirements

The following are examples of how ZEPHYROS has been upgraded to meet the requirements of the CLF user community :

1. Import of externally generated resistivity curves : Included so that resistivity curves from DFT-QMD simulations could be imported to simulate fast electron transport through different allotropes of carbon [5].

2. Double sided fast electron injection : To support interpretation of CLF experiments by Prof.Riley's team at QUB.

3. New fast electron injection distributions : Included at the request of Prof. McKenna's team at U.Strathclyde to help interpret proton emission measurements taken on the Vulcan system [6,7].

4. Lee More Resistivity Model : Currently implemented a 'reduced' version. This should allow modeling of a wide range of materials (both element and density) with some reasonable treatment of the cold conductivity region. Implemented to help research at both QUB and U.Strathclyde.

5. Externally Imposed B-fields : Users can now specify the inclusion of an externally imposed B-field. This was included to help the development of new transport concepts [8] by Prof.Borghesi's team at QUB and their future experimental interpretation.

6. Arbitrary Material Arrangements: Users can feed files to ZEPHYROS to specify a fully arbitrary arrangement of Z, ion density and temperature. This has been used by APLR in recent FI studies [9].

3D Visualization Support

STFC's e-Science facility has provided help in terms of 3D visualization via the production of the clfVtkWriter code (available on SCARF). This code will convert ZEPHYROS output files into .vtk files which are readable by the VisIt 3D visualization software. Thus all ZEPHYROS output can be rendered in 3D plots through VisIt.

Python Based Support for ZEPHYROS

We are providing additional support for ZEPHYROS via Python scripts for post-processing and visualization. Often users only want to be able to see 2D slices of select ZEPHYROS output in the first instance, without having to manual transfer or process the bulky main output files. We are producing a suite of Python scripts called *Pytheros*. The currently released scripts will extract entire arrays of slices and automatically produce pseudocolor plots by calling gnuplot, thus leaving the user with an entire set of plots in ready-to-view PNG format at a keystroke. Future versions of the *Pytheros* suite will include auto-plotting scripts that will slice and extract in many different ways, and also ones that invoke the *matplotlib* library which should provide better plotting.

Resources on SCARF

The PPG maintains a good environment for use of ZEPHYROS in the CLF space on the SCARF cluster facility. Here we maintain up-to-date executable, the supporting Python scripts, manuals, and clfVtkWriter ready for user access in a single area.

Acknowledgements

APLR would like to thank e-Science for their help with ensuring SCARF is a suitable home for the use of ZEPHYROS. In particular he'd also like to thank Srikanth Nagelle for his work on clfVtkWriter, and Ian Bush for his suggestions on Python scripting.

References

1. S.Kar et al., *Phys. Rev. Lett.*, **102**, 055001 (2009)
2. B.Ramakrishna, *Phys.Rev.Lett.,* **105**, 135001 (2010)
3. J.R.Davies, *Phys.Rev.E*, **65**, 026407 (2002)
4. ZEPHYROS User Manual, CLF Code Repository (2012) (email : alex.robinson@stfc.ac.uk or obtain from /work/clf/zeph_public/manuals on SCARF)
5. P.McKenna et al., *Phys.Rev.Lett.*, **106**, 185004 (2011)
6. M.Coury et al., Submitted
7. D.MacLellan et al., In Preparation
8. X.H.Yang et al., *Phys.Plasmas*, **18**, 093102 (2011)
9. A.P.L.Robinson, M.H.Key, and M.Tabak, *Phys.Rev.Lett.*,

The spectral distribution and total kinetic energy of fast electrons generated in a relativistically intense, frequency doubled laser-solid interaction

R.H.H. Scott,[1, 2, a)] F. Perez,[3] E.L. Clarke,[4] J.R. Davies,[5] H.-P. Schlenvoigt,[3] J.J. Santos,[6] S. Hulin,[6] K.L. Lancaster,[1] S.D. Baton,[3] S.J. Rose,[2] and P.A. Norreys[1, 2]

[1)] *Central Laser Facility, STFC, Rutherford Appleton Laboratory, Harwell Oxford, Didcot, OX11 0QX, United Kingdom*

[2)] *Department of Physics, Blackett Laboratory, Imperial College London, Prince Consort Road, London, SW7 2AZ, United Kingdom*

[3)] *LULI, École Polytechnique, UMR 7605, CNRS/CEA/UPMC, Route de Saclay, 91128 Palaiseau, France*

[4)] *TEI, Chania, Crete, Greece*

[5)] *GoLP, Instituto de Plasmas e Fusão Nuclear - Laboratório Associado, Instituto Superior Técnico, 1049-001 Lisboa, Portugal*

[6)] *Univ. Bordeaux/CNRS/CEA, CELIA, UMR 5107, 33405 Talence, France*

(Dated: June 25, 2012)

Novel bremsstrahlung photon detectors have been successfully fielded on a relativistically-intense laser-solid experiment using frequency doubled laser light. Analysis of the experimental data was performed with the 3D Monte Carlo code MCNPX. The spectral distribution of the bremsstralung photon spectrum generated by the fast electron beam corresponds to a relativistic Maxwellian of temperature 125 ± 25 keV, this is best fit by Sherlock's scaling law. The measured laser to fast electron conversion efficiency was $13 \pm 3\%$ at an intensity of $5 \pm 3 \times 10^{18}$ W/cm^2. The design of the bremsstrahlung photon detector is described and the interpretation of the frequency doubled experimental data using Monte Carlo modelling is detailed.

I. INTRODUCTION

When an intense laser pulse irradiates a solid target, large numbers of fast electrons are generated. The kinetic energy these fast electrons acquire during the interaction is close to that of electrons oscillating in the transverse field of the incident light wave[1–3]. If the picosecond-duration laser pulse is associated with a much longer duration, lower intensity pedestal (caused by amplified spontaneous emission), then a coronal plasma is formed around the interaction point some time before the relativistic pulse arrives. In these circumstances, it is possible for the fast electrons to acquire substantially higher energies[4] via ponderomotive acceleration processes in the finite density gradient plasma.

The understanding of fast electron energy transport caused by intense laser-plasma interactions is an interesting area of fundamental physics. Furthermore the detailed characterization of the fast electron transport under controlled conditions is important for numerous applications including proton and ion beam production[5–8], isochoric heating of high density matter for opacity studies[9–13], and fast ignition inertial confinement fusion[14–19]. Fast electron energy transport is dictated by the resistivity and density of the medium in which the transport is occurring, the fraction of laser energy absorbed into fast electrons, the fast electron source size, their divergence and the energy spectrum. This paper describes a methodology by which the fast electron energy spectrum and total fast electron energy can be measured using bremsstrahlung radiation, these techniques are then used to analyze a frequency doubled, relativistically-intense laser-solid experiment.

The measurement of the fast electron energy spectrum is greatly complicated by the formation of a large electrostatic field at the target rear surface/vacuum boundary by the initial population of electrons exiting the target[20]. This field confines the subsequent fast electrons, meaning only a small fraction of the fast electrons accelerated by the laser are able to exit the target rear. The spectrum of the fast electrons which do exit the target can be measured relatively simply using magnetic spectrometers, however as the bulk of the electrons remain within the target, it is likely that the fast electron spectrum measured from this electron population is not representative of the bulk fast electron spectrum. Bremsstrahlung photon emission, caused by fast electron collisions with the target, offers a mechanism by which the spectrum and total laser absorption of the bulk fast electron population can be inferred.

This paper describes the application of bremsstrahlung measurement techniques and associated Monte Carlo analysis in combination with spectrally and spatially resolved Cu K_α measurements and rear surface pyrometry. A detailed quantitative analysis of the fast electron transport induced by frequency doubled, relativistically-intense laser-solid interactions is presented. Section II begins by discussing the bremsstrahlung generation mechanism and previously employed bremsstrahlung measure-

[a)] Electronic mail: Robbie.Scott@stfc.ac.uk; The authors gratefully thank the staff of the LULI2000 laser facility, Ecole Polytechnique, Paris, France. The author would also like to thank Stuart Ansel for useful MCNPX discussions. This investigation was undertaken as part of the HiPER preparatory project and was funded by LaserLab Europe, Ecole Polytechnique and by the Science and Technology Facilities Council.

ment techniques, while section III goes on to describe the design of a novel bremsstrahlung detector. Section IV describes how Monte Carlo modelling is used to back out the fast electron temperature and the total laser energy absorbed into fast electrons. Finally an experiment is described in section V using frequency doubled, relativistically-intense laser light to irradiate a solid target. The measured bremsstrahlung radiation energy deposition is compared with modelling allowing the experimental fast electron temperature and fraction of laser light absorbed into fast electrons to be inferred.

II. BACKGROUND

During relativistically intense laser-solid interactions large numbers of fast electrons are generated with energies up to and exceeding 100MeV. The fast electrons undergo collisions within the solid target, with the resulting deceleration causing the emission of bremsstrahlung photons. The energy of an emitted photon is dictated by the energy the fast electron loses during the deceleration, and is therefore related to both the angle through which the electron is scattered and the initial fast electron energy. The photon's emission direction is limited to a that of a cone, the major axis of which is that of the initial fast electron propagation direction, while the opening angle of the cone is determined by the initial Lorentz factor of the fast electron. The relationship between the incident electron and bremsstrahlung photon mean that absolutely calibrated measurements of the spatial and spectral distribution of the bremsstrahlung emission can enable the determination of the fast electron spectrum, laser absorption fraction and fast electron spatial distribution. Due to the number of particles involved, interpretation of experimental data rapidly becomes extremely complex meaning data analysis is greatly simplified by the use of Monte Carlo type simulations.

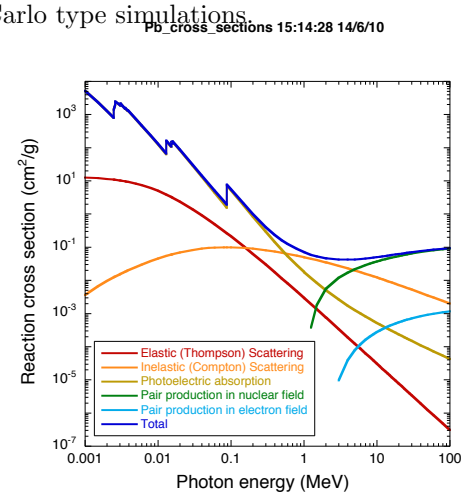

Figure 1. Reaction cross sections with respect to incident photon energy for Pb, source XCOM, NIST. Photonuclear interactions are not shown but are extremely small for Pb for photon energies < 10 MeV.

Bremsstrahlung radiation measurement techniques typically employ either differential filtering or photonuclear activation. Photonuclear techniques[21,22] are limited to photons of energies > 5 MeV due to the rapid decrease in the photonuclear cross section below this energy. For the purposes of fast ignition inertial confinement fusion, the electron energies of interest are those below ~ 3 MeV hence photonuclear techniques are less well suited to such measurements. Differential filtering[4,23–25] relies on spectral variations in opacity; away from resonance regions such as the K edges of materials, the opacity decreases monotonically with incident photon energy, typically followed by a slight increase above $\sim 1-5$ MeV (figure 1) due to the increasing photonuclear cross sections in this region. As photons propagate through matter, the flux reduces exponentially with increasing distance, while from figure 1 the cross section is generally inversely proportional to photon energy. Therefore as the photons propagate through a given material, the low energy flux undergoes more collisions (and ultimately absorption) than the high energy photon flux. By using many filters of differing thicknesses and measuring the flux exiting the filters, the spectrum of the incident flux can be inferred.

Photon flux is generally measured indirectly via photon energy deposition, various different techniques exist such as thermoluminescent detectors, image plates and pin diodes. The change in cross section with material can also potentially be used advantageously, for example in a Ross pair configuration the K-edges of various materials are used to preferentially remove photons with energies closely corresponding to that of the K-edge of the filter material. However this method is only effective for photon energies up to ∼100 keV, as although the K-edge energy increases with atomic number, even Uranium only has a K-edge of 115 keV.

Accurate interpretation of differential filtering is complicated as photon collisions lead to the emission of secondary particles through various mechanisms such as the photoelectric effect, pair production, or photonuclear interactions. These secondary particles may in turn emit their own secondaries, hence the situation rapidly becomes very complex. Monte Carlo modelling is well suited to this type of problem, allowing the measured signal to be deconvolved.

Bremsstrahlung detectors have been used in numerous guises on laser-solid experiments in the past[4,21–25]. Limitations of previous detectors have generally arisen from the relatively small number of energy bins and the inability to measure higher energy photons.

Norreys *et al*[23] used bremsstrahlung measurements to diagnose the hot electron temperature. These measurements were made using an array of pin diodes with photomultiplier/scintillator detectors in combination with substantial Pb collimation, shielding and 2-5 mm of differential Pb filtering. This setup enabled the measurement of the relationship $T_{hot} \sim (I\lambda^2)^{1/3}$.

$Li_2B_4O_7$ and $CaSO_4$ thermoluminescent detectors were used by Key *et al* to detect bremsstrahlung

emission[4].

More recently Chen *et al*[24] designed a bremsstrahlung detector based on differential filtering using 13 different materials which separated image plates. The materials were chosen so that their k-edges lay in an appropriate part of the spectrum thereby preferentially filtering photons of that energy. In combination with ITS modelling of the electron and photon transport, this techniques allows good resolution of the lower energy region of the spectrum. This method provides good spectral resolution in the spectral region examined, but has the practical disadvantage of the number of image plates which are required; extracting, scanning and replacing 13 image plates after each laser shot creates a huge experimental workload limiting the number of detectors which can be fielded on an experiment and hence the spatial resolution.

III. DESIGN OF A NOVEL BREMSSTRAHLUNG DETECTOR USING MCNPX

A new bremsstrahlung detector design was conceived in order to provide good energy resolution across the spectral region of interest, whilst allowing numerous detectors to be fielded on one experiment. The ability to field multiple detectors is important as it allows the angular emission of the bremsstrahlung emission to be measured. As the cone angle of the bremsstrahlung emission is related to the fast electron energy, the spatial resolution provides a secondary measurement with which to further constrain Monte Carlo calculations. This is important in order to ensure the solution which is arrived at via the Monte Carlo modelling is unique. From these measurements it is possible to infer the fast electron temperature as a function of angle, the absolute number of fast electrons and hence the fraction of laser energy absorbed into fast electrons, and potentially the fast electron divergence angle.

The filtering was chosen to be of differential design in order that the < 3 MeV photons of importance to fast ignition can be resolved. The filters were comprised of just one material with differing filter thicknesses as, based on the cross-sections, this should allow the resolution of higher energy photons. By creating a three dimensional filter array, a design solution was arrived at which only requires one image plate - a significant improvement over previous designs. The filter design is shown in figure 2. An image is created on the image plate by the transmitted photons, this image is a function of the bremsstrahlung spectrum, filter thickness, and filter material. This filtering concept requires that the bremsstrahlung flux is effectively spatially and spectrally uniform across the cavity of the detector. Modelling showed that this assumption is valid as long as the detector is sufficiently far from the electron source.

A detailed characterization of Pb and Fe as filtering materials was performed as they both have relatively high total cross sections, also the minimum inflection point of

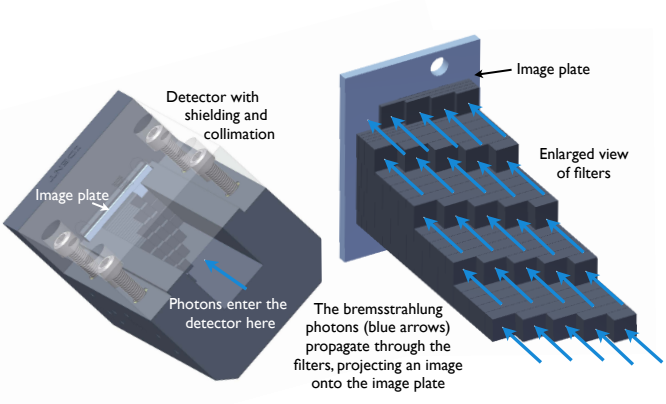

Figure 2. 3D CAD models: (left) the final detector design shown rotated by 45° as per the experimental orientation (one of the collimator walls is transparent for clarity). The view is through the 'mouth' of the detector and down the collimator towards the stepped filter array. The image plate is shown in light blue behind the filters. (Right) The photons propagate through the filter array, creating an image on the region of image plate behind the filters, this image contains convolved information about the spectral distribution of the bremsstrahlung photons. The 25 filters create 25 energy bins.

their cross sections is > 1 MeV which should allow for spectral resolution up to (and even beyond) this point. 3D MCNPX modelling was used to quantify the photon energy deposition within the active phosphor layer of the image plate as a function of both photon energy and filter thickness. A 3D filtering array was created spanning a wide filtering thickness range within MCNPX . In order to characterize photon energy deposition as a function of photon energy, numerous mono-energetic photon source runs were performed, yielding the energy deposition as a function of filter thickness for that particular photon energy. The data from many runs was aggregated to create figure 3.

The three dimensional filtering array was potentially susceptible to cross-talk between the various filters due to lateral Compton scattering within the filters as the photons propagate towards the image plate detector, excessive scattering could have rendered the design unusable. This cross-talk was reduced geometrically by minimizing the required filter depth by maximizing the total photon cross section of the filter material (within practical limitations) by using Pb filtering. The modelled energy deposition in the image plate is shown in figure 5, it can be seen that there is a reasonably clear distinction between the signals formed on each region corresponding to a channel of the detector.

Teflon was excluded as a structural material as it was found to massively reduce the sensitivity of the detector by flooding the image plate with low energy K_α photons effectively giving a huge background. Modelling showed high Z materials were far better in this respect, hence Pb was used structurally throughout.

Detailed design of the bremsstrahlung detector was

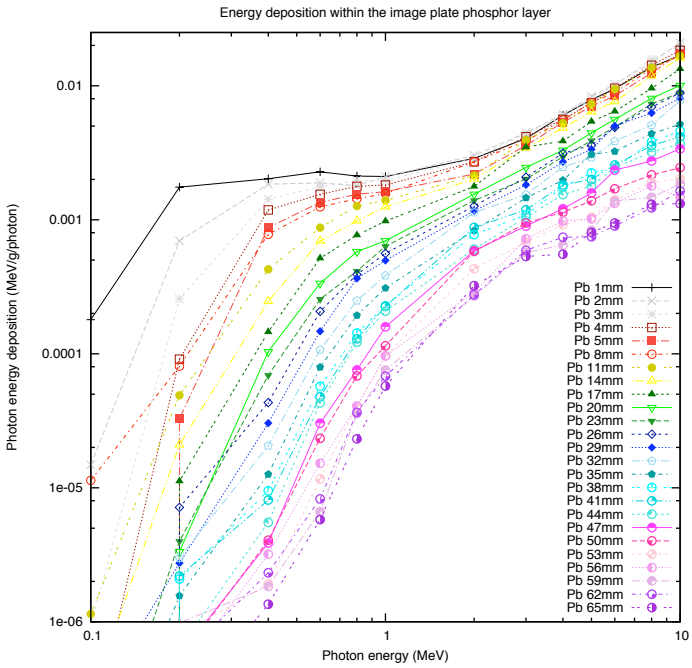

Figure 3. Energy deposition within the active phosphor layer of the image plate as a function of photon energy and Pb filter thickness, as modelled with MCNPX. Each line represents a different thickness of Pb filtering, the thicknesses shown are those which were eventually used on the final design. The relative errors are not shown for clarity, but it can be seen from the erratic nature of the curves that the relative error is higher when the photon energies are lowest and the filters thicker. Interestingly the curves rise monotonically despite the increase in the cross section of Pb at ~ 3 MeV, this implies that the detector should have sensitivity up to 10 MeV.

performed by using MCNPX[27] to solve the 3D coupled electron-photon transport problem. Excluding the effects of self-generated electro-magnetic fields, and using the assumption that the cold cross sections remain accurate at temperatures of ~ 50 eV, MCNPX can accurately model the electron transport and bremsstrahlung generation via collisions within the solid target, furthermore the subsequent photon flux propagation through the filters and energy deposition within the image plate can also be modelled as one self-consistent problem, whilst accounting for undesirable/complex effects such as K_α emission and pair production within the filters.

The solid laser target, detector and image plate were modelled in 3D in MCNPX, using accurate dimensions, material densities and cross sections. An electron source of appropriate spectral and spatial (both angular and position) distribution is injected into the target, generating bremsstrahlung photons, the spectral and spatial characteristics of which are related to those of the electron source. The photons propagate through space and then into the detector. Within the detector they pass through many centimeters of high Z filtering before depositing their energy within the ~ 10 µm phosphor layer of the image plate. However as the probability of such an event occurring is extremely small, the problem is computationally intractable in its raw form, especially given the many design iterations. During the conceptual design huge computational gains were made by sub-dividing the problem and using variance, or relative error, reduction techniques[27]. An example of a design run is shown in figure 6, in this case the target has been moved artificially close to the detector to improve statistics. Figure 4 shows the flux distribution within the filters in more detail.

From figure 3 it can be seen that the data for the lowest photon energies has significantly higher relative errors (although these are not explicitly plotted for clarity), this is visible in the more erratic nature of the curves towards the bottom left of the graph. All but the thinnest filters prevent all of the 100 keV photons from propagating through the filters, meaning there is *no* energy deposition for 100 keV photons with thicker filters. Examination of the trends of the curves and physical intuition suggest this result is incorrect. In reality some of the 100 keV photons would have propagated through the filtering depositing their energy within the phosphor, however the computational limitations on the number of particles that can be simulated means that such an improbable event may not be sampled, and even if it is (as in the case of the thinner filters), it may be sampled so few times that the relative error is large. To make the problem tractable a new photon population control technique was devised. In the new scheme, the 5 dimensions of phase space (3 space, energy, and time) are subdivided with an 'importance' n applied to each region. As photons propagate through the filters (and hence phase space) their population will reduce exponentially and be shifted to lower energies. Simultaneously the pre-set importances will cause the photons to be split into n photons of weight $1/n$. In this way a large number of low weight, low energy photons can be tracked through the Pb, ultimately depositing some energy in the image plate. Even though the energy deposited per tracked particle is low, the statistics are good as many particles deposit an appropriate amount of energy. The population control technique enabled a highly optimized solution to this specific transport problem to be implemented that was otherwise intractable.

The detector Pb wall thickness was designed such that the K_α radiation produced within the walls of the experimental chamber would be reduced by $\sim 10^{-10}$. The collimator length was minimized in order to save space, its length was based on MCNPX modelling which showed that even 100 MeV photons should not be able to propagate through 20 cm of Pb.

A 0.4 T magnet was positioned between the laser target and the bremsstrahlung detector to bend those electrons which do escape the target away from the mouth of the detector. This field will deflect 100 MeV electrons away from the detector entrance if the magnet is located 40 cm in front of the detector.

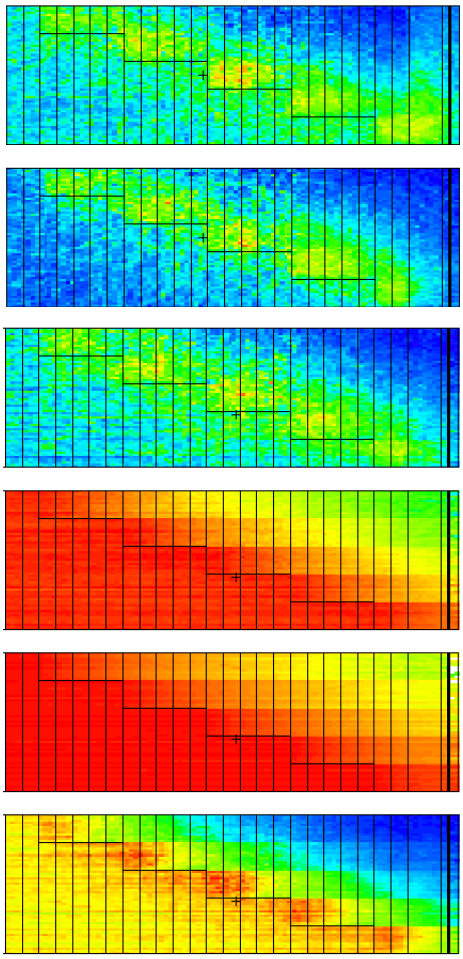

Figure 4. Flux within one planar slice through the filters during a simplified run where a photon source of uniform photon energy probability up to 100 MeV with zero divergence was injected just before the entrance to the filters. Photons enter from the left into a vacuum, the Pb filters are the stepped structure in the the top right of each image. From top to bottom: photon flux 1 keV to 500 keV, 500 keV to 600 keV, 600 keV to 1 MeV, 1 -10 MeV, 10-100 MeV, 1 keV to 100 MeV (all photons in problem). From these images various effects are apparent; firstly the low energy photon flux *increases* within the filters. This somewhat counterintuitive result is due to K_α creation and pair production by the higher energy photons. Secondly the higher energy photons are far less susceptible to scattering and hence will deposit energy within the correct spatial region of the image plate more effectively than lower energy photons. The plot showing the contribution of all the photons gives confidence that the filtering structures are effectively projected onto the image plate by the photons.

IV. FAST ELECTRON TEMPERATURE, ABSORPTION AND DIVERGENCE MODELLING

The experimental setup was modelled in 3D within MCNPX including all of the target layer materials, n bremsstrahlung detectors are positioned exactly as per the experiment both in terms of angle and distance from the source. A probabilistic distribution of the source electron energies was created, corresponding to a 1D relativistic Maxwellian. In order to make the problem computationally tractable, it is subdivided, the modelling steps are as follows:

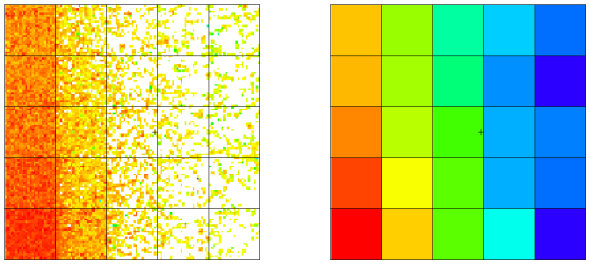

Figure 5. Energy deposition within the active phosphor layer of the image plate by all photons, as modelled with MCNPX. The filter thickness increases monotonically going from bottom to top in each column, the filters in the columns to the left are thinner than those on the right. (Left) high resolution image of energy deposition. (Right) low resolution energy deposition; area integral of energy deposition over pixel size. The filter structure is visible in both the high and low resolution images. In this case the electron source temperature is relatively low with a temperature of 100 keV, hence the thickest filters are not of use - the energy deposition is relatively uniform over the region of the thickest filters.

1. Using a single detector a range of Maxwellian fast electron sources with temperatures varying from 0.1 MeV to 0.8 MeV were 'injected' into the target in MCNPX (the temperature range was based on the experimental intensity and using Beg's[23] and Wilks'[33] scalings). The modelled photon energy deposition within the phosphor layer of the image plate was compared to the experimentally measured PSL value using absolute calibration values from the image plates[?] . The modelled result which best fit the experimental data was deemed to be the correct relativistic Maxwellian temperature.

2. Using the fast electron spectrum found to best fit the data (step 1) and an assumed fast electron angular divergence, a run is performed using n detectors. The spectrum of bremsstrahlung photons entering each detector is recorded.

3. n new input decks are created, one for each detector. Each deck uses the bremsstrahlung spectrum (from step 2) to define the spectrum of the photons injected in this run. This calculates the coupled photon-electron transport through n detectors, their filters and ultimately the energy deposited within the phosphor layer of the image

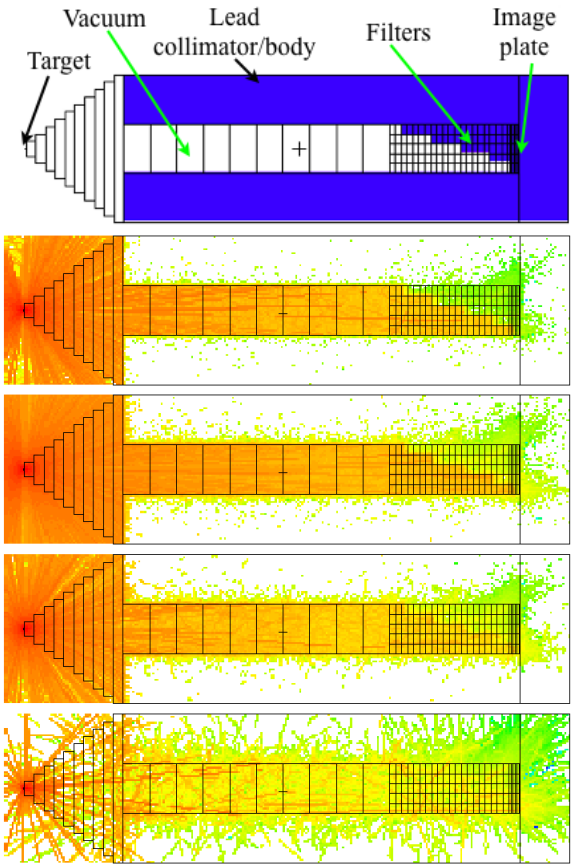

Figure 6. Top: Schematic diagram of the detector. Note that the cells within the vacuum (cell walls are depicted by the black lines) are not part of the detector geometry but were used for variance reduction population control techniques. Lower four images: Measurements of the bremsstrahlung photon flux within the detector using a 0.5 MeV non-relativistic Maxwellian electron source with the target placed artificially close to the detector - electrons are injected into the target from the left. Red indicates more flux, green less. The various images show photons of differing energies. From second top to bottom: 1 to 10 keV, 10 to 100 keV, 100 to 300 keV, 300 keV to 1 MeV. From these images it can be seen that even the lowest energy photons are able to propagate through the thick Pb filtering, although this will in part be due to the creation of low energy photons by the more penetrating high energy photons. To the left of the target it is apparent that more of the lower energy photons are scattered backwards out of the target than propagate towards the detector. There is a lower probability of a higher energy photon being created due to the relativistic Maxwellian electron energy distribution. The lower population of the highest energy photons is clearly visible in the bottom image, as is their greater ability to penetrate further through the Pb walls of the detector.

plate per bremsstrahlung photon entering the detector.

4. Using the absolute calibration of the image plates the modelled energy deposition within the phosphor layer of the image plate is compared with the experimentally measured values. Depending on the result of this comparison either the electron source spectrum and/or divergence may be iterated until a good match is found.

5. The total energy in the fast electron distribution is calculated as follows:

   (a) The modelled bremsstrahlung spectrum entering each of the detectors is integrated the over each detector cavity and energy spectrum, giving the total number of photons entering each detector *per source electron* entering the target.

   (b) The total modelled energy deposited in the image plate phosphor layer *per source photon* is found by integrating over the phosphor volume. Using (a) this is then converted to total energy deposited in the phosphor layer *per source electron*.

   (c) Using the image plate absolute calibration, the total experimentally measured energy deposition in units of PSL are converted to units of MeV.

   (d) From (b) and (c) the number of source electrons required to create the experimentally measured signal are calculated.

   (e) The mean electron energy of the fast electron distribution is calculated given its temperature and distribution. The total energy of the fast electron distribution is found by multiplying the number of electrons from (d) by the mean energy of the fast electron distribution.

When using the above absorption calculation technique it is crucial that the modelled response of all the detectors matches that of the experimental data, as a consequence some fast electron divergence (or potentially angularly varying fast electron temperature) of the electron source must be assumed. Conversely, the value of fast electron divergence which best fits the data is a measure of the experimental fast electron divergence. This measurement of divergence contains spectral information but is very limited in spatial resolution compared to existing techniques due to the number of detectors. Sensitivity to the assumed divergence angle will only occur when the fast electron temperature is sufficiently high such that the bremsstrahlung is confined to the $1/\gamma$ angular cone. Bremsstrahlung theory leads us to expect anisotropic distributions from higher fast electron temperatures and hence should occur during experiments with higher values of $I\lambda^2$.

V. FREQUENCY DOUBLED, RELATIVISTICALLY-INTENSE, LASER-SOLID EXPERIMENT

An experiment was performed at the LULI 2000 laser facility at the Ecole Polytechnique in Paris in order to characterize the properties of the fast electron

beam generated when relativistically-intense frequency-doubled laser light interacts with a solid target. We show that using a combination of absolutely calibrated bremsstrahlung measurements, spatially resolved Cu K_α emission from a fluor layer within the target and target rear thermal emission, it is possible to diagnose all of the fast electron beam properties which are important for fast ignition inertial confinement fusion in just a few laser shots. On this experiment 25J of 527 nm light was incident on the target at 45 degree p-polarization, with a pulse length of 800 fs and spatial full-width-at-half-maximum of 15 µm yielding a peak intensity of 9×10^{18} W/cm^2 and mean intensity (spatially and temporally averaging) of 5×10^{18} W/cm^2.

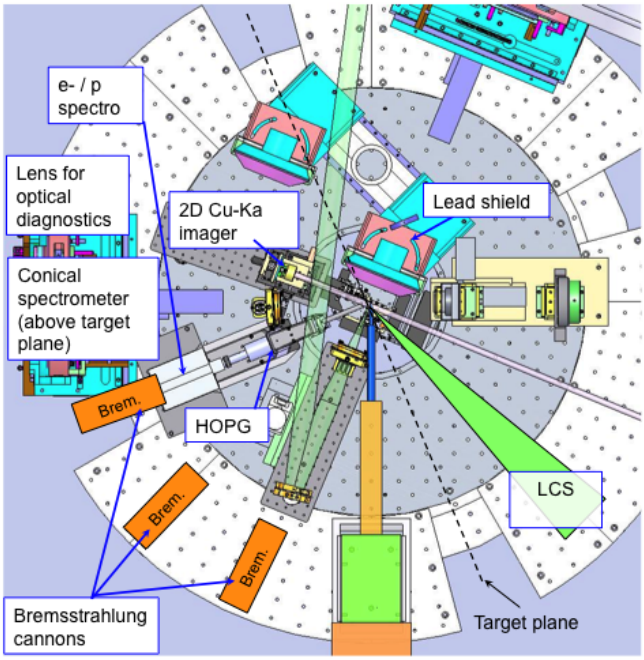

Figure 7. The experimental setup used for the $2\omega_0$ experiment.

A. Experimental Setup

The setup is depicted in figure 7. The target rear surface temperatures were evaluated using Cu K_α x-ray spectroscopy, and spatially and temporally resolved streaked pyrometry of the rear surface. A KAP conical crystal with a focal length of 310 mm and 2d spacing of 26.64 Å focussed the 6.85-8.5 keV (fifth order) Cu K_{α_1} and K_{α_2} x-rays onto an image plate. The temperatures were derived by line fitting the experimental spectra against spectra synthetically generated using the nlte atomic kinetics code FLYCHK[30]. F/4 optics at 20° from target normal collected the visible optical emission from the target rear surface, which was focussed onto a high speed pyrometric sampling camera[28]. In this setup the pyrometry combines a 2D spatial resolution of 70 µm with a temporal resolution of ∼ 15 ps and multi-frame capability over the 1 ns window. The pyrometry was filtered with a bandpass filter centred at 460 nm with a 40 nm FWHM, this maintained sufficient thermal signal, removed any optical transition radiation and provided good temporal resolution by minimizing dispersion within the fibre-optics. The temporally and spatially resolved target rear surface thermal emission data was calibrated using an absolutely calibrated lamp which provided a reference intensity at a known temperature for both optical diagnostics. A detailed procedure for backing out the target temperature is described in[29] and[?] .

The Cu K_α x-rays emitted from the Cu layer of the target were imaged with a spherically bent quartz 2131 crystal (2d = 3.082 Å) with the radius of curvature RC = 380 mm. This crystal only reflects the K_{α_1} line at 8048 eV, and has a central Bragg angle of $\theta_0 = 87.3 \pm 0.1°$. The setup gave a magnification of 11. The aperture diameter size on the crystal was 15 mm at the beginning of the experiment, but was changed to 25 mm to get more signal, cross calibration was used to compare the data before and after this alteration.

The bremsstrahlung spectra and spatial distribution were measured using three detectors as shown in figure 7. Based on the work of Santala *et al*[31] it was anticipated that the peak emission should be located along the target normal direction given the high experimental contrast, hence they were positioned along the laser axis and then at two 22.5° increments with the third detector at target normal. Magnets were positioned such that all electrons below 40 MeV were prevented from entering the detectors.

A variety of ∼ 5mm square, planar targets were used for the experiment. For the purposes of the absolute laser absorption measurements the target was constructed as follows Al (10 µm), Ag (10 µm), Au (10 µm), Cu (10 µm), Cu (10 µm) and CH (300 µm), with the laser incident on the first Al layer. Absolute bremsstrahlung radiation measurements require the prevention of refluxing as multiple transits of the electrons within the target will cause multiple bremsstrahlung emissions from within the target. By attaching a 300 µm mylar layer to the target rear, the majority of the fast electrons are stopped within 600 µm of plastic (based on Monte Carlo modelling of an appropriate fast electron energy distribution), meaning the experimental signal should be a good approximation to a single pass of the fast electrons passing through the high Z material. For the rear surface pyrometry measurements either planar pure Al targets or Al backed with Cu were used.

B. Results

1. Target Rear Surface Temperatures

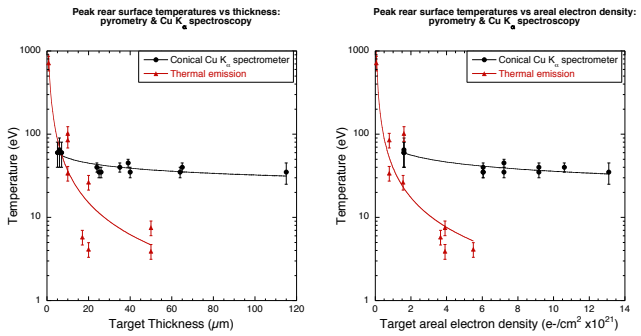

(a) (b)

Figure 8. Rear surface temperatures measured by thermal emission and Cu K_α spectroscopy as a function of (a) target thickness, and (b) areal electron density. All temperature data has been normalised to a shot energy of 25 J (the mean experimental laser energy).

The temperatures measured by rear surface pyrometry and Cu K_α spectroscopy are shown in figure 8. For the pyrometrically derived data, the plot against areal electron density exhibits a more predictable trend than that against target thickness, this is due to the variation in the target composition for the various aspects of the experiment. The temperatures derived from the Cu K_α spectroscopy show little variation with thickness in comparison to the pyrometric data. This is attributed to a relative insensitivity in the Cu K_α spectroscopy (over this experimental range) as evidenced by the fact that over the areal density range of the Cu K_α spectroscopy measurements, simple heat capacity arguments show that even a collimated beam should heat the target a factor of seven less, while the experimental spectroscopy results only reduce by of factor 1.5. This insensitivity has been found to be consistently true over a number of experiments and is attributed to a number of effects: firstly the Cu K_α spectroscopy is spatially and temporally averaged, secondly the theoretical Cu K_α lines (from FLYCHK do not vary a lot over the (pyrometrically inferred) experimental temperature range. These factors in combination with experimental noise mean the sensitivity is lower than the pyrometry. It should be noted that when such effects are minimised, Cu K_α spectroscopy is a very useful technique for making absolute temperature measurements.

2. Fast Electron Energy Spectrum

The procedure to find the fast electron energy spectrum (as outlined in section IV) was followed using the experimental target materials, densities, geometry and detector geometry modelled in 3D within MCNPX. Figure 9 (a) and (b) show the relative energy deposition within the different spatial regions of the image plate (each region corresponds to an energy bin) as a function of fast electron temperature. The experimentally measured values are also over-plotted. The best fit to the experimental data was a fast electron temperature of 125 ± 25 keV. For the purpose of evaluating the fast electron temperature only the relative values of the energy deposition in each bin is important, hence arbitrary units are employed here.

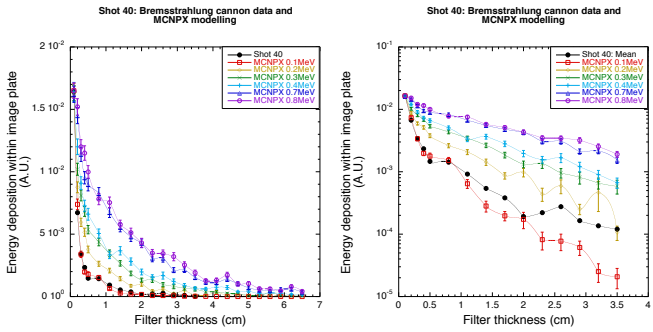

(a) (b)

Figure 9. (a) & (b) show the same data plotted on linear and log scales. The data from shot 40 (detector at target normal) is compared to the modelled detector response for various initial relativistic Maxwellian electron temperatures. The experimental data is the mean PSL value within each 'region' of the image plate, a region exactly corresponds to the shadow cast by one of the filters onto the image plate, likewise the MCNPX value is the mean energy deposition within the same location and area of the modelled image plate's phosphor layer.

3. Fast Electron Divergence

Figure 10 shows a plot of the HWHM of the thermal and Cu K_α emission regions as a function of target thickness or Cu layer depth respectively. The two datasets show similar results. The half angle divergence calculated from the thermal HWHM data from targets of thickness > 10 µm is $\sim 14°$, while that from the imager is $21 \pm 2°$. The 0.8 µm target thermal emission region is significantly enlarged, this is attributed to refluxing within this thin target. The and Cu K_α imager dataset is comprised of data from targets both with and without anti-refluxing 300 µm layers. The generally linear increase in HWHM with thickness indicates that even for the 10 µm thick targets refluxing has little effect on the FWHM derived using the imager. This relatively low fast electron temperature will reduce the effect of refluxing. Within the experimental error bounds the divergence angle measured using this technique is the same as that previously measured using 1ω laser light on the same facility[29].

The measured bremsstrahlung emission over the 45° angle was highly uniform. This was found to be due to the relatively low fast electron temperature meaning

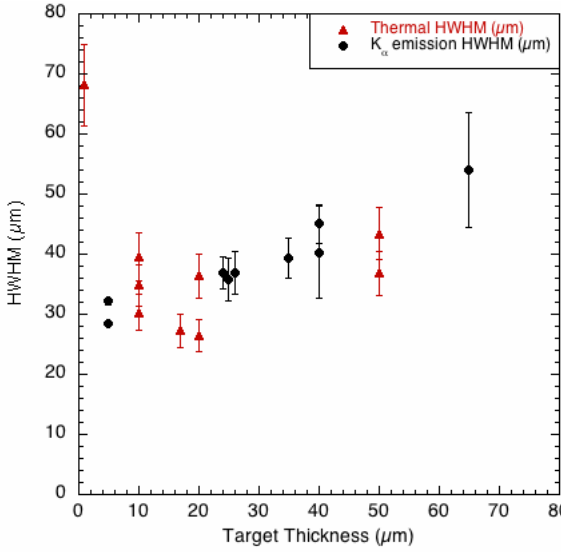

Figure 10. HWHM of thermal and Cu K_α emission as a function of target thickness or Cu layer depth respectively.

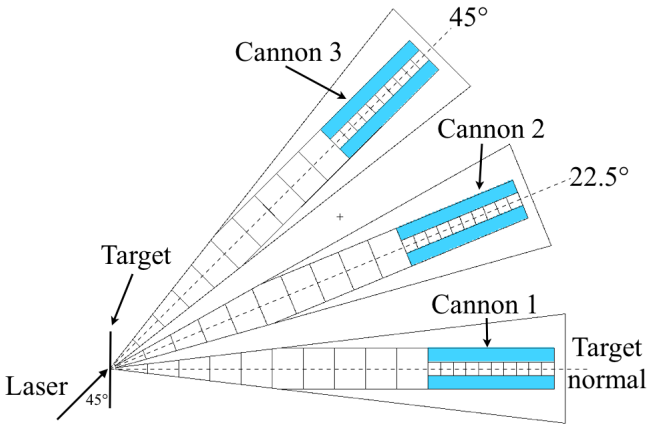

(a)

Figure 11. The 3D MCNPX model with 3 detectors positioned exactly as per the experiment.

the emitted bremsstrahlung is not measurably beamed, and is explained as follows: the mean energy of a non-relativistic Maxwellian is $3/2T$ while that of an ultra relativistic Maxwellian is $3T$, where T is the relativistic Maxwellian temperature. It was found numerically that the mean energy of a 100 keV relativistic Maxwellian is 22 keV, corresponding to $\gamma = 1.4$. The bremsstrahlung cone half-angle corresponding to this mean energy is 20°, hence over the 45° angle covered by the detectors, it is unsurprising the distribution is approximately uniform; the electron temperature is insufficient for beaming of the bremsstrahlung to occur over the measurement angle (the average Lorentz factor is too low), meaning no information about the source angular distribution can be inferred from these experimental measurements. This was confirmed by modelling the target and all three detectors in MCNPX using the fast electron temperature derived from the experiment. The MCNPX model geometry is shown in figure 11, while figure 12 shows the calculated bremsstralung emission over the forward hemisphere, which is essentially uniform. This modelling was performed with a *collimated* electron beam entering the target with temperature 125 keV confirming that the fast electron temperature is insufficient for the emitted bremsstrahlung to be measurably beamed in the direction of the propagating electrons.

The fast electron beam divergence is often measured experimentally using Cu K_α imaging. By comparing the spatial distribution of the modelled Cu K_α radiation with the experimental Cu K_α data the Monte Carlo modelling can be further constrained. This technique provides a better measure of the divergence angle of the experimental fast electrons, as the role of scattering of the fast electrons is accounted for and any blooming of the fast electron beam can be subtracted from the total measured divergence, yielding the true divergence of the injected electrons. It has been shown that when modelling the energy deposition of two temperature fast electron distributions non-unique solutions may be arrived upon[?] . Here this is avoided by fitting the Monte Carlo modelling to the spatial distribution of the experimental data. The issue of non-unique solutions is avoided as the high temperature component of a two temperature distribution will be more beamed and hence should be visible in the spatial distribution of the bremsstrahlung radiation (assuming the high temperature component has a sufficiently high mean Lorentz factor).

4. Laser Energy Absorbed into Fast Electrons

Based on the absolute calibration, and best fitting relativistic Maxwellian temperature of 125 ± 25 keV, the fraction of the laser energy absorbed into fast electrons was found to be 13 ± 4 %. The principal sources of error were due to the uncertainty in the relativistic Maxwellian temperature (and the associated mean electron energy) and the image plate calibration, the variance of the MCNPX modelling was < 0.7 %.

When using this technique it is crucial that the modelled response of all the detectors matches that of the experimental data as otherwise this technique would give anomalous results. In this case the bremsstrahlung emission was found to be relatively isotropic over the forward hemisphere, meaning the modelling could be fitted to the experimental data with relatively few iterations. The near isotropic emission gives added confidence that any important spatially varying features of the experimental data have been captured despite the limited solid angle covered by the detectors, and hence that the in-

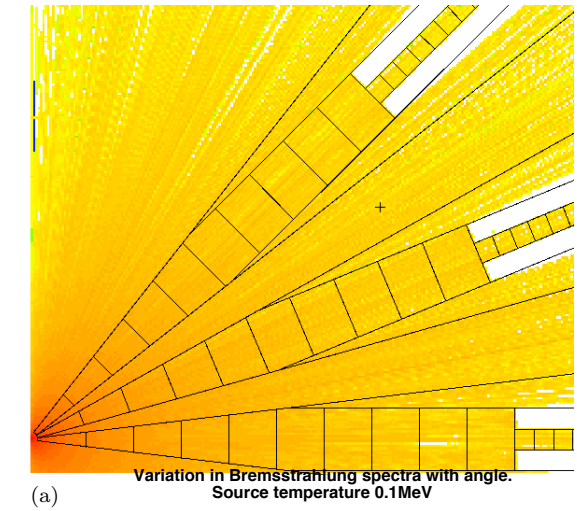

(a)

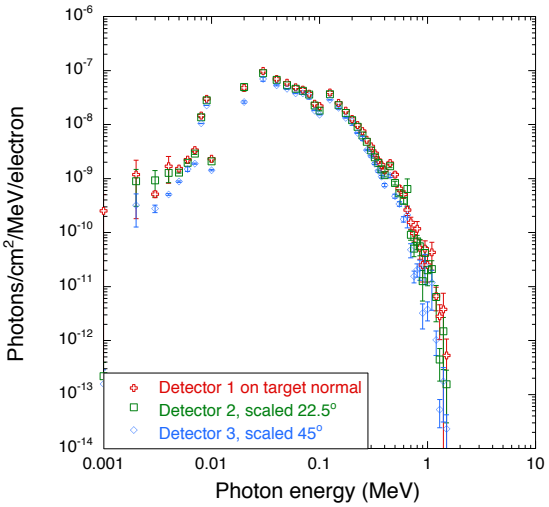

(b)

Figure 12. (a) The modelled spatial distribution of bremsstrahlung flux of all energies. The target is at the bottom left of the image, while the lead shielding of the three detectors is visible as the white regions (low photon flux)towards the top and right. (b) The modelled flux spectra measured at the entrance to the three bremsstrahlung detectors (scaled to account for the differences in the detector distances from the target) shows very little spectral variation with angle.

ferred absorption fraction should be accurate. The laser energy absorption fraction was calculated separately for each detector and found to be consistent within ±1%, indicating the modelled bremsstrahlung emission accurately matches that of the experiment.

C. Discussion

The bremsstrahlung fast electron temperature analysis yielded a best fit with a relativistic Maxwellian temperature of 125 ± 25 keV. This value is low in comparison to current scaling laws. Based on an analysis of the focal spot[32] the temporally and spatially averaged mean laser intensity within the FWHM was found to be $5 \pm 3 \times 10^{18}$ W/cm^2. Based on Beg's[23], Sherlock's[2] and Wilks'[33] scaling laws the fast electron temperatures are found to be 240 ± 30 keV, 144 ± 20 keV and 242 ± 35 keV respectively. Only Sherlock's seems to be close to the experimental value, Sherlock's scaling is the same as that of Wilks but multiplied by 0.6. This experimental measurement is in a lower intensity regime than that necessary for fast ignition, however assuming this result scales to higher intensities, it is promising as it suggests that the ignition laser intensity can be higher than that predicted by Wilks' scaling before the electrons will become too energetic to stop in the compressed DT fuel

Based on bremsstrahlung measurements, the measured laser energy absorption fraction into fast electrons was found to be $13 \pm 3\%$. This is lower than recent measurements by Ping *et al*[34] which measured the total laser light absorbed rather than the energy in the fast electron distribution. This disparity will partly be caused by energy being transferred away from the electrons via processes the Monte Carlo modelling cannot model (e.g. ion acceleration, collective field generation). Furthermore the pulse length in Ping *et al's* experiment was considerably shorter - such a short pulse may be completely absorbed by any pre-plasma. Although the measured $13 \pm 3\%$ is lower than that desirable for fast ignition purposes, based on the absorption-intensity curves of Ping *et al*, the absorption fraction may be as high as 4× this value at fast ignition relevant intensities. The measured value shows very good agreement with the lower intensity measurements of Yasuike *et al*[35] which rises from 12% at 2×10^{18} W/cm^2, to 18% at 10^{19} W/cm^2, reaching 50% at 10^{20} W/cm^2.

In summary, we have designed a novel bremsstrahlung photon detector which overcomes many of the shortcomings of previous designs, having 25 spectral resolution 'bins' over the region of interest in a configuration which easily allows multiple detectors to be fielded experimentally. The detectors were successfully fielded on an experiment using frequency doubled laser light. Analysis of the experimental data was performed with the 3D Monte Carlo code MCNPX. The data was best fit with a relativistic Maxwellian of temperature 125 ± 25 keV, and is closest to Sherlock's scaling law. The measured laser to fast electron conversion efficiency was $13 \pm 3\%$ - consistent with others' work showing a conversion efficiency of 50-60% at ignition relevant intensities.

REFERENCES

[1] S. C. Wilks *et al.*, Phys. Rev. Lett. **69**, 1383 (1992), copyright (C) 2008 The American Physical Society Please report any problems to prola@aps.org PRL.
[2] M. Sherlock, Phys. Plamas **16**, 103101 (2009).
[3] M. G. Haines *et al.*, Phys. Rev. Lett. **102**, 045008 (2009).

[4]M. H. Key *et al.*, Hot electron production and heating by hot electrons in fast ignitor research (1998).
[5]M. Key *et al.*, Journal de Physique IV (Proceedings) **133**, 371 (2006).
[6]E. L. Clark *et al.*, Phys. Rev. Lett. **84**, 670 (2000).
[7]R. A. Snavely *et al.*, Phys. Rev. Lett. **85**, 2945 (2000).
[8]A. Maksimchuk *et al.*, Phys. Rev. Lett. **84**, 4108 (2000).
[9]D. Hoarty *et al.*, High Energy Density Phys. **3**, 115 (2007).
[10]P. K. Patel *et al.*, Phys. Rev. Lett. **91**, 125004 (2003).
[11]F. Perez *et al.*, Phys. Rev. Lett. **104**, 085001 (2010).
[12]H. Nishimura *et al.*, Physics of Plasmas **18**, 022702 (2011).
[13]A. Saemann *et al.*, Phys. Rev. Lett. **82**, 4843 (1999).
[14]M. Tabak *et al.*, Phys. Plamas **1**, 1626 (1994), part 2.
[15]R. Kodama *et al.*, Nature **412**, 798 (2001).
[16]J. J. Honrubia and I. Meyer-Ter-Vehn, Nuclear Fusion **46**, L25 (2006), three-dimensional fast electron transport for ignition-scale inertial fusion capsules 10.1088/0029-5515/46/11/l02.
[17]S. Atzeni, A. Schiavi, and J. R. Davies, Plasma Phys. & Controlled Fusion **51**, 015016 (14pp) (2009).
[18]R. G. Evans, Plasma Phys. & Controlled Fusion **49**, B87 (2007), modelling electron transport for fast ignition 10.1088/0741-3335/49/12b/s07.
[19]C. Deutsch *et al.*, Phys. Rev. Lett. **77**, 2483 (1996).
[20]S. C. Wilks *et al.*, Phys. Plamas **8**, 542 (2001).
[21]M. A. Stoyer *et al.*, Nuclear diagnostics for petawatt experiments (invited) (2001).
[22]S. P. Hatchett *et al.*, Physics of Plasmas **7**, 2076 (2000).
[23]F. N. Beg *et al.*, Phys. Plamas **4**, 447 (1997).
[24]C. D. Chen *et al.*, A bremsstrahlung spectrometer using k-edge and differential filters with image plate dosimeters (2008).
[25]C. Courtois *et al.*, Phys. Plamas **16**, 013105 (2009).
[26]C. Chen, Private discussion.
[27]D. Pelowitz, Mcnpx user's manual version 2.6.0.
[28]R. Kodama, K. Okada, and Y. Kato, Review of Scientific Instruments **70**, 625 (1999).
[29]R. H. H. Scott *et al.*, Physics of Plasmas **19**, 053104 (2012).
[30]H.-K. Chung *et al.*, High Energy Density Physics **1**, 3 (2005), ISSN 1574-1818.
[31]M. I. K. Santala *et al.*, Phys. Rev. Lett. **84**, 1459 (2000), copyright (C) 2008 The American Physical Society Please report any problems to prola@aps.org PRL.
[32]H. P. Schlenvoigt, Private correspondance (2009).
[33]S. C. Wilks and W. L. Kruer, IEEE J. Quantum Electronics **33**, 1954 (1997).
[34]Y. Ping *et al.*, Phys. Rev. Lett. **100**, 085004 (2008).
[35]K. Yasuike *et al.*, Hot electron diagnostic in a solid laser target by k-shell lines measurement from ultraintense laser–plasma interactions (3 x 10[sup 20] w/cm[sup 2],¡= 400 j) (2001).

Developing an integrated approach to modelling short pulse laser-solid interaction.

Contact *Nathan.Sircombe@awe.co.uk*

N J Sircombe

AWE plc. Aldermaston, Reading, Berkshire, RG7 4PR, UK

Centre for Fusion, Space and Astrophysics, Department of Physics, University of Warwick, Coventry CV4 7AL, UK

Central Laser Facility, Science and Technology Facilities Council, Rutherford Appleton Laboratory, Chilton, Didcot, Oxfordshire, OX11 0QX, UK

S J Hughes

AWE plc. Aldermaston, Reading, Berkshire, RG7 4PR, UK

Centre for Inertial Fusion Studies, Imperial College London, South Kensington, London, SW7 2AZ

Introduction

Modern Particle in Cell (PIC) codes, VFP models and radiation hydrodynamic codes together constitute the tools required to model key aspects of short pulse laser-plasma interaction. However a complete description of the problem requires a daunting breadth of physics, which cannot reasonably be included in a single code. Our approach is to develop an integrated modelling capability in which detailed models for different aspects of the problem are linked together.

This note briefly outlines our methodology and demonstrates the approach taken to link PIC models of LPI into hybrid models of electron transport.

Background

A full description of short-pulse laser-solid interaction would require, at a minimum: accurate treatment of Maxwell's equations and kinetic effects where the laser is absorbed; collisional effects for the onward transport of fast particles ('hot electrons'); return current effects; and hydrodynamic response in the dense target, including ionisation and EOS.

However, the standard approaches to modelling in each of these areas are not compatible. Modelling laser-plasma interaction (LPI) necessitates a mesh which can capture the dispersion of electromagnetic waves, typically tens of cells per micron. The plasma in the interaction region must be treated with a kinetic model, to resolve the absorption physics which, at high intensities, generates fine scale structure in the distribution function and leads to distinctly non-thermal electron, and ion, populations. The problem of modelling laser plasma interaction boils down to the explicit solution of the Vlasov-Maxwell system of equations, typically through a macro-particle (i.e. Particle In Cell, PIC[1]) or continuum (i.e. direct Vlasov[2]) approach. In tackling this problem, the PIC code EPOCH[3] has proven to be an effective and flexible tool, offering a reasonable balance of fidelity and speed.

In the dense material of the bulk target, away from the LPI region, collisional physics dominates. The transport of hot particles generated by the action of the laser is dependent on their slowing and stopping in the dense material and their need to draw a return current to counterbalance the current they themselves carry into the target[4]. These effects will heat the target, which in turn influences transport. On longer timescales, the hydrodynamic response of the target will begin to play a role as the pressure generated from isochoric heating begins to take effect. Resolving such densities using an explicit kinetic code would make such an approach prohibitively expensive in terms of compute. Here, where comparatively large systems are needed, with material properties and bulk hydrodynamic motion, a more practical approach is to add additional physics to an existing radiation hydrodynamic model, treating the energetic hot populations separately to the colder bulk material.

The transport code THOR2 seeks to achieve this by adopting the approach of Davies et al.[5] - applying a Monte-Carlo approach to the solution of the Vlasov-Fokker-Planck equation for the energetic particles, against a background of cold, dense material which provides the return current. This 'hybrid' model can then be coupled back into an existing hydro code which provides material properties and hydrodynamic response.

These tools do not collectively make for a single, self-consistent, model of the laser-target interaction problem. The effects of hydrodynamic motion due to the laser pre-pulse should be included in the PIC code's initial conditions, for example, and the transport model needs to know what the energetic particle spectra emitted from the absorbtion region should be.

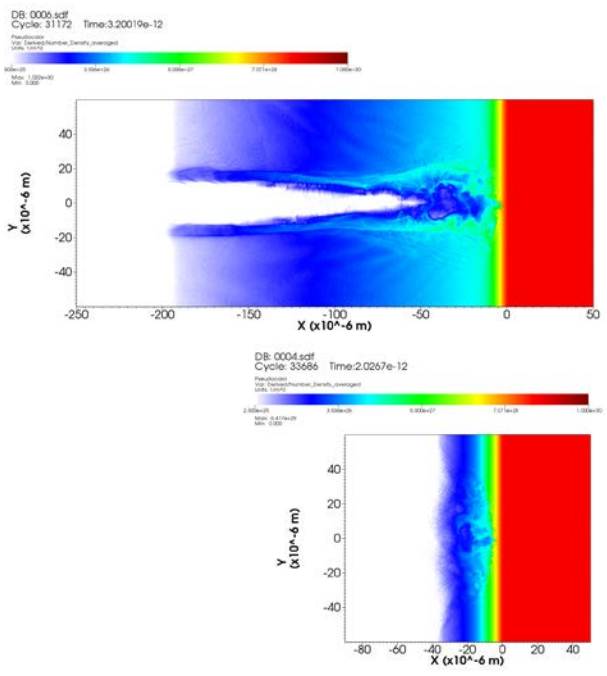

Figure 1: Electron density profiles from EPOCH for 50µm (top) and 10µm (bottom) scale-length pre-plasmas. In the long scale length plasma, a stable channel is formed. In both cases, filamentation as the beam approaches critical densities generates an unstable hot electron source which changes direction as the plasma evolves.

To address these issues, we plan to link our kinetic, transport and hydrocodes together to provide an integrated modelling capability, while at the same time augmenting and refining the physics available in the codes. There are three links which are

required: the ability to initialize EPOCH from hydrocode outputs (the link code FENRIS[6] was developed for this purpose); the integration of THOR2 into CORVUS (work on this link is currently ongoing); and a link from EPOCH to THOR2.

Here we focus on the link between EPOCH and THOR2, which allows the hot electron distributions used in THOR2 to be derived directly from the particle distributions generated by EPOCH, and present results for a number of pre-plasma and bulk target conditions.

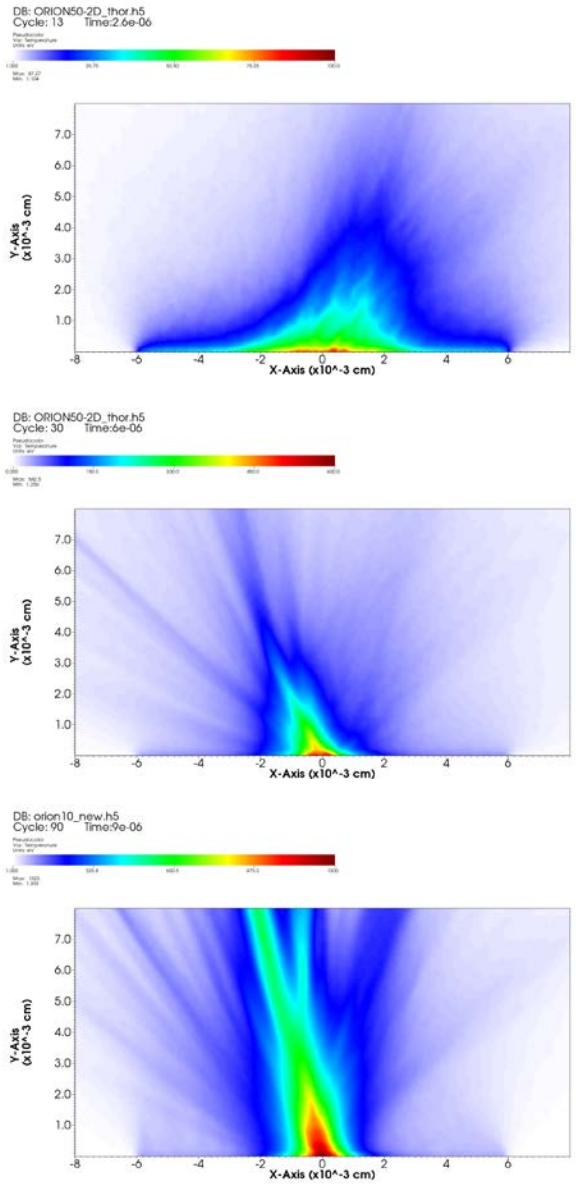

Figure 2: Temperature profile from THOR2 using a hot electron source generated form EPOCH simulations via the link code LOKI. The 'hosing' of the particle beam can be seen in the heating profile. For example, in the long scale length case, at early time (top) the electrons are directed to the right, generating a corresponding asymmetry in the heating profile. Whereas at later time (middle) the direction has shifted to the left. The lower average energy in the short scale length case (bottom) results in higher material temperatures. Here the shifts in direction have generated several distinct filaments in the heating profile.

LOKI: linking EPOCH and THOR2

LOKI generates a source term for the transport code THOR2 from the data generated by EPOCH's particle probes – a diagnostic which saves all the particle data for each particle that crosses a pre-defined plane in the simulation. This creates a distribution function in space, energy, angle and time which is saved into a relatively small (compared with the total PIC code output), portable HDF5 file.

THOR 2 is an explicit, hybrid electron transport code, with a Monte-Carlo VFP solver for the hot electron population. THOR2 generates particles from a LOKI source using a similar method to that used for analytic distribution functions. A point in 3D3P phase space is generated using a Sobol quasi-random number sequence[7], appropriate limits on the space are set by querying the LOKI dataset in order that the sampling is efficient. An initial weight is set by querying the appropriate phase space bin in the LOKI data, if the weight is very low the particle is ignored. When a new set of particles has been chosen the new distribution is normalised so that the weights correspond to a number of electrons that guarantee energy conservation.

Integrated modelling of the effect of pre-plasma scale length on target heating.

We use EPOCH to model a solid density target with two different pre-plasma conditions: a 50µm scale length pre-plasma extending from critical density out to 200µm in front of the target; a 10µm scale length pre-plasma extending from critical density to 40µm in front of the target. In both cases the density profile rises from critical to solid density with a scale length of 2µm.

A laser enters from the left-hand edge of the system. The characteristics of the beam are chosen to be equivalent to one of the PW arms of the Orion laser at AWE: wavelength = 1.053 µm; intensity = 1e20 W/cm^2; energy = 500J; pulse length = 2ps (Gaussian profile); spot radius = 6.7µm (Gaussian profile).

In the long scale length plasma, a stable channel is formed. In both cases, filamentation as the beam approaches critical density generates an unstable hot electron source which changes direction as the plasma evolves, see Figs. 1 & 2.

We use a particle migration algorithm to move electrons from the background into a 'hot' species once their energy exceeds a fixed multiple of the background. This allows us to differentiate between the energetic electrons important for target heating and the slow-moving 'background' population. A particle probe plane located just inside the target records 'hot' particles as they pass through. This data is then passed to LOKI to generate a source distribution for THOR2.

In the long scale length case, the distribution produced has a high energy tail – many of these energetic electrons leave the system. The 'colder' distribution generated in the short scale length case results in considerably stronger target heating.

The 'hosing' of the hot electrons, due to the evolution of filaments near critical density, and later between critical and solid density, is clear in both cases and has a lasting impact on the target heating profile (see Fig. 2).

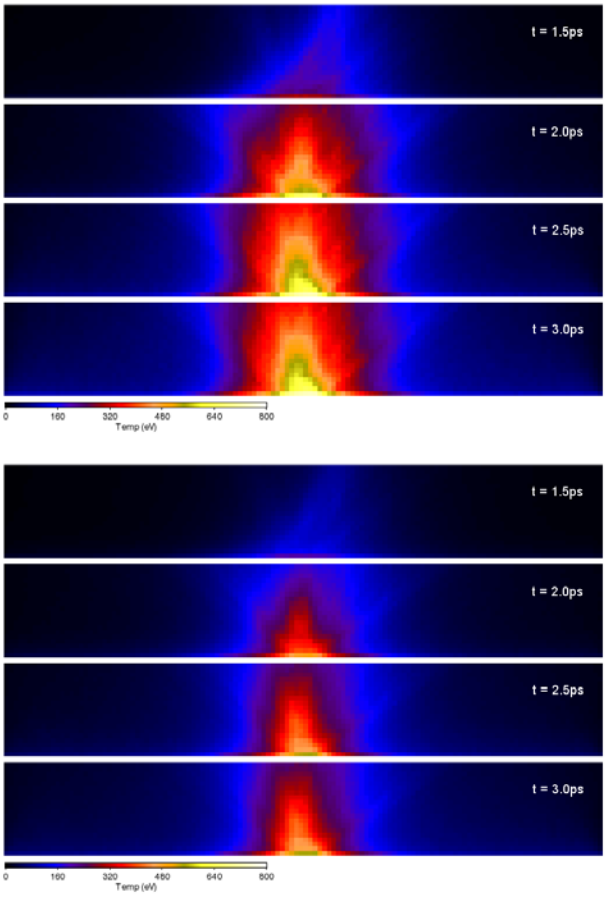

Figure 3: THOR2 modelling of target heating in plastic (top) and diamond (bottom) using an EPOCH hot electron source. The system is 160µm wide and 40µm deep. The same LOKI file is used as a source in both cases. The heating profile is largely unaffected but, due to its higher density, the diamond target reaches a lower temperature than the plastic target.

Modelling target heating in plastic and diamond targets with an EPOCH derived hot electron source.

In this example a hot electron source generated by an EPOCH simulation of a first harmonic 125J, 0.5ps pulse with a peak intensity of 5e19Wcm^{-2} interacting with a pre-formed plasma with a scale-length of 3µm. This same source is used for two separate THOR2 simulations: one of solid plastic, at 1g/cc; and one of diamond, at 3.5g/cc. Sesame EOS and Spitzer resistivity are used in THOR2 in each case.

Figure 3 indicates that the change in material leaves the heating profile largely unaffected. However, due to its higher density, the diamond target reaches a lower temperature than the plastic target. In this instance, the different material properties of the diamond target may, in actuality, lead to a different pre-plasma environment in response to the same laser pre-pulse. A shorter pre-plasma could be expected to produce a colder energy distribution and stronger return current heating, compensating for the apparent reduction in temperature relative to the plastic target. It is important to note that with an analytic source, using scaling based on empirical relations between hot electron 'temperature' and laser intensity, it would not be possible to make this assessment, but with an integrated modelling capability we can study the interplay of changes to the laser and target parameters in a more self-consistent manner.

Conclusions

We have outlined the motivation for linking LPI, transport and hydro models together and demonstrated some of the work carried out to date on linking PIC models of LPI into hybrid models for electron transport. This integrated modelling capability, as it matures, will provide a flexible, capable and extensible tool to support the design and analysis of experiments on laser systems such as Vulcan and Orion.

In short pulse laser-solid interaction, the extent of the pre-plasma in front of the target, at the time the main pulse arrives, has a significant impact on the heating of the bulk target. Longer scale-lengths tend to give higher absorption, but this does not necessarily couple to the hot electrons – and the hot electrons generated tend to have higher particle energies which may not be suitable for bulk heating of the target.

The 'hosing' of the electron source, as a result of the evolution of the laser path through the pre-plasma also impacts the heating of the target. Significant changes in direction over the laser pulse may help to heat the bulk target, and can even seed large filamentary structures. This is an effect which is often omitted from target heating models which assume some form of analytic source. It is a clear demonstration of the potential benefits of linking transport models to large-scale PIC simulations of LPI.

The use of LOKI to link EPOCH to THOR2 provides an element of flexibility; LOKI distributions, once generated, can provide a source for a multiple THOR2 simulations, to model how changes to conditions in THOR2 affect the evolution of the system. Conversely a number of LOKI distributions could be tried with the same THOR configuration to see how differing assumptions about the pre-plasma might affect the target. In either case, there is no necessity to re-run the computationally expensive PIC simulation for every change to the target parameters. It is possible to use LOKI files generated previously to perform quick parameter-scans over differing bulk target or pre-plasma conditions, repeating and refining the supporting EPOCH simulations only when absolutely necessary.

References

1. C.K. Birdsall, A.B. Langdon, "Plasma physics via computer simulation", IoP (1991).
2. N. J. Sircombe and T. D. Arber. "VALIS: A split conservative scheme for the relativisitic 2D Vlasov-Maxwell system." *J. Comp. Phys.*, **228**, 4773(2009).
3. www.ccpp.ac.uk
4. A. R. Bell, J. R. Davies, S. Guerin, and H. Ruhl. "Fast electron transport in high-intensity short-pulse laser-solid experiment." *Plasma Phys. Control. Fusion*, **39**, 653 (1999).
5. J. R. Davies, A. R. Bell and M. Haines. "Short-pulse high-intensity laser-generated fast electron transport into thick solid targets", *Phys. Rev. E*, **56**, 7193, (1997).
6. M. G. Ramsay, PPD Annual Report 2010, www.awe.co.uk
7. W. H. Press, B. P. Flannery, S. A. Teukolsky, and W. T. Vetterling. "Numerical Recipes in Fortran", Cambridge, (1986).

Wave breaking and saturation of resonantly driven waves in warm plasma

R.M.G.M. Trines[1, *]

[1] *Central Laser Facility, STFC Rutherford Appleton Laboratory, Didcot, United Kingdom*

A unified theory for the growth and breaking or saturation of driven waves in a warm, inhomogeneous plasma is presented. This theory incorporates both secular growth and convective saturation of the waves, and incorporates earlier results for growing waves in cold plasma [Koch and Albritton, Phys. Rev. Lett. **32**, 1420 (1974)] and saturated waves in warm plasma [V.L. Ginzburg (Gordon and Breach, New York, 1961)]. It also discusses previous attempts to reconcile these two limiting cases.

Wave breaking of plasma waves has been studied intensively for homogeneous plasma [1–3] as well as for undriven waves in inhomogeneous plasma [4, 5]. However, wave breaking of plasma waves driven by resonant absorption of a long, low-intensity laser beam is important for e.g. fuel assembly in laser-driven nuclear fusion. The driven wave can either break [6] or dissipate its energy because of its finite group velocity [7]. In the first case, laser energy is converted into electron kinetic energy via collisionless heating. In the second case, the driven wave may carry energy away from the compressed fuel. Which case applies is determined by the balance between the energy supplied by the driving laser pulse and the energy carried away because of the (Bohm-Gross) group velocity of the plasma wave [8]. Thus, it is important to have a good description of the growth and evolution of a driven plasma wave, including the thermal effects that govern the group velocity.

We consider a warm electron plasma with density profile $n = n_{cr}(1 + x/L)$ and electron thermal speed $v_T^2 = k_B T_e/m_e$. An incident laser beam with frequency $\omega_0^2 = e^2 n_{cr}/(\varepsilon_0 m_e)$ and field amplitude $x_D = eE_D/(m_e\omega_0^2)$ drives a longitudinal plasma oscillation via resonant absorption. The cold-plasma case ($v_T = 0$) has been treated by Koch and Albritton [6]. They determined the wave breaking limit for their cold-plasma solution, using Dawson's definition $|\delta'| = 1$. They found a wave-breaking time of $\omega_0\tau_c = \sqrt{8L/x_D}$ and a wave-breaking amplitude of $\delta_c = \sqrt{2Lx_D}$. For warm plasma, where the energy supplied by the laser beam is completely balanced by the energy carried away by the plasma wave, a saturated solution with amplitude $\delta_G/x_D =\approx 1.2(\omega_0 L/v_T)^{2/3}$ was found by Ginzburg [7].

Several attempts have been made to reconcile these two limiting solutions. The simplest approach was employed by Estabrook, Valeo and Kruer [9], who compared δ_c and δ_G and assumed that the lowest of these two limits would determine the eventual behaviour. A more elaborate approach was employed by both Kruer [10] and Bezzerides and Gitomer [11], who inserted the cold-plasma solution (3) into a definition for warm-plasma wave breaking. Here, Kruer uses Coffey's definition $|\delta'| = 1-(3v_T^2/v_\varphi^2)^{1/4}$ [12] and Bezzerides and Gitomer use the ad-hoc definition $|\delta'| = 1 - 0.64(v_T^2/v_\varphi^2)^{2/7}(L/x_D)^{1/7}$. However, all the approaches [9–11] suffer from the following shortcoming. The expressions used for the phase velocity v_φ of the driven wave are derived from cold-plasma theory: $v_\varphi = \omega_0\delta_c^2/|\delta|$ [10] or $v_\varphi = \omega_0\delta_c/\sqrt{|\delta'|}$. This ignores a fundamental difference between a non-dissipative driven wave in cold plasma, for which both the amplitude δ and the wave number k are growing, and saturated waves in thermal plasma, where at most one of δ and k is growing. While $v_\varphi = \omega_0\delta_c^2/|\delta|$ in the first case, $v_\varphi = \omega_0\delta_c^2/(2|\delta|)$ in the second. As long as there is such ambiguity concerning the phase speed, wave breaking cannot be studied properly.

A different approach has been used by Bergmann and Mulser [13]. In their paper, they use the stationary solution for a cold plasma flowing at constant speed [14, 15] and determine the wave breaking limit for this case using the criterion $|\delta'| = 1$. Then they insert the group velocity at the end of the resonance zone $v_g = 3v_T^2 k_G/\omega_0$ in lieu of the flow speed to determine the wave breaking limit for a driven wave in a non-flowing warm plasma. However, this approach ignores the fact that the group speed associated with Ginzburg's stationary solution (4) is not constant, but depends on the local wave number $k(\bar{x})$, and that $k(\bar{x}) \propto \bar{x}$ outside the resonance zone for a plasma flowing at constant speed [14, 15], but $k(\bar{x}) \propto \bar{x}^{1/2}$ according to (4), as also explained in Refs. [5, 14]. This leads to strange discrepancies, such as $v_\varphi = 3v_T^2/v_g = \omega_0/k_G$, but also $v_\varphi = |\partial\delta/\partial\tau|/|\partial\delta/\partial\bar{x}| = 0.72\sqrt{\omega_0 L v_g} = 0.72\omega_0/k_G$. It also ignores the fact that the group speed of a driven wave is not constant as long as the wave has not yet saturated. Since the onset of wave breaking cannot be determined if the wave phase or group speed is not accurately known, this approach is not fully satisfactory either.

In this paper, the following approach will be followed. First, a global solution to Eqns. (1) and (2) below is derived that reconciles the two limiting cases (3) and (4). Second, a proper definition for the breaking of this wave is derived that includes thermal effects and the growth of both the amplitude and the wave number. Third, this definition will be used to determine wave breaking of a plasma driven by resonance absorption including thermal effects. Since this approach takes the dynamic evolution of both the wave amplitude δ and its spatial derivative

*Electronic address: raoul.trines@stfc.ac.uk

δ' (and thus of the wave number $k \equiv |\delta'|/|\delta|$, the phase speed $v_\varphi \equiv \omega/k$ and the group speed $v_g \equiv 3v_T^2 k/\omega$), this approach does not suffer from any of the issues mentioned above.

We consider a warm electron plasma with density profile $n = n_{cr}(1 + x/L)$ and electron thermal speed $v_T^2 = k_B T_e/m_e$. An incident laser beam with frequency $\omega_0^2 = e^2 n_{cr}/(\varepsilon_0 m_e)$ and field amplitude $x_D = eE_D/(m_e\omega_0^2)$ drives a longitudinal plasma oscillation via resonant absorption. We transform to Dawson's coordinates $(\bar{x}, \tau)$ [1], where $\bar{x}$ denotes the average position of an electron and τ the time. Writing $x(\bar{x}, \tau) = \bar{x} + \delta(\bar{x}, \tau)$, $t = \tau$, we find the following equations for the electron motion [11]:

$$\frac{\partial^2\delta}{\partial\tau^2} - 3v_T^2\frac{\partial^2\delta}{\partial\bar{x}^2} + \omega_0^2(1 + \bar{x}/L)\delta = -\omega_0^2 x_D \sin(\omega_0\tau), \quad (1)$$

$$\frac{\partial^2\delta'}{\partial\tau^2} - 3v_T^2\frac{\partial^2\delta'}{\partial\bar{x}^2} + \omega_0^2(1 + \bar{x}/L)\delta' = -\omega_0^2\delta/L, \quad (2)$$

where $\delta' = \partial\delta/\partial\bar{x}$. For a cold plasma, the following growing solution is found [6]:

$$\delta_K(\bar{x}, \tau) = \frac{x_D}{(2+\nu)(1+\nu)}\big[\sin(\omega_0\tau) - \sin(\nu\omega_0\tau/2)\cos(1+\nu/2)\omega_0\tau/(\nu/2)\big], \quad (3)$$

where $\nu = \omega_p/\omega_0 - 1 = \sqrt{1 + x/L} - 1$. In a warm plasma, for $\tau \to \infty$, when energy dissipation balances the energy input from the source term $\omega_0^2 x_D$, the following stationary solution is found [7]:

$$\delta_G(\bar{x}) = k_G L x_D \zeta^{1/2} \times \times \begin{cases} \left[J_{1/3}(2\zeta^{3/2}/3) + J_{-1/3}(\frac{2}{3}\zeta^{3/2})\right], & \zeta > 0, \\ \left[-I_{1/3}(2|\zeta|^{3/2}/3) + I_{-1/3}(\frac{2}{3}|\zeta|^{3/2})\right], & \zeta < 0, \end{cases} \quad (4)$$

where $\zeta = k_G\bar{x}$, $k_G^3 = \omega_0^2/(3v_T^2 L)$. It is our aim to find a general solution to (1)-(2) that connects these two limiting cases.

To start, a solution of the form $\delta(\bar{x}, \tau) = A(\bar{x}, \tau)\cos[\psi(\bar{x}, \tau)]$ is inserted into (1). Writing $k \equiv \partial\psi/\partial\bar{x}$ and $\omega \equiv -\partial\psi/\partial\tau$, this yields the following relations:

$$[\omega^2 - 3v_T^2 k^2 - \omega_0^2(1 + \bar{x}/L)]A = [2\omega A_\tau + \omega_\tau A + 3v_T^2(2kA_{\bar{x}} + k_{\bar{x}}A)](\psi + \omega_0\tau), \quad (5)$$

$$[2\omega A_\tau + \omega_\tau A + 3v_T^2(2kA_{\bar{x}} + k_{\bar{x}}A)]\sin\psi = -\omega_0^2 x_D \sin(\omega_0\tau) \quad (6)$$

The first of these relations is the Bohm-Gross dispersion relation [8], extended for a plasma wave on a density gradient [5]. The second relation governs the growth of the wave amplitude $A(\bar{x}, \tau)$. Since the wave frequency inside (outside) the resonance region is mostly determined by the source frequency ω_0 (plasma frequency $\omega_0\sqrt{1 + \bar{x}/L}$), the term $\omega_\tau A$ is neglected with respect to ωA_τ. Also, a long scale length L is assumed, so $kA_{\bar{x}}$ is a small perturbation with respect to $k_{\bar{x}}A$ and x_D. Then the following relation is found for the growth of the amplitude A inside the resonance region:

$$\frac{\partial A}{\partial\tau} + \frac{\omega_0}{2k_G^3 L}\left[\frac{\partial k}{\partial\bar{x}} + \frac{2k}{A}\frac{\partial A}{\partial\bar{x}}\right]A = \frac{\omega_0 x_D}{2(1 + \bar{x}/L)^{1/2}}. \quad (7)$$

Using the following initial and final conditions, derived from Eqns. (3) and (4),

$$\left.\frac{\partial A}{\partial\tau}\right|_{\tau=0} \approx \frac{\omega x_D}{2 + (3/2)\bar{x}/L}, \quad (8)$$

$$\lim_{\tau\to\infty} A(\bar{x}, \tau) \approx 3\pi^{-1/2}\, k_G L x_D (1 + k_G\bar{x})^{-1/4}, \quad (9)$$

we find the following solution for $A(\bar{x}, \tau)$:

$$A(\bar{x}, \tau) = C[1 - \exp(-\lambda\tau)], \quad (10)$$

$$C = 3\pi^{-1/2}\, k_G L x_D (1 + k_G\bar{x})^{-1/4}, \quad (11)$$

$$\lambda = \frac{\pi^{1/2}}{3}\frac{\omega_0}{k_G L}\frac{(1 + k_G\bar{x})^{1/4}}{2 + 3\bar{x}/(2L)}, \quad (12)$$

an equation governing the wave number k [5]:

$$\frac{\partial k}{\partial\tau} + \frac{\omega_0}{k_G^3 L}k\frac{\partial k}{\partial\bar{x}} = -\frac{\omega_0}{2L}, \quad (13)$$

and an equation governing the energy flux:

$$\frac{\partial kA^2}{\partial\bar{x}} = \frac{\pi^{1/2}}{3}k_G^4 L^2 x_D^2. \quad (14)$$

Similarly, inserting $\delta' = B(\bar{x}, \tau)\sin[\psi(\bar{x}, \tau)]$ into (2) yields:

$$\frac{\partial B}{\partial\tau} + \lambda B = \frac{\omega A}{2L}. \quad (15)$$

Applying the initial conditions $B(\bar{x}, 0) = B_\tau(\bar{x}, 0) = 0$, we find the following (WKB) solution:

$$B(\bar{x}, \tau) = \frac{\omega}{2\lambda}\frac{C}{L}[1 - \exp(-\lambda\tau) - \lambda\tau\exp(-\lambda\tau)], \quad (16)$$

with C and λ as above. For small $\lambda\tau$ (i.e. small τ, large L or small v_T), the cold-plasma solution by Koch and Albritton is recovered [6], while for large $\lambda\tau$ the above solutions tend to the asymptotic solution by Ginzburg [7].

In Ref. [5], the wave-breaking limit for undriven waves was given as $\omega A = v_\varphi[1 - (3v_T^2/v_\varphi^2)^{1/4}]$. For the current case, this translates into

$$|\delta'| = 1 - [(1/k_G^3 L)|\delta'|^2/|\delta|^2]^{1/4}. \quad (17)$$

This is essentially a third-degree equation that can be solved to give $\sqrt{|\delta'|}$ in terms of $\sqrt{|\delta|}$. Inserting the results of Eqns. (10)-(15) into (17) will lead to a transcendental equation for $\lambda\tau$. Solving this equation will

then yield both the wave breaking time and the wave amplitude at the instant of breaking. For $\omega C/(2\lambda L) < 1-[(1/k_G^3 L)(\omega/2\lambda L)^2]^{1/4}$, or $k_G^2 L x_D < 1$, this will never happen and the solution will tend to Ginzburg's solution (4). In that case the energy supplied by the driving pulse is balanced by the energy carried away by the driven plasma wave, and the growth of the plasma wave saturates before it can break.

In summary, we have presented a new approach to wave breaking of a laser-driven plasma wave in a warm plasma with a density gradient, as seen in e.g. fuel assembly scenarios in laser-driven nuclear fusion. This approach unifies the two limiting scenarios of Koch and Albritton [6] and Ginzburg [7] while avoiding common pitfalls concerning the proper phase and group velocities of the driven wave. Further extensions of this method could include the inclusion of ion motion, plasma flow or relativistic effects.

[1] J. M. Dawson, Phys. Rev. **113**, 383 (1959).
[2] T. Katsouleas and W. B. Mori, Phys. Rev. Lett. **61**, 90 (1988).
[3] R.M.G.M. Trines and P.A. Norreys, Phys. Plasmas **13**, 123102 (2006).
[4] S. Bulanov, N. Naumova, F. Pegoraro and J. Sakai, Phys. Rev. E **58**, R5257 (1998).
[5] R. M. G. M. Trines, Phys. Rev. E **79**, 056406 (2009).
[6] P. Koch and J. Albritton, Phys. Rev. Lett. **32**, 1420 (1974).
[7] V.L. Ginzburg, *Propagation of Electromagnetic waves in Plasma* (Gordon and Breach, New York, 1961)
[8] D. Bohm and E. P. Gross, Phys. Rev. **75**, 1851 (1949).
[9] K. G. Estabrook, E. J. Valeo and W. L. Kruer, Phys. Fluids **18**, 1151 (1975).
[10] W. L. Kruer, Phys. Fluids **22**, 1111 (1979).
[11] B. Bezzerides and S. J. Gitomer, Phys. Fluids **26**, 1359 (1983).
[12] T. P. Coffey, Phys. Fluids **14**, 1402 (1971).
[13] A. Bergmann and P. Mulser, Phys. Rev. E **47**, 3585 (1993).
[14] S. V. Bulanov, L. M. Kovrizhnykh and A. S. Sakharov, Zh. Eksp. Teor. Fiz. **72**, 1809 (1977) [Sov. Phys. JETP **45**, 949 (1977)].
[15] P. Mulser, H. Takabe and K. Mima, Z. Naturforsch. A **37**, 208 (1982).

Monte Carlo studies of ion-ion inverse Bremsstrahlung absorption

Contact *a.turrell09@imperial.ac.uk*

A. Turrell, M. Sherlock, S. Rose

Blackett Laboratory, Imperial College London
SW7 2AZ

Introduction

A 0D Monte Carlo (MC) code has been developed to study ion-ion inverse Bremsstrahlung absorption in the presence of a linearly polarised laser field in the relativistic to 'ultra-relativistic' regime in which the Lorentz factor of the electrons is much greater than 1. The mechanism is analogous to electron-ion inverse Bremsstrahlung absorption, and applies to two or more species of ion with non-identical charge-to-mass ratios. The effect is increased for increasing densities and increasing Z, or for larger differences in charge-to-mass ratio.

Lasers with intensities of the order of 10^{22} W/cm^2 [1] have been demonstrated and the next generation, including ELI and Vulcan 10PW, will provide intensities reaching 10^{23} W/cm^2, corresponding to the ultra-relativistic regime. New physics is important in this regime, including quantum corrections, pair-production and new absorption processes ([2, 3, 4]).

The interplay of QED-plasma processes in this regime means a full simulation is extremely complex. Rather than solving the full problem, the code models ion-ion inverse Bremsstrahlung absorption in isolation, using an 'effective' intensity, defined as the intensity felt by the ions once other absorption effects are taken into account. As electrons are strongly affected by QED processes in this regime, and are an order of magnitude less effective in the transfer of energy to ions than are other ions, they are ignored. For this reason, only time periods of the order of the ion-ion equilibration time are considered.

The Monte Carlo code

The code is based on Takizuka and Abe's scheme [5]. The distribution of scattering angles for collisions between charged particles *i* and *j* is assumed to satisfy $\Theta \sim \mathcal{N}\left(0, \langle\Theta^2\rangle\right)$ where the variance is

$$\langle\Theta^2\rangle = \left(\frac{e^2 Z_i Z_j}{4\pi\varepsilon_0}\right)^2 \frac{\pi n}{2 m_{ij}^2 v_{ij}^3} \Delta t \ln\Lambda_{ij}$$

with n the lower of the densities of *i* and *j*, and Δt the timestep. Angles for individual collisions are given by a Box-Muller transform [6],

$$\theta = \sqrt{-2\langle\Theta^2\rangle \ln U_1}\cos(2\pi U_2); \quad U_1, U_2 \in (0,1]$$

with U_1, U_2 randomly distributed. Energy and momentum are conserved in each collision, and macroscopic variables such as temperature and Coulomb logarithm are updated each timestep.

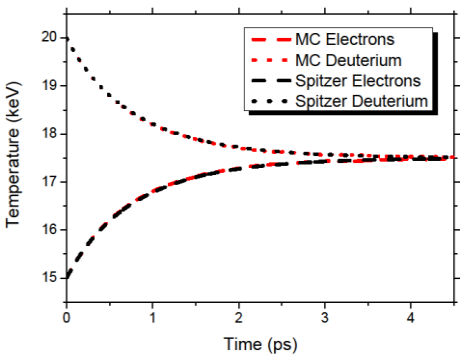

Fig. 1: Electron-ion equilibration for $n_e = n_i = 4 \cdot 10^{32}$ m^{-3}

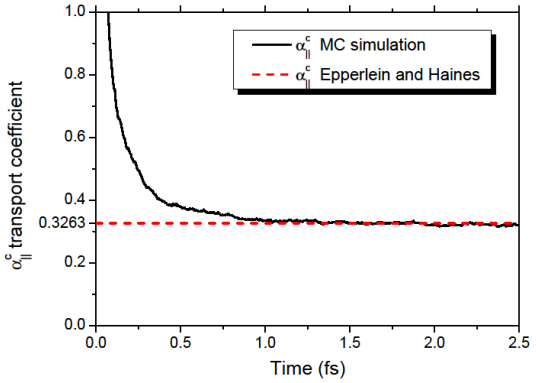

Fig. 2: Electrical resistivity transport coefficient for **B** = **0**, $E_x = 5 \cdot 10^9$ V/m, Z = 12

The code has been benchmarked against the Spitzer model of temperature equilibration as shown in Fig. 1 and it reproduces the electrical resistivity transport coefficient of Epperlein and Haines [6], Fig. 2.

The laser field

A laser field of period ω propagates in the z-direction, giving all charged particles a forced velocity. It is assumed that the reservoir of laser energy is infinite, and that all particles are fully ionised. The electric field acceleration induces a time-dependent relative velocity between species of different charge-to-mass ratios of

$$\boldsymbol{v} = \frac{e\boldsymbol{E}}{\omega}\cos(\omega t)\left(\frac{Z_i}{m_i} - \frac{Z_j}{m_j}\right)$$

The timestep must resolve ion-ion collisions but is also restricted by the uncertainty in the final momentum of the ions of $\approx Ze\langle\boldsymbol{E}\rangle\Delta t/\omega$. The laser pulse has a Gaussian growth and decay profile.

Ion-ion inverse Bremsstrahlung absorption

Under the guise of driven collisional ion heating, ion-ion inverse Bremsstrahlung absorption was first examined by Mjolsness and Ruppel [7]. Their ordinary differential equation method is restricted to two ion species and does not include temperature equilibration. The MC code includes temperature equilibration and can handle an arbitrary number of species.

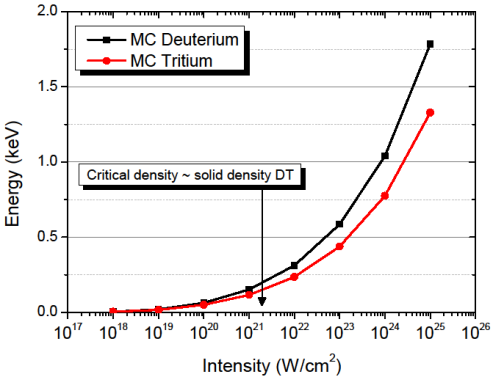

Fig. 3: DT, 500 fs pulse at critical density.

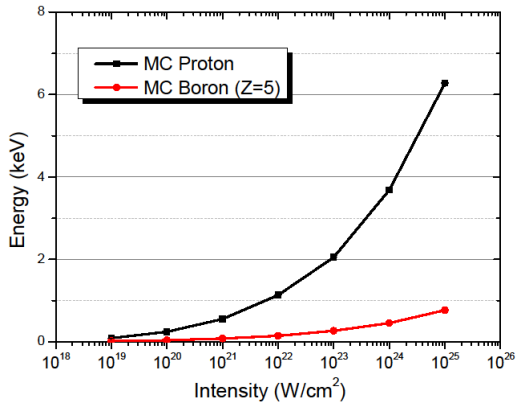

Fig. 4: pB, 300 fs pulse at critical density.

Fig. 3 shows the heating effect for two species of similar charge and mass. Using a high Z ion and a low Z ion pushes the low Z ion to much higher energies, as demonstrated in Fig. 4 with Boron. Fig. 5 also exhibits this effect, and shows how it applies to three ion species.

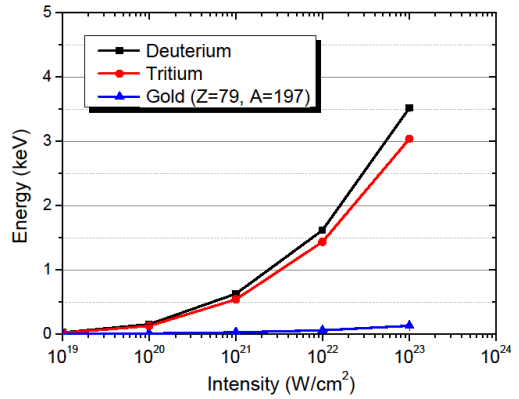

Fig. 5: AuDT, 30 fs pulse at critical density.

Conclusions

A full picture of the heating mechanism requires a model including the complex interplay of QED-plasma effects, but the MC simulations suggest that effective intensities of 10^{23} W/cm^2 applied for tens of fs can achieve energies in the keV via inverse Bremsstrahlung absorption with a suitable choice of ions. In future, more complex models and mathematical descriptions of ion-ion inverse Bremsstrahlung absorption will be sought, and a formal prescription for pulse shapes that maximise the heating rate provided.

References

1. S.-W. Bahk et al, *Optics Letters*, **29:24**, p. 2837, (2004)
2. C. P. Ridgers, C. S. Brady *et al.*, *Phys. Rev. Lett.*, **108**, 165006 (2012)
3. J. G. Kirk, A. R. Bell and I. Arka, *Plas. Phys. and Cont. Fus.*, **51**, 085008 (2009)
4. Y. Ping et al., *Phys. Rev. Lett.*, **100**, 085004 (2008)
5. T. Takizuka and H. Abe, *Journal of Comp. Phys.*, **25**, 205-219 (1977)
6. G. E. P. Box and M. E. Muller, *Annals of Math. Statistics*, **29:2**, 169-181 (1996)
7. E. M. Epperlein and M. G. Haines, *Phys. Fluids*, **29**(4), 1029 (1986)
8. R. C. Mjolsness and H. M. Ruppel, *Phys. Fluids*, **15**(9), 1620 (1972)